In situ field measurement of the Open Dipole magnet at the BGO-OD experiment

Torsten Frese

Diplomarbeit in Physik
angefertigt im Physikalischen Institut

vorgelegt der
Mathematisch-Naturwissenschaftlichen Fakultät
der
Rheinischen Friedrich-Wilhelms-Universität
Bonn

Dezember 2012

Ich versichere, dass ich diese Arbeit selbstständig verfasst und keine anderen als die angegebenen Quellen und Hilfsmittel benutzt sowie die Zitate kenntlich gemacht habe.

Referent:	Prof. Dr. Hartmut Schmieden
Koreferent:	PD Dr. Wolfgang Hillert

Contents

Chapter 1

Introduction

Ancient Greeks were already interested in the structure of matter. In the 5^{th} century BC, Leucippus the philosopher of nature and his pupil and successor Democritus developed the theory of atomism: the theory of matter composed entirely of various microscopic indivisible and immortal elements rapidly and randomly moving in a vacuum. They called the elements atoms (from the Greek *ἄτομος*: indivisible body). In the beginning of the 20^{th} century it was found out that the atom consists of electrons and one nucleus. In 1897, J.J Thomson discovered the electron, while he was studying cathode rays of different materials. In 1919, E. Rutherford observed the proton by irradiating nitrogen with α-particles. Two years later, he postulated the existence of another particle in the nucleus and called it the neutron. The neutron was observed eleven years later.

At the end of the 1960s, the deep inelastic scattering experiments at the Stanford Linear Accelerator Center (SLAC) revealed that protons and neutrons are not elementary particles. They consist of particles, called quarks. To date, six different types of quarks (up, down, charm, strange, top and bottom) and their corresponding antiparticles are known. Until today, quarks and antiquarks together with leptons and antileptons ($e^{\pm}$, $\mu^{\pm}$, $\tau^{\pm}$, $\nu_{e,\mu,\tau}$, $\overline{\nu}_{e,\mu,\tau}$) are known to be elementary particles. The electromagnetic, the weak and the strong interaction between these particles are mediated by the photon, the $W^{\pm}$, the Z^0 and the gluon.

Quarks can not be observed as free particles, but only in bound systems called hadrons, which are classified as mesons and baryons. Mesons carry an integer spin and consist of two quarks, while baryons have a half-integer spin and are composed of three quarks (like protons and neutrons). Since quarks can not be individually observed, O. W. Greenberg in 1964 postulated they have another intrinsic property which is not “visible“ in the hadrons. This property was called colour. Hadrons are thought as “white“ objects. As a consequence baryons are described as bound systems of three quarks, each with a different colour (red, blue and green); mesons as bound systems of colour-anticolour quark-antiquark couples.

The colour is interpreted as the charge of the strong interaction, which is the interaction responsible for keeping quarks in a bound state. The strength of the strong interaction is described by the corresponding coupling constant α_s. At high momentum transfer, α_s is small and perturbative methods can be used as an approximation in the QCD Lagrangian. Calculated results agree well with high energy particle physics experimental data.

At lower momenta transfer (less than $\approx 2\,\mathrm{GeV}$ and distances of $\approx 1\,\mathrm{fm}$) α_s is very large, preventing perturbative calculations to be used. This non-perturbative regime governs the physics of hadrons.

Hadrons are therefore often described by phenomenological models. There are various models which describe hadron properties, but there are still many open questions. For example: why does the experimentally observed proton excitation spectrum not agree with model prediction? Experiments with photons with high energy ($E_\gamma \sim 3\,\mathrm{GeV}$) which are used to excite nuclei are good for studying this. The excited resonances decay into mesons, which decay again into photons or lighter mesons. The analysis of the final decay states allows for the reconstruction of the excited resonances within a theoretical framework.

The BGO-OD experiment is a fixed target experiment for the systematic investigation of meson photoproduction processes off protons and neutrons. For fixed target photoproduction experiments where final state particles are Lorentz boosted at small angles in the laboratory system, it is important to have accurate particle momenta reconstruction in the forward direction.
To achieve this goal, the BGO-OD setup is equipped with a Forward Spectrometer, whose main component is an Open Dipole magnet.
Momenta of charged particles are determined by the curvature of their trajectory in the magnetic field, and a time of fight measurement enables particle identification (see Figure 1.1). An accurate measurement of charged particle momenta (with a resolution of 1.5% - 2%) requires a good knowledge of the magnetic field generated by the open dipole magnet as even a small anomaly of the magnetic field can change the track of the particles inside the magnet.

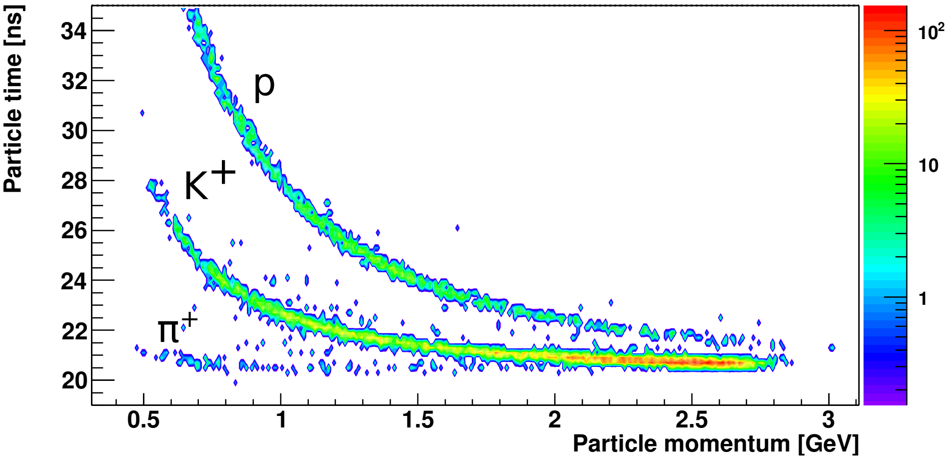

Figure 1.1: Particle momentum for simulated $\gamma p \rightarrow K^+\Lambda$, with a visible loci of protons, K^+ and π^+ (top, middle and bottom curves respectively)[Jud].

A first accurate measurement of the open dipole magnetic field was performed at the GSI in 2009. The aim of this thesis is to perform a new in situ measurement of some regions of the magnetic field. This is required to evaluate quantitatively the effects of distortions of the magnetic field due to the presence of shielding materials and metallic structures of the detectors close to the open dipole magnet. Even if distortions are small, a precise characterisation of the magnetic field will allow for high precision momenta reconstruction.
This work is organised as it follows. In the next chapter, the BGO-OD experiment is described. In chapter three the mapping of the magnetic field and the existing maps of the magnet are explained. The construction for the in situ measurement system is explained in detail in chapter four. Chapter five shows the results of the measurements from this work and compares them with older and simulated maps and an analysis of the momentum reconstruction using simulated data. The thesis ends with a summary.

Chapter 2

BGO-OD Experiment

The BGO-OD experiment is located at the Electron Stretcher Accelerator (ELSA) at the Physics Institute at the University of Bonn. In 1987, the ELSA stretcher ring was adept and can accelerate electrons up to 3.5 GeV. The smaller synchrotron exists since 1967 and is able to accelerate electrons up to 2.5 GeV [HS88]. When ELSA is working, the synchrotron is used as booster for the ELSA stretcher ring. Figure 2.1 shows an overview of ELSA. ELSA consists of three main parts. Two linear accelerators, LINAC1 and LINAC2 which respectively produce polarised and unpolarised electrons and accelerate them to about 20 MeV. The electrons are then injected into the booster synchrotron and accelerated to 1.6 GeV. Finally they are injected into the stretcher ring where they are accelerated to 3.5 GeV and then extracted alternatively into the experimental area of BGO-OD or CBELSA/TAPS (Crystal Barrel and the Two Arm Photon Spectrometer), the other main experiment at ELSA.

Figure 2.2 shows the setup of the BGO-OD experiment, with the electron beam entering from the left. In the following text it follows a short description of the BGO-OD setup, which will be described in terms of photon beam production and photon beam detectors (photon energy tagger, photon flux monitor and gamma intensity monitor), target system, detectors in the central region covering the polar angular range $25° \leq \Theta_{lab} \leq 155°$ in the laboratory frame (BGO, scintillator, barrel detector, MWPC) and the forward spectrometer covering the polar angular range $\Theta_{lab} \leq 12°$ in laboratory frame (MOMO, SciFi2, Open Dipole, Drift chambers and Time of Flight walls).
The name of the experiment refers to the main component of the central detector and of the forward spectrometer: the BGO-Ball and the Open Dipole magnet.

2.1 Photon beam

After the extraction of the electron beam into the BGO-OD area, the electron beam impinges on a thin (usually metal) radiator, which is placed inside the goniometer vacuum chamber. Bremstrahlung photons are produced by the deflection of the electrons in the electromagnetic field of the radiator atoms. The magnetic field of the tagging magnet is used to momentum analyse the scattered electrons. The photon energy is given by the energy difference of scattered and incoming electrons,

$$E_\gamma = E - E'$$

where E is the energy of incoming electrons and E' the energy of the scattered electrons.
At the end of the beamline, a gamma intensity monitor (GIM) is positioned behind the TOF (time of flight) walls. The GIM is a lead glass detector with 100% efficiency which absorbs and detects photons from the incident beam. The real photon flux of the experiment is measured by the GIM by counting the photons of the primary beam, that pass through the target. The calculation of the reaction cross section is based on the number of reactions and the photon flux [Pho].

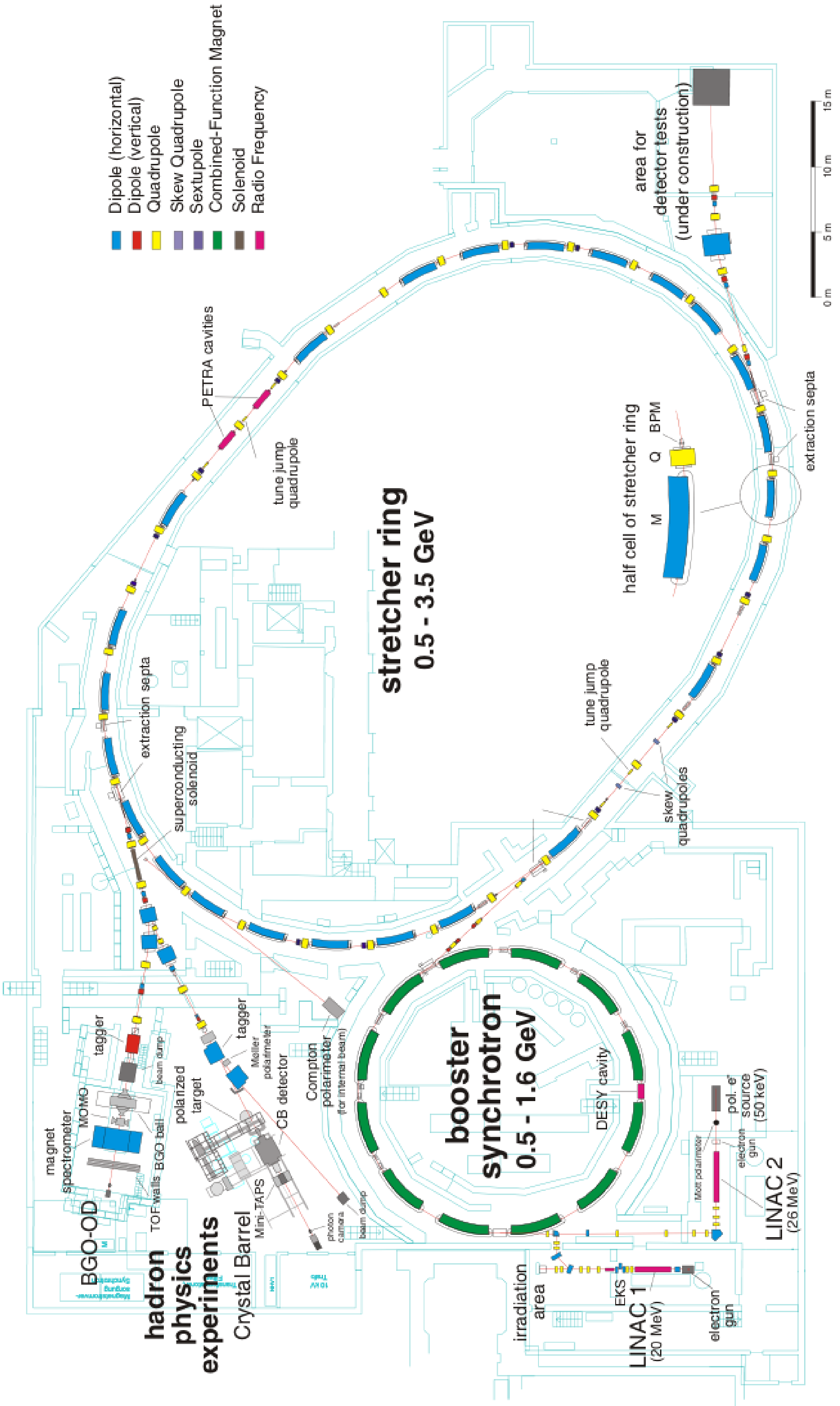

Figure 2.1: Electron Stretcher Accelerator (ELSA) [ELS09]

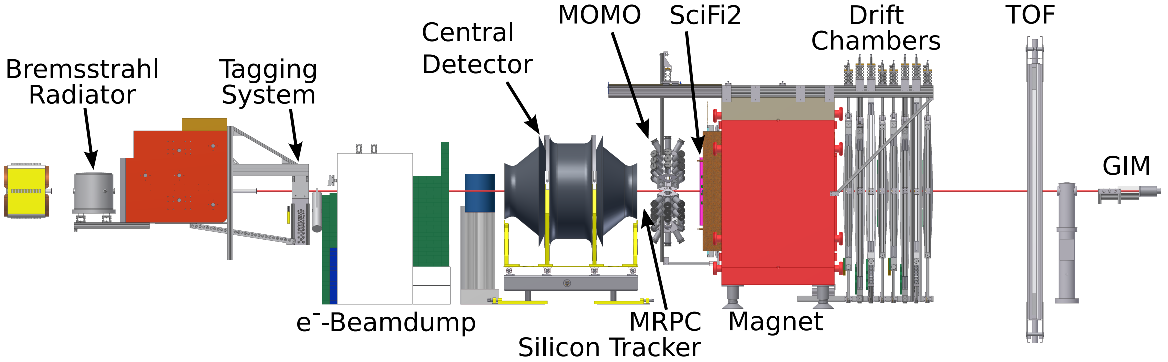

Figure 2.2: Overview of the BGO-OD experiment[Han]

2.2 Central detector

The central detector of the experiment consists of three parts: the MWPC, the scintillator barrel and the BGO-Ball. In the centre of the BGO-Ball there is a liquid deuterium or hydrogen target inside a cylindrical vacuum tube. The photons hit the target, causing photonuclear reactions. Mesons and baryons are produced, traversing the experimental setup and sometimes decaying to lighter particles on route. Figure 2.3 shows a picture of the BGO-Ball installed in the area with a liquid hydrogen target put inside from the left. Around the target two cylindric multiwire proportional chambers (MWPC) for inner tracking of charged particles are located. A scintillator barrel is located between the inner tracking detector (MWPC) and the crystals, to detect charged particles angle to measure their energy loss for unitary path ($\frac{dE}{dx}$). Together with the energy measured by the BGO colorimeter, the $\frac{dE}{dx}$ allows for charged particle identification. The barrel consists of 32 scintillators which have a length of ≈ 430 mm, a thickness of ≈ 5 mm, made of BC-448. They are coupled to Hamamatsu H3164-10 photomultiplier tubes.

The main detector of the central region is the BGO electromagnetic calorimeter. The BGO-Ball consists of 480 $Bi_4Ge_3O_{12}$ crystals with a length of 24 cm, which corresponds to approximately 21 radiation lengths. The crystals are arranged around the beam axis in 15 polar ($\vartheta = 25°$ to $155°$) and 32 azimuthal sectors ($\varphi = 0°$ to $360°$). The crystals readout is performed by photomultiplier tubes: 192 Hamamatsu R580 for the first and last three crowns and 288 Hamamatsu R-329-02 for the inner crowns. The BGO-Ball has around 90% acceptance of the 4π solid angle and is ideal for the detection of photons, charged particles the reconstruction of neutral mesons [O.B05][San96][Ghi98][Cas98].

2.3 Forward spectrometer

The forward spectrometer detects charged particles (usually $\pi^{\pm}$, $K^{\pm}$ and protons) and measures their momenta at forward angles ($\Theta \lesssim 12°$). The forward magnetic spectrometer consists of two tracking detectors (MOMO and SciFi2) in front of the magnet, an Open Dipole magnet, eight drift chambers for tracking behind the magnet and time of flight walls. Figure 2.4 shows a picture of the forward magnetic spectrometer in the area (beam travels from the bottom to the top of the photography). At the bottom of the photography, behind the end of the BGO-Ball, are the two tracking detectors MOMO and SciFi2. Behind them, in the middle of the photography the Open Dipole magnet is shown and behind the drift chambers. The time of flight walls are not visible on the photography. In the following this chapter

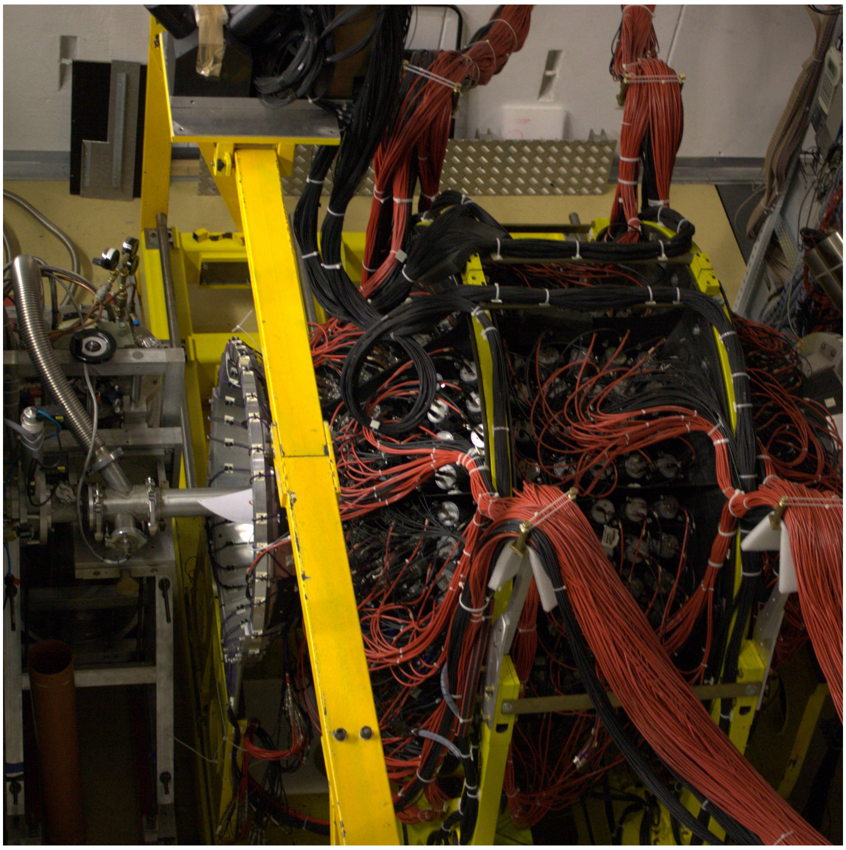

Figure 2.3: A picture the BGO ball. On the left side the cryogenic system for liquid H_2 or D_2 target is visible [Ham].

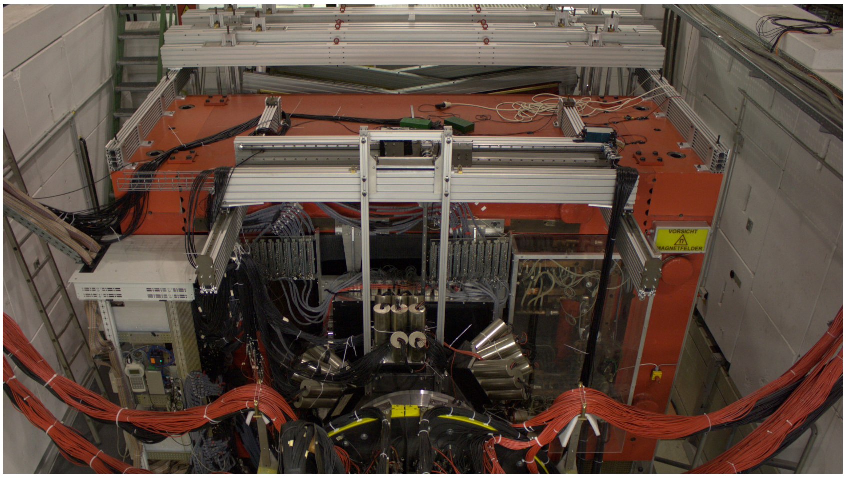

Figure 2.4: A photography of the forward magnetic spectrometer. The beam comes from the bottom of the photography [Ham].

describes the spectrometer components in more details.

Behind BGO is located the first tracking detector MOMO (Monitor of Mesonic Oberservables). This consists of six identical modules, with 672 scintillating fibres. The modules are arranged into three layers of 2.5 mm thick fibres, rotated by 60° with respect to each other. Figure 2.5 shows a schematic drawing of the detectors. The active area of the detector is circular with a diameter of 44 cm[MOM]. A 4.5 cm wide hole in the centre allows the primary photon beam to pass through. 16-channel Hamamatsu R4760 photomultipliers tubes read out the scintillating fibres. This detector was originally developed for the MOMO experiment at COSY and was used there for the detection of charged kaon and pion pairs. When charged particles or photons hit the sensitive region of MOMO they scintillate, giving the position of where they hit MOMO. This special arrangement of fibres allows to disentangle two particles which hit MOMO at the same time.
SciFi2 (scintillating fibre detector 2) works in the same way as MOMO, however it can not clearly distinguish between two particles which hit at the same time. SciFi2 gives a second reference point which allows for reconstruction of the track of charged particle which hit MOMO and SciFi2. SciFi2 consists of 288 vertical and 352 horizontal scintillating fibres with a diameter of 3 mm. The fibres are arranged in two horizontal and two vertical layers which overlap each other so that each incident particle hits at least one vertical and one horizontal fibre. The active area of SciFi2 has dimensions of 660 mm x 510 mm. A $4 \times 4\,\mathrm{cm}^2$ hole in the centre allows the beam to pass through. 16-channel Hamamatsu H6568 photomultiplier tubes are used for the read out of the scintillating fibres. A drawing of the arrangement of SciFi2 is shown in figure 2.6 [BÏ2].

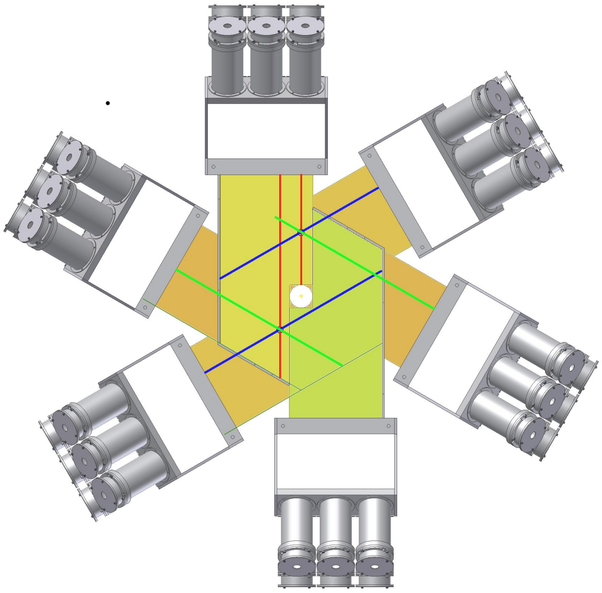

Figure 2.5: Drawing of the six MOMO detectors.

In the middle of the forward spectrometer is located the Open Dipole magnet with a dimension of $(2800 \times 3900 \times 1500)\,\mathrm{mm}^3$. Charged particles traversing the magnetic field are dispersed in the horizontal plane depending on their momentum. More information about the magnet is given in chapter 3.

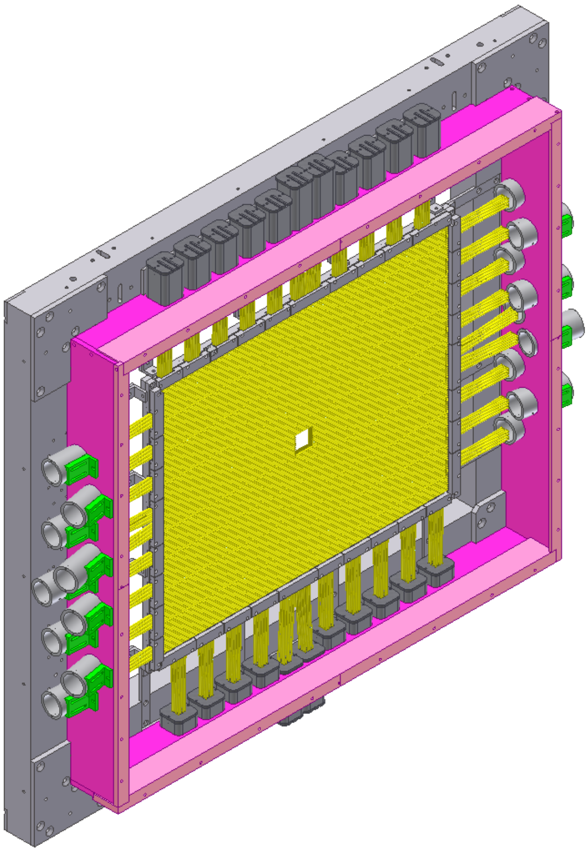

Figure 2.6: Drawing of SciFi2 [BÏ2].

Eight drift chambers are mounted behind the Open Dipole magnet, each contains a double layer of hexagonal drift cells. A particle should traverse two drift cells in each chamber it passes. The position of the cells which were hit by charged particles allows for reconstruction of the curvature of the deflection of the charged particle in the magnetic field. There are four different orientations with two chambers of each orientation: vertical wires to measure the x-coordinate, horizontal wires to measure the y-coordinate and wires tilted by ±9° to the vertical, to distinguish between true and false combinations of multiple hits in the x and y chambers [Dri].

At the end of the forward magnetic spectrometer behind the drift chambers, the time of flight (TOF) wall are mounted. The TOF wall consist of 14 vertically arranged scintillating bars. Each scintillating bar has an active area of $2.7 \times 0.2 \times 0.045\ \mathrm{m}^3$. A second wall with eight horizontally arranged scintillating bars with an active area of $3.4 \times 0.215 \times 0.06\ \mathrm{m}^3$ per bar will be mounted in the next future. The bars have photomultiplier tubes (PMTs) attached to both ends. The TOF walls are used to measure particle speeds by the time difference from target to TOF walls [Jah].

Chapter 3

Field mapping of the spectrometer magnet

Figure 3.1: The open dipole magnet [BGO]

The open dipole magnet is the basic component of the forward spectrometer and is available on a permanent loan basis from DESY, Hamburg. Figure 3.1 shows the magnet in the experimental area before the installation of the detectors. The magnet has a weight of 94 t. At ELSA the magnet operates with a maximum current I_{max} = 1340 A, which corresponds to a magnetic field in the centre of the magnet of B_{max} = 0.53 T, corresponding to a bending power of $\int B\,dl \approx 0.71$ Tm [BGO]. A reference Hall probe is located in the bottom left position in the middle of the magnet gap and measure a reference value of B_{max} = 0.43 T for that setting.
The gap of the magnet was extended from 544 mm to 838 mm. It increased the acceptance of the spectrometer magnet in vertical direction from ±5° to ±8°. The acceptance of the Open Dipole in horizontal direction is $\alpha_{hor} \approx \pm 12.1°$ for particle detection in the forward direction. After the extending the gap it was necessary to measure the magnetic field of the Open Dipole magnet because it changes the magnetic field and it was not done a mapping of the complete magnetic field of the Open Dipole before.

The measurements are performed by using Hall probes. Hall probes use the Hall effect, discovered by Edwin Hall in 1879. If current flows through a conductor in a magnetic field, which is not parallel to the current flow, the electrons are deviated inside the conductor by the Lorentz force. This generates an electric field which is perpendicular to the magnetic field and compensates the Lorentz force. The voltage U_H generated by this electric field is related to magnetic field $B_\perp$ component perpendicular to the current flow I:

$$U_H = A_H \frac{IB_\perp}{d}$$

there d is the width of the conductor and A_H is a the material constant called Hall constant.

3.1 Field mapping at GSI

Figure 3.2: Field measurement setup at the GSI. The 3 Hall probes are located at the end of the 3 meter long arm [Han].

In August 2009 the magnet was transported to the GSI (Gesellschaft für Schwerionenforschung) in Darmstadt to perform the necessary precise measurement of the magnetic field of the Open Dipole magnet. Figure 3.2 shows the measurement setup used at the GSI. To be able to measure a large volume three Hall probes are located at the end of a 3 meter arm. This arm is mounted to a tower which can be moved on a marble plate.

The field map was measured over the full inner volume of the Open Dipole with variable increments in the x (horizontal direction) and y (vertical direction) coordinates. The z (longitudinal direction) increment is fixed to 1 cm. The fringe field was also measured up to a distance of 1300 mm in front and 1800 mm behind the magnet. All three field components were measured simultaneously by a temperature stabilised high precision hall probe ($\Delta T = 10^{-4}$ T).

Figure 3.3 shows a xz plane of the field map at y = 0, measured at a current of I = 1340 A. The measurements were performed for three different setting with the reference Hall probe inside the magnet:

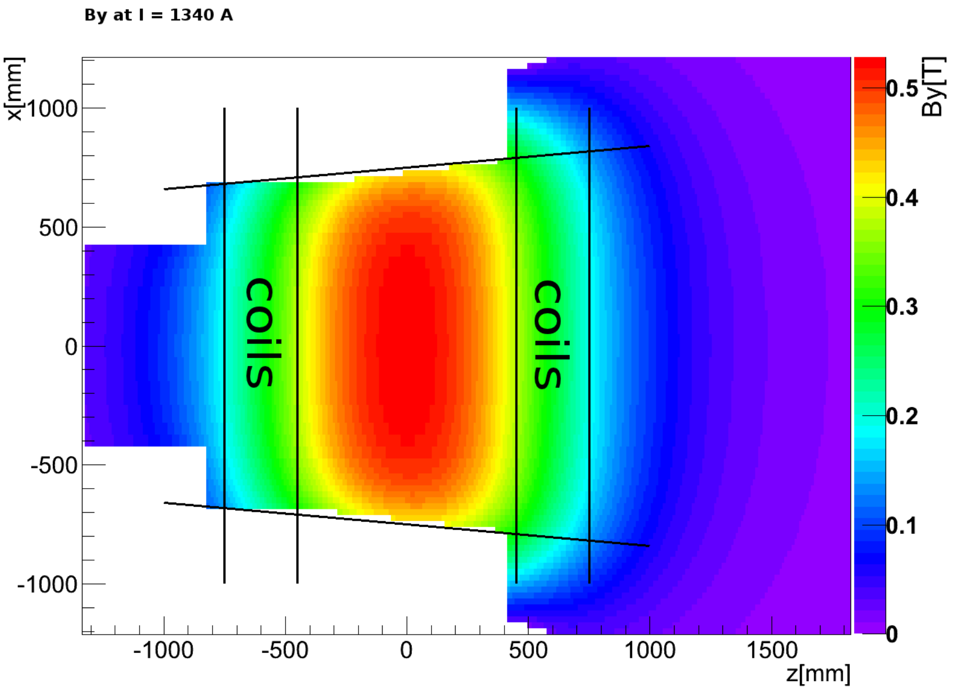

Figure 3.3: Magnetic field map over the full acceptance region of the (xz)-plane for the y-component of the field at I = 1340 A and y = 0 [BGO].

1. I = 940 A and 302 mT
2. I = 1140 A and 366 mT
3. I = 1340 A and 430 mT

In Figure 3.4 the y-component of the measured field along the photon beam axis is shown.

3.2 Field simulation

A simulation of the magnetic field of the Open Dipole magnet has been performed. This simulation is based on CST studio suite 2011 and all magnetic parts of the detector setup are included.

Figure 3.5 shows the ratio of data measured at the GSI and simulated data (with the GSI setup) for the y-component of the magnetic field at I = 1340 A. The plot shows small deviations at a level of few percent between the measured and the simulated B field.

The magnetic shielding of MOMO and SciFi2 photomultiplier tubes, not present at the GSI measurement, have been included in the simulation now together with all magnetic parts of the detector setup. Since figure 3.5 shows that the simulation does deviate from the real field, for a precise knowledge of the magnetic field it is necessary to measure the fringe field of the Open Dipole, where all the new magnetic material is now in place.

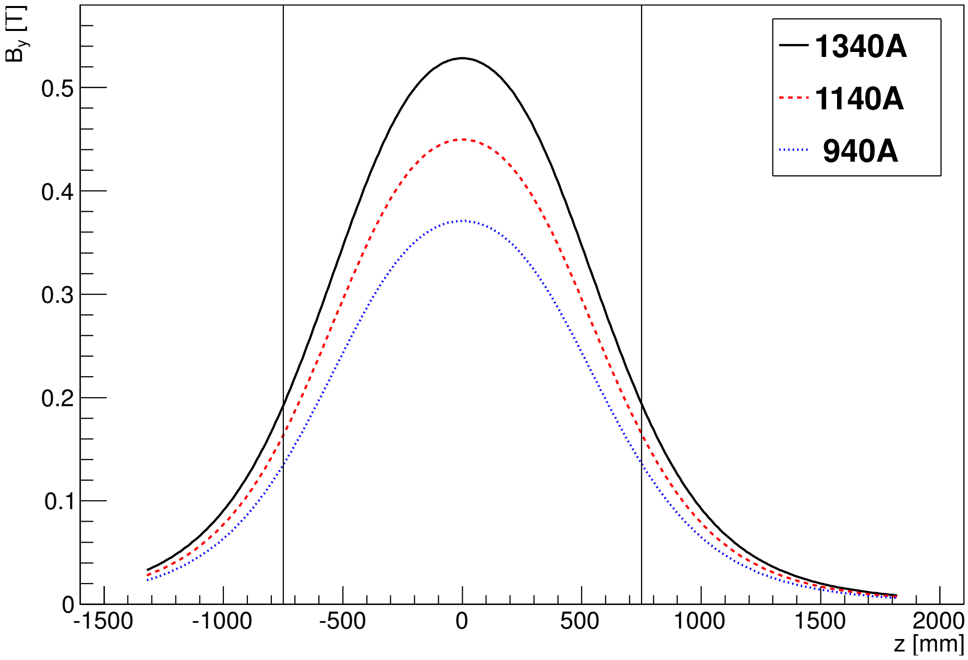

Figure 3.4: The y-component of the measured field at GSI along the photon beam axis for three different currents (legend inset). The two vertical black lines indicate the position of the magnet [Ham].

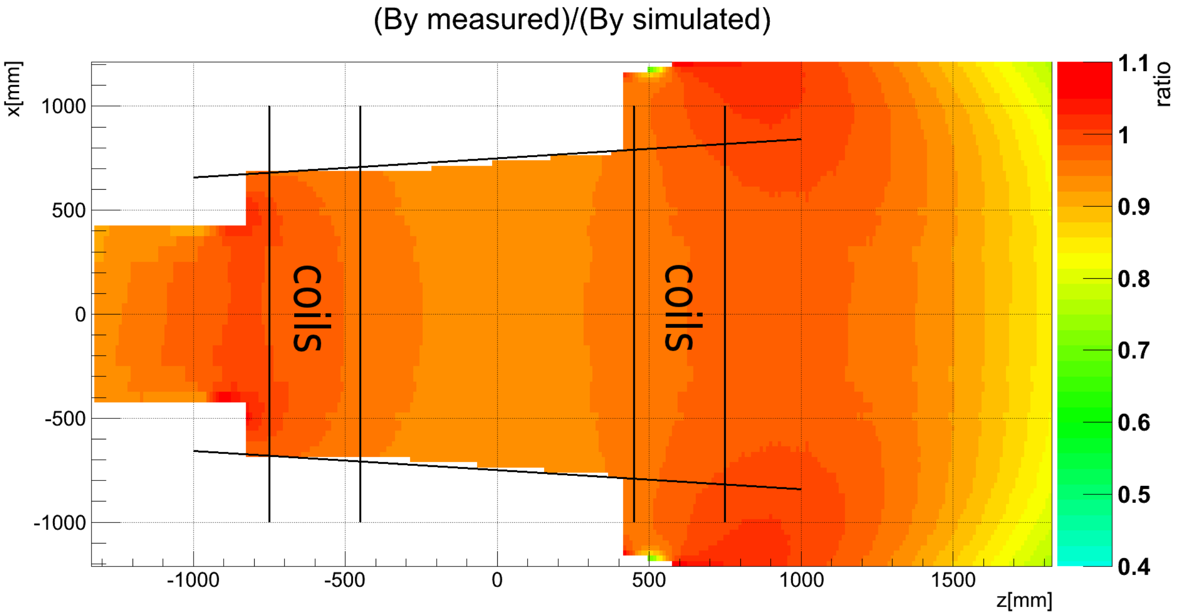

Figure 3.5: Ratio of the measured data at the GSI and simulated data with GSI setup of the y-component of the magnetic field at I = 1340 A and y = 0 [Ham].

Chapter 4

The Measuring System

In the following chapter, the setup for the in situ measurement will be described. It consists of a mechanical frame to hold the Hall probe, dedicated electronics to move it and the development of a user interface to perform the measurement remotely.
The project of the mechanical frame, the production/assembling and test of the electronic board, the program to control the motor movements and the development of the user interface are a substantial part of this diploma work.

The measuring system is an electric two axis linear system for the x- and y-direction powered by two step motors. It is manually movable in the z-direction (beam direction). A Hall probe is used to measure the magnetic field in front of the magnet and it is fixed to a carriage to be moved on the linear system. The Hall probe can measure the three dimensional components of the magnet field simultaneously. A laser tacker will be used to increase the precision in the readout of the position of the Hall probe.

The Hall probe is available on a loan basis from the ELSA group. It is a MPT-141-2s from Group3 Technology Ltd [Gro05]. The probe consists of three independent Hall probes installed in a holder, each probe can measure the magnetic field strength in one dimension. The simultaneous use of 3 probes allows for a 3D-measurement of the magnetic field with precision $\Delta T = 10^{-4}$ T.

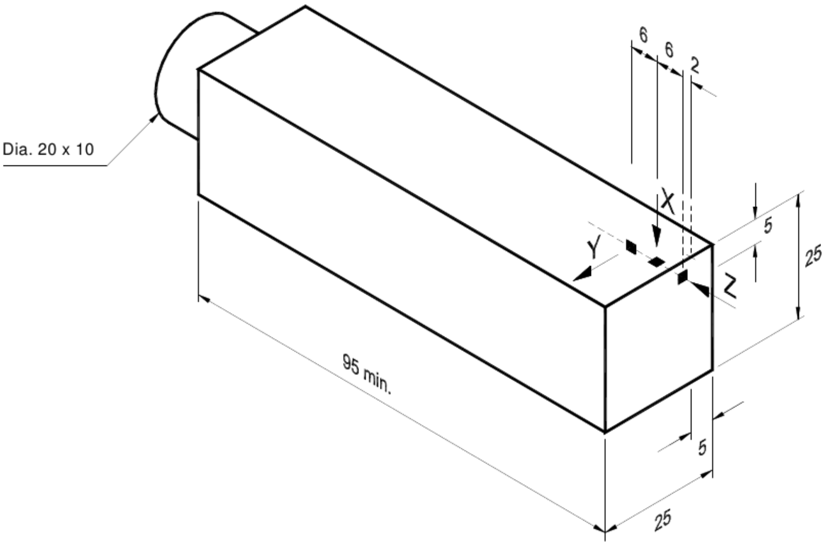

Figure 4.1: Layout of Hall probe holder. Active area of each Hall probe 0.5 mm × 1 mm. Materials: aluminium and 30% glass reinforced for the holder, plastic for the clams and nylon for the screws [Gro97]

Each probe is read by a DTM-151-DS teslameter from Group3 Technology Ltd [Gro07]. The precision of the teslameter readout is 0.01% of the reading. It is possible to perform up to ten measurements per second. The display of the teslameter shows eight digits while the measurement readout by a serial port allows for more precision measurement (up to 10 digits). The measurements can be performed by setting the teslameter range at the following values: 0.3, 0.6, 1.2, 3.0 Tesla or kilo Gauss. The temperature can also be measured and displayed. The working temperature range is between 0 °C and 50 °C . All three teslameters are read by a USB port connected to the serial port of the teslameters by an adaptor. These serial ports are configured to a baud rate of 9600, seven data bits and two stop bits. Figure 4.2 shows the three teslameters fixed in a small rack. For interaction with the teslameters there is a serial talk protocol [Gro07]. From now on, we will refer to the full system for the 3D measurement as the Hall probe.

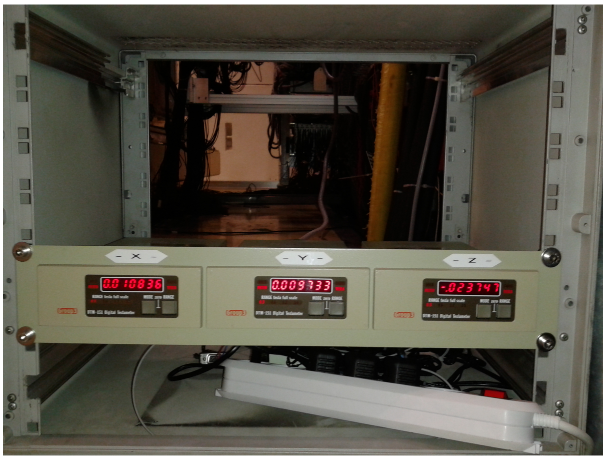

Figure 4.2: The three teslameters of the Hall probe fixed in a small rack.

4.1 Mechanics

A mechanical frame has been built to hold the Hall probe and to move it in the xy-plane of the experimental area. A non magnetic linear system from Franke GmbH is used as the main component of the mechanical construction for the in situ measurement. It consists of three aluminium rails (2100 mm long) and 5 carriages. Two rails are mounted parallel to each other at a distance of 6 cm on an aluminium profile. Together they build the horizontal axes (x-axes) of the construction (see figure 4.3). Two carriages are located in each aluminium rail. An aluminium adaptor plate is fixed on the four carriages, so that it can be moved by a simultaneous translation of the 4 carriages by the use of a step motor. The step motor is mounted at the right end of the top aluminium body.
On the aluminium adaptor plate, the third aluminium rail is fixed perpendicularly to the two other rails, in the vertical direction. A non magnetic carriage can run along the vertical rail by a rubber gear belt moved by the second step motor. A further aluminium construction is used to fix the Hall probe holder on the carriage. A photograph of the Hall probe on the carriage is shown in figure 4.4. This construction allows for movements of the Hall probe in the xy plane remotely.

All the parts which can affect the magnetic field of the Open Dipole (horizontal bars, the two step motors and the 4 carriage for the horizontal movement) are located in the top part of the construction.

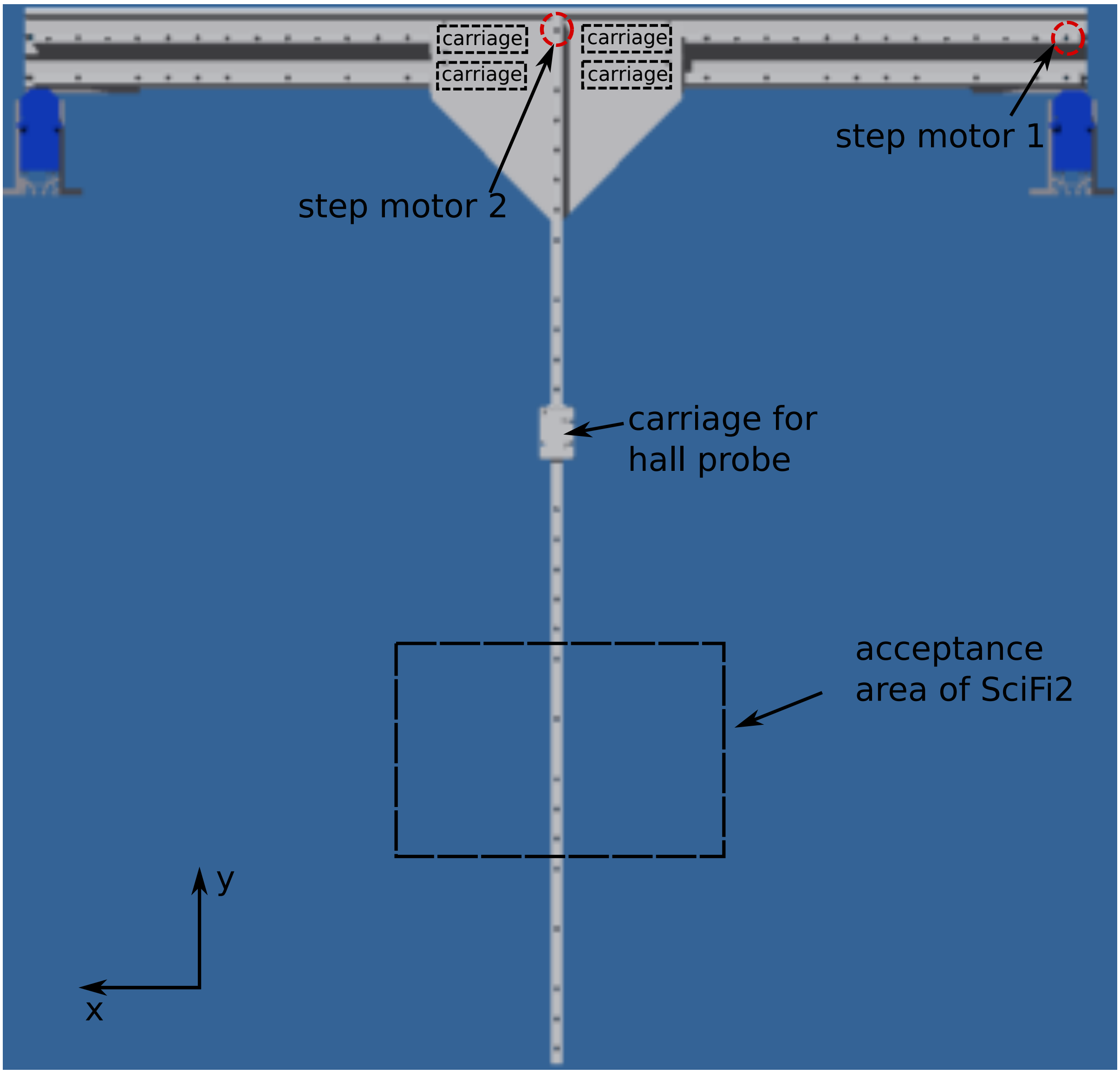

Figure 4.3: Drawing of mechanical part of the measuring construction with the attachment to the magnet. The two step motors are indicated. Step motor 1 in the top right corner of the construction is for the movement along the x axis. The second step motor (top in the middle) is used to rotate the rubber gear belt and move the non magnetic carriage in the vertical direction. The other four carriages are suggested by dashed line on the top rails under the adaptor plate on the top middle of the drawing.

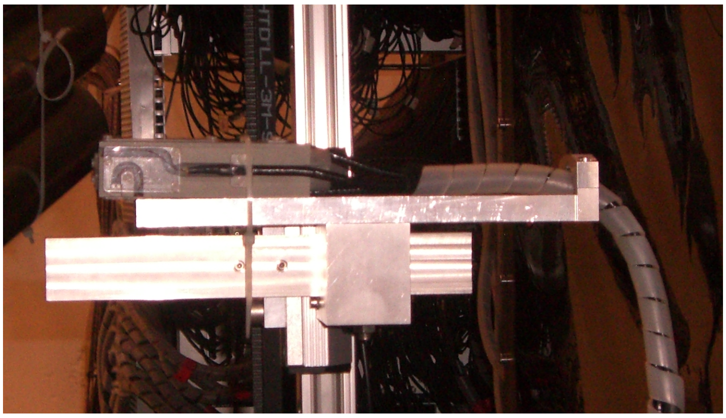

Figure 4.4: Hall probe fixed to the holder on the carriage.

It is possible to move the construction manually along the z direction (beam direction) in the experimental area. The horizontal part of the construction is fixed on two other carriages which can be moved along two rails which sit on two $80 \times 160\,\mathrm{mm}^2$ and 2400 mm long aluminium profiles. The two profiles together with the rails are part of the holding structure of MOMO. They are fixed on top of the open dipole magnet and are arranged between the magnet and the BGO ball. This enables measurements of the fringe field between the BGO ball and the open dipole magnet, where MOMO and SciFi2 are positioned.
The holder of the Hall probe can also be moved 20 cm (along the longitudinal direction) to move it as close as possible to MOMO and SciFi2 detectors.

Figure 4.5 shows a side view of the mechanical frame, the vertical aluminium body, Hall probe on the bottom, the second step motor and a part of the horizontal profile on the top.

4.2 Electronics

Two Python ZSS 57 step motors are used with an additional 16:1 gear to give higher torsional moment. The Step motors move 200 steps per rotation and have holding torque of 700 mN·m [Phy]. A three channel encoder (Nanotec HEDL-5540 A14) is attached to each step motor and counts 500 steps per rotation [Nan]. The encoder will be used for getting information of the current position from the construction which will be moved by the step motors, if no laser tracker is used.
For controlling the step motors a PololuA4988 step motor driver and a Atmega23u4 micro controller are used. Before they were soldered on a board, the chips were tested on a breadboard to find the optimal setup. Figure 4.6 shows a picture of the test setup with a smaller step motor than the one used in the construction.

The schematics of the controlling board for the step motors is shown figure 4.7. On top of the diagram there is shown the micro controller connected to the step motor driver (at the bottom of the diagram), the encoder and two limit switches. The micro controller is connected to a computer by a mini USB port. The computer also provides the required voltage for the encoder and for the step motor driver. At the step motor driver, the step motors and a 24 V power supply for the step motors are connected. There is one capacitor between the step motor driver and the power supply and two capacitors between the 5 V

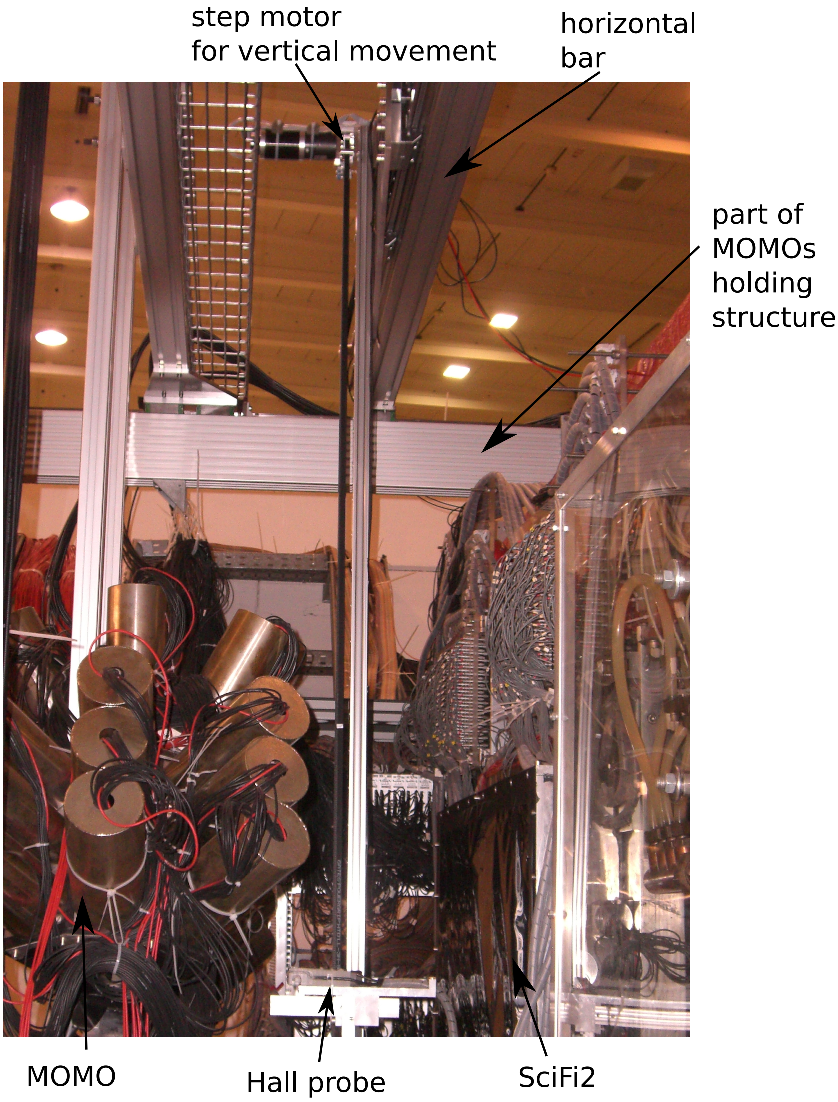

Figure 4.5: The mechanical construction between MOMO and SicFi2 with the Hall probe fixed on the holder on the bottom of the photograph. The step motor for moving in the vertical direction is shown at the top of the photograph.

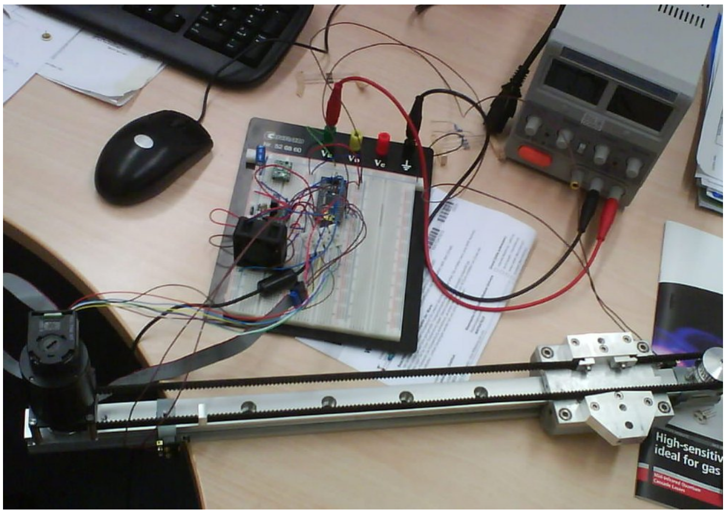

Figure 4.6: Test setup with a smaller step motor for testing the micro control Atmega23u4 and the step motor driver PololuA4988.

for the supply of the micro controller and the step motor driver to protect it from current fluctuations.

The user can send commands to the micro controller by a virtual serial port, provided by the USB port of the micro controller. The program which will be used for sending commands to the micro controller is explained in section 4.3. As soon as the micro controller gets a command for the step motors, a signal is sent to the step motor driver. The step motor driver converts the incoming signal into an impulse and sends it to the step motor, which then starts to move the carriage in the indicated direction. For all the other commands (for example, the read out of the probe position), the micro controller reads the information from the encoder.

At both ends of the vertical and the horizontal aluminium body which are used as the guide rails for carriages, limit switches are mounted. If the carriage moves into one of the limit switches the micro controller receives a signal and stops sending the signal to the step motor controller that should move the step motor. The carriage stops immediately, to save the step motor and the construction from damage. After stopping the step motors, the micro controller sends a signal to the step motor controller to move the carriage in the opposite direction until it is no more in contact with of the limit switch.

The board is installed in a plastic box with two air coolers on one side and holes on the other side for a good air stream. The cooling is necessary to prevent the micro controller from overheating. The step motor driver has an overheat control which switches it off if it gets too hot. Since the current flow in the step motor controller reaches values up to 1.2 A, an additional cooling body is used for the chip. Figure 4.8 shows a picture of the open box with the controlling board fixed inside and the two air coolers at the upper side of the box. The connectors for the encoder, limit switch and the step motors are on the right side of the box, on the left side there is the connector for the power supply and a hole for the micro USB cable. Both step motors have their own micro controller board in independent boxes with air cooling, which are fixed beside the corresponding step motor on the mechanical construction.

A serial protocol is used for the communication with the micro controller. Table 4.1 shows a list of

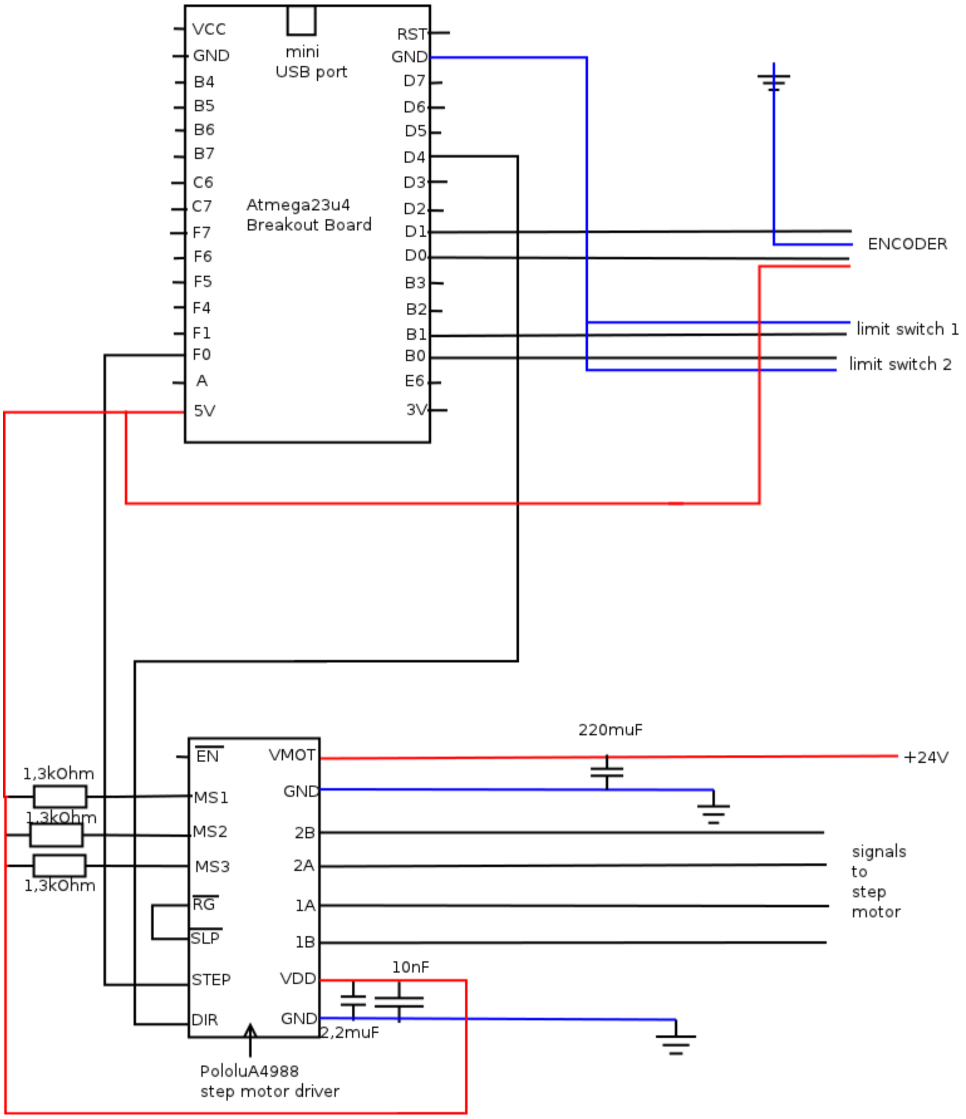

Figure 4.7: Schematic drawing of the connections for the controlling board of the step motors with a micro control Atmega23u4 and a step motor driver PololuA4988

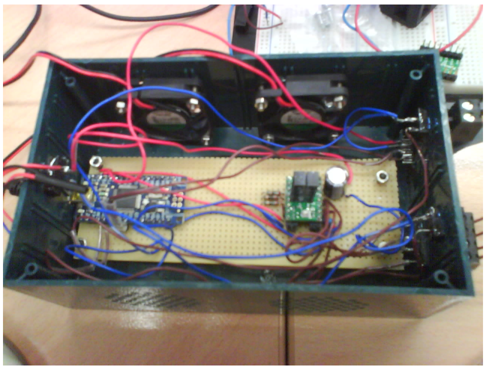

Figure 4.8: Box with the controlling board for one step motor is fixed inside. Connectors for encoder, limit switch, step motors and power supply on the small side of the box, two air coolers on the long side of the box are shown.

the existing commands, error messages and info messages which the micro controller sends.

command	effect
“P“, “p“	read the current position
“W“, “w“	read the final position
“G“, “g“ and value of steps (+ means forward, - means backward)	movement of the value steps in desired direction
“T“, “t“ plus a value for the desired position	moves to the desired position
“R“, “r“	set current position to zero
“S+“, “s+“	moves one step in forward direction
“S-“, “S-“	moves one step in backward direction

error messages	meaning
“Error: Unknown command“	the program does not know the command
“Error: Direction missing“	+ or - are forgotten by command “S“

info messages	meaning
“Info: Limit Switch reached!“	carriage was moved against a limit switch by the step motor
“Info: Movement Stopped!“	step motor stops moving

Table 4.1: List of commands for the micro controller and of messages from the micro controller.

4.3 Control program

The control program is written in Qt. Qt is a cross platform application framework. It uses the programming language C++ and is used for software applications with a graphical user interface. The program can connect to both step motor controllers and the teslameters to enable the complete control with one program.

In figure 4.9 the graphical user interface is shown. The user interface is subdivided into three parts. On the left the “Controls“ box, in the middle the “Measurement“ box and of the right side the information part.

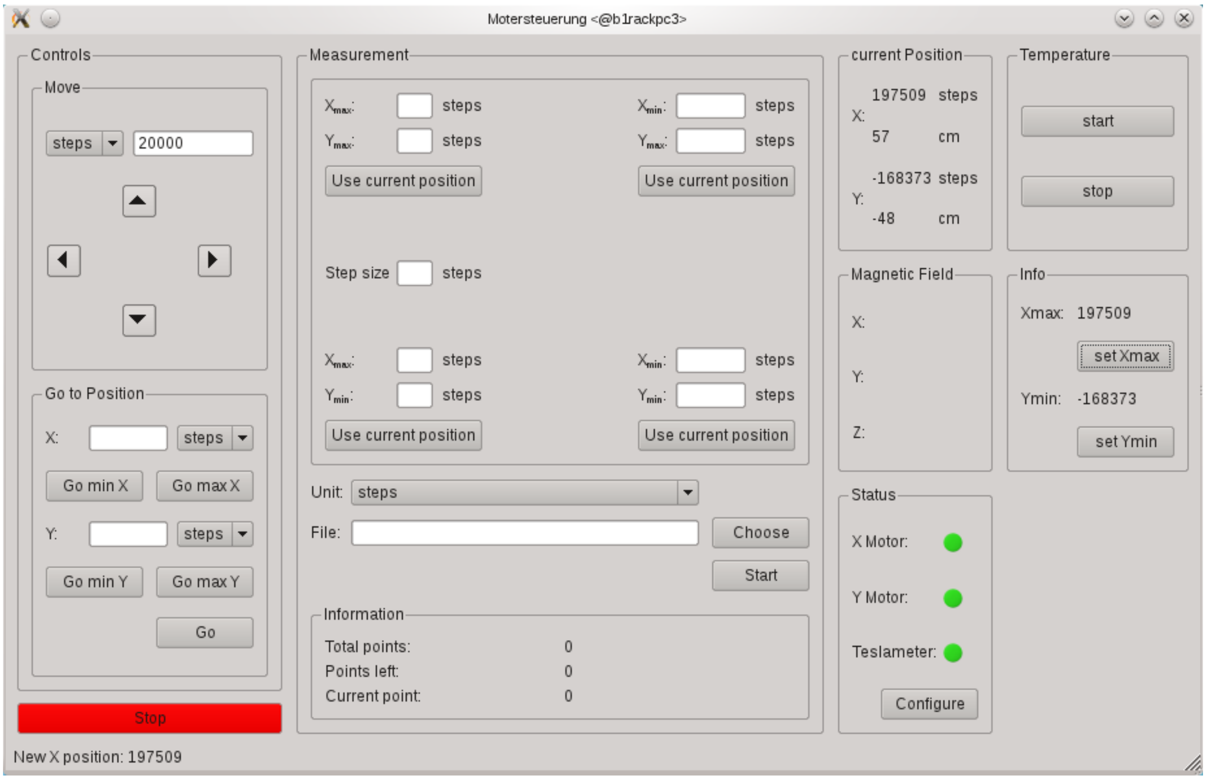

Motersteuerung <@b1rackpc3>

Move: steps 20000

current Position: X: 197509 steps, 57 cm; Y: -168373 steps, -48 cm

Info: Xmax: 197509; Ymin: -168373

Unit: steps

Information: Total points: 0; Points left: 0; Current point: 0

New X position: 197509

Figure 4.9: Graphical user interface to control the step motors and the Hall probe and to perform automated measurements.

At first the user has to connect the two step motors and the teslameter. In the bottom right of the user interface there is the “Status“ box (figure 4.10). It shows the status of the connection from the two step motors and the teslameters for the Hall probe. Green points indicate that they are connected, red points indicate that they are not. There is also a “Configure“ button which opens an extra dialogue window. In this window the user can tell the program at which serial port the step motors and the teslamaters are connected to the computer. Figure 4.11 shows this extra window other lapped on the user interface.

If the step motors and the teslameter are connected the user has the option to move the Hall probe or to start a measurement. For moving the Hall probe, the user has two possibilities. On the left side of the user interface under “Controls“ (figure 4.12) the two different methods to move the Hall probe are located.

By the upper box “Move “ the construction can be moved relatively to the current position. By clicking on one of the four arrows the step motors will move the construction in the required direction with respect to the beam direction in the area. The distance of the movement will be given by the number that the user writes into the white box on top of the arrows. On the left of the white box there is a unit button which can be switched between steps in cm, in which 1 cm is equivalent to 3448 steps.

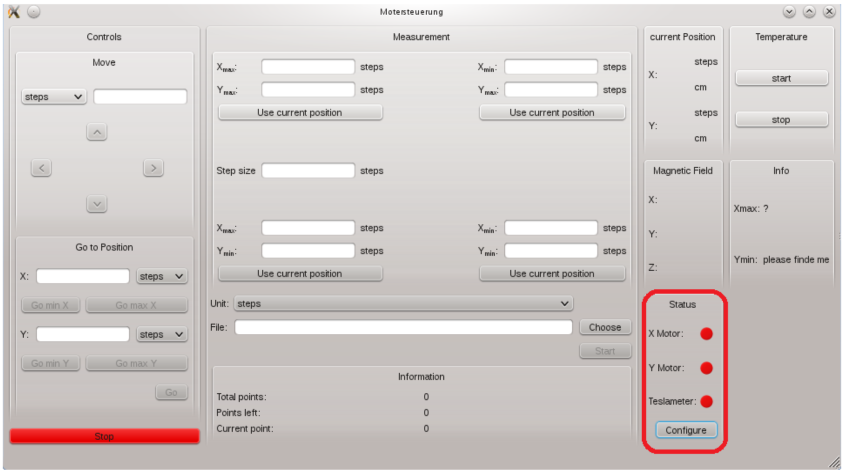

Unit: steps

Figure 4.10: User interface, the box for connecting is highlighted by a red frame.

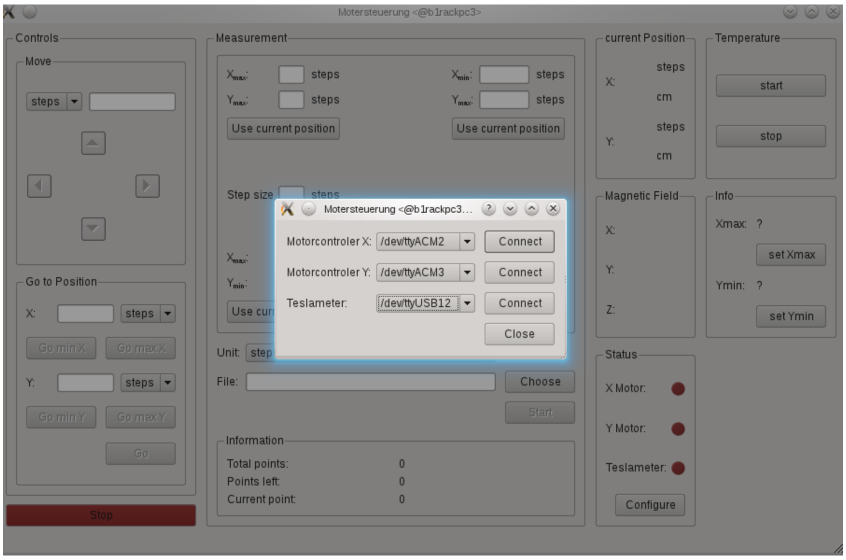

Motorcontroler X: /dev/ttyACM2
Motorcontroler Y: /dev/ttyACM3
Teslameter: /dev/ttyUSB12

Figure 4.11: The extra window in front of the user interface is used for giving the program the information at which serial port of the computer the step motors and the teslameter are connected.

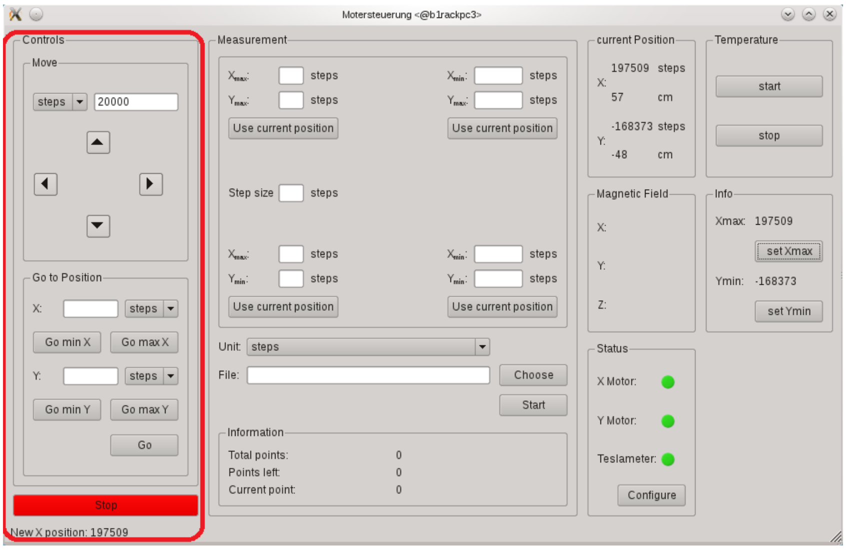

Move: steps 20000

current Position: X: 197509 steps, 57 cm; Y: -168373 steps, -48 cm

Info: Xmax: 197509; Ymin: -168373

Unit: steps

Total points: 0
Points left: 0
Current point: 0

New X position: 197509

Figure 4.12: User interface, the boxes for moving the construction are highlighted by a red frame.

The second method to move the construction to an absolute position is given in the lower big left box “Go to Position“. There are two white boxes for the x-coordinate and the y-coordinate. In these boxes the user can write the desired x- and y-position. Beside the white boxes there are also unit buttons which can switch between steps and cm. When the user clicks on the “GO“-button (bottom right in this box) the Hall probe will be moved by the step motors to the given position. If one of the white boxes is empty, the program does not change the current position in this direction and controls the movement only in the other one.
Below each of the two white boxes there are two buttons for moving to the minimal and maximal position in x and y. The step motors will move the construction until it reaches the corresponding limit switch and then will be stopped.
For both the methods, the button for moving commands are disabled if the step motors are not connected. On the bottom left side under the movement boxes a “stop“ button is located, which stops the movement by getting clicked.

In the centre of the user interface the “Measurement“ box is located (figure 4.13). In this box the user can set all parameters which the program needs to perform an automatic measurement. In the upper half of the window there is a box in which the user must write down the extreme points of the area which should be scanned. Among the fields for the extreme points there is a “Step size“ field where the user must write a value for distance between the points in the area which should be measured.
The bottom half of the “Measurement“ window starts with a box where the user can choose between steps and cm as a unit for the values he tipped before. The user has to write the name of the output file in which the measured data will be stored.
In this text file the program will write the measured data in six columns. In the first column the program writes the current time at which the measurement was taken at a certain point, in the second column it writes the current x-position and in the third the current y-position of this point in steps. In the columns four to six the program writes the measured values of magnetic field in mT at that point and time: in

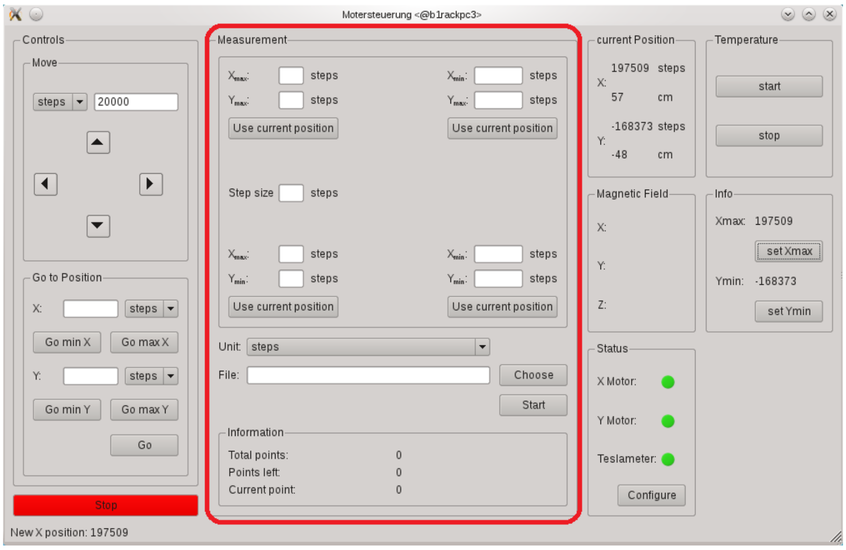

Move: steps 20000

Measurement: X_{max}: steps, X_{min}: steps, Y_{max}: steps, Y_{max}: steps; Step size steps; X_{max}: steps, X_{min}: steps, Y_{min}: steps, Y_{min}: steps

Unit: steps

File:

Information
Total points: 0
Points left: 0
Current point: 0

current Position
X: 197509 steps
57 cm
Y: -168373 steps
-48 cm

Magnetic Field
X:
Y:
Z:

Info
Xmax: 197509
Ymin: -168373

Status
X Motor: ●
Y Motor: ●
Teslameter: ●

New X position: 197509

Figure 4.13: User interface, the box for setting a measurement is highlighted by a red frame.

the fourth column B_x, in fifth column B_y and in the sixth column B_z. By clicking the start button the program starts the automatic measurement. If some information is still missing the program displays an error message.

On the bottom of the centre box, there is a box which shows the information about the measurement. It shows how many points in total will be acquired, how many are still missing and how many are already measured.

The automatic measurement is done as follows. At first the program calculates with the information of the basic points and the step size, a grid of all the positions where the measurement must be performed. The measurement starts at X_{min} and Y_{min}. After the Hall probe is moved to this point the measurement starts. First all y-points at X_{min} were measured upwards from Y_{min} to Y_{max}. After this, it moves to the next x-point and measures all y-points from Y_{max} to Y_{min} and so on until all points are measured. The effect of the reversal error disregard in basis of a positioning error of 2 cm (explain in chapter 5) without using the laser tracker. By using the laser tracker the effect can be disregard because it measure the correct position.

During the movement of the Hall probe it was noticed that the reference position of the entire construction could change slightly due to mechanical strain. This was most pronounced for a movement of the Hall probe in the horizontal (x) direction. To correct for this effect, the measurements are performed by scanning the vertical direction for each horizontal step. At each point the program measures the magnetic field value several times until two consecutive measurements are within $\Delta = \pm 0.1$ mT and stores this value.

On the right side of the user interface there are three status boxes shown in figure 4.14. The box “current Position“ shows the current x- and y-position of the Hall probe in steps and cm. The next box “Magnetic Field“ shows the last measured values of the x-, y- and z-components of the magnetic field in mT and the third box corresponds to the status of the connections.

On the right side two additional boxes are located (figure 4.15). The “Temperature“ box allows a

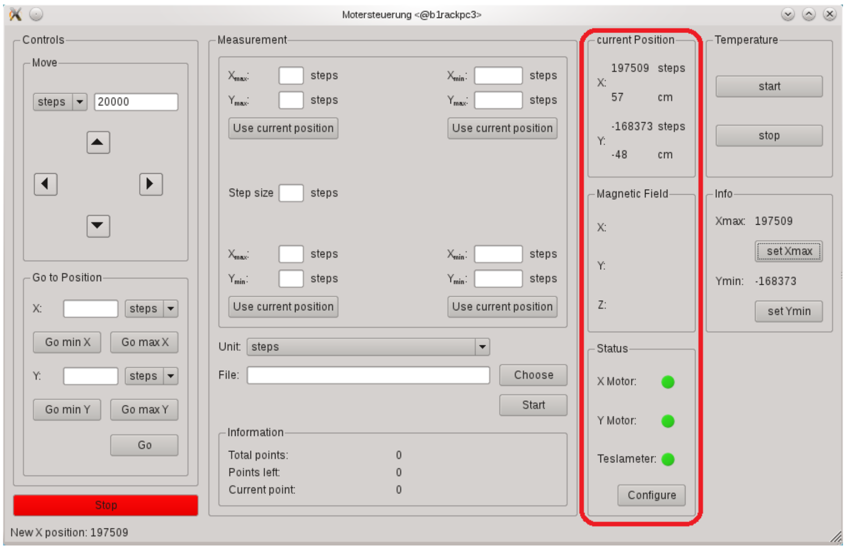

Motersteuerung <@b1rackpc3>

Move: steps 20000

current Position
X: 197509 steps
57 cm
Y: -168373 steps
-48 cm

Info
Xmax: 197509
Ymin: -168373

Unit: steps

Information
Total points: 0
Points left: 0
Current point: 0

New X position: 197509

Figure 4.14: User interface, the three info boxes are highlighted by a red frame.

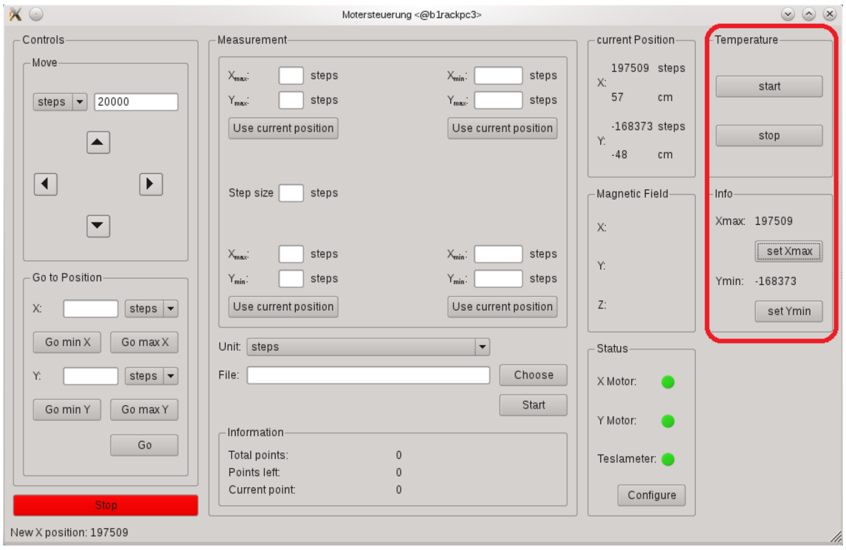

Motersteuerung <@b1rackpc3>

Move: steps 20000

current Position
X: 197509 steps
57 cm
Y: -168373 steps
-48 cm

Info
Xmax: 197509
Ymin: -168373

Unit: steps

Information
Total points: 0
Points left: 0
Current point: 0

New X position: 197509

Figure 4.15: User interface the boxes for temperature measuring and reference points are highlighted by a red frame.

measurement of the temperature of the Hall probe over a long period of time. This is useful to find out if there are a effect by temperature variations on the precision of measurements of the Hall probe.
The “Info“ box below displays the maximal x-coordinate and the minimal y-coordinate in steps. These points will be set by moving the corresponding limit switch or by clicking the buttons when the construction is at the desired position. When the measurements are done without laser tracker these two points are needed to convert the coordinate of the measurement system into the coordinates system of the experimental setup. The minimal y-position of the Hall corresponds to -265 mm with respect to the centre of the magnet and at the maximal x-position corresponds to 524 mm with respect to the centre of the magnet. The z-position must be measured by the user with a laser distance meter and a plumb.

4.4 The laser tracker

The Geodätische Institute of the University of Bonn owns a Leica absolute tracker AT901. This will be used to determine the absolute position of the Hall probe in our experimental setup coordinates for improving the accuracy of the position measurements. The origin of this coordinate system is the centre of the magnet. The laser tracker system is able to measure the position of the Hall probe for the three space coordinates (x, y, z) simultaneously with a positioning accuracy of ≈ 0.1 mm[Lei08].

Chapter 5

Measurements

The following chapter shows the in situ measurements, compare they with the measurements done at the GSI and simulated magnetic field data. In the last part of the chapter an analysis of the momentum reconstruction using simulated data are done.
To measure one xy-plane takes half a day, to ensure that temperature changes of the Hall probe and the teslameter electronics do not effect the measurement. A measurement of the sensitivity to temperature of the Hall probe and the readout electronics of the teslameters were done. The Hall probe was fixed in a box together with a small permanent magnet and kept in a constant magnetic field. Then over two days the magnetic field and the temperature were measured every five minutes and written in a text file by the control program. Figure 5.1 shows the measured temperature against the measured z component of the constant magnetic field (the magnetic field was oriented to the z component of the Hall probe). The measurement shows that there is a correlation between the measured magnetic field and the temperature, for lower temperatures the Hall probe measured a higher magnetic field values. The variation of measured field is in the region of 0.07 mT for temperature changes of 4 °C, which is consistent with the given precision of $\Delta T = 10^{-4}$ T of the Hall probe.

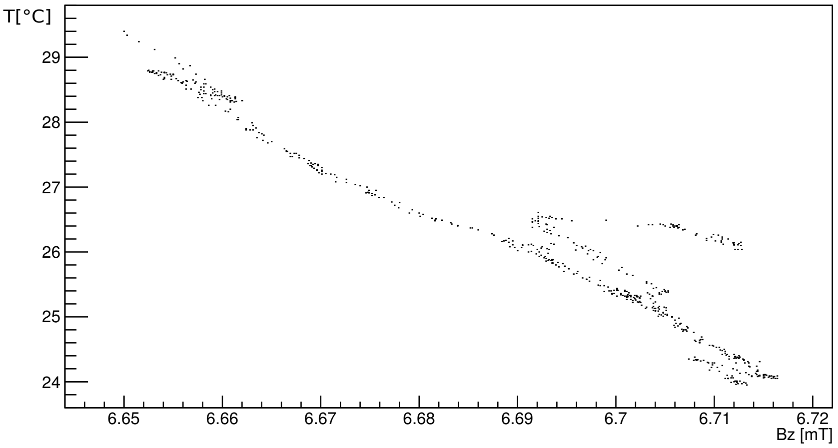

Figure 5.1: Changes of measured values of a constant magnetic field at different temperatures.

The fringe field of the Open Dipole was measured in xy-planes between MOMO and SciFi2 without using a laser tracker for the position. The closest xy-plane to MOMO is located at position z = -1557 mm and the closest xy-plane to SciFi2 is located at position z = -1065 mm relative to the centre of the magnet. In total 15 z positions have been measured as shown in figure 5.2.

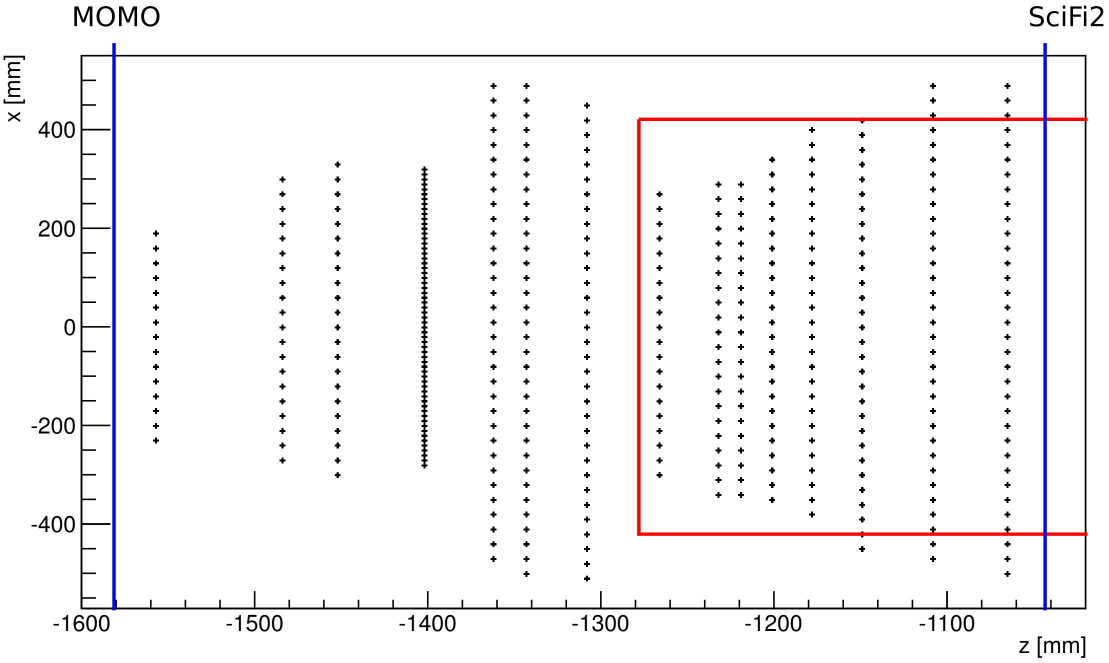

Figure 5.2: Position along z of the measured xy-planes magnetic field maps. Z coordinates indicate the distance between the measurement set-up of the Open Dipole magnet. The blue lines show the position of MOMO and SciFi2. The red lines mark where reference measurements from the GSI exist.

The red lines mark the area of existing measurements at the GSI and the blue lines mark the position of MOMO and SciFi2. The reason why the xy-planes having different ranges in x is that the construction of MOMO and its shielding limit the accessible space at every position and also because the Hall probe holder was rotated. From z = -1557 mm to z = -1308 mm the Hall probe holder was rotated to measure the field near MOMO; for the other planes Hall probe holder was orientated to SciFi2. The gap of the points in the horizontal and vertical direction is 3 cm. Only the plane at z = -1402 mm is measured with a gap of 1 cm to check whether the 3 cm gap is sufficient. It was found that the changes in 1 cm distances are small so that there is no problem to measure with a gap of 3 cm. The measurements of the Open Dipole at the GSI were also done with a similar gap. All measurements were done by a reference value of 430 mT of the reference Hall probe inside the Open dipole (the required current was ≈1305 A).

The measurement of the position along the z direction was done by a hand laser tracker and a plumb. The distance was measured several times at each position. The value of the z position was taken as the average of these results with an error of 5 mm. The positioning of the x- and y-coordinate is given by the encoders, and to translate into the reference system two reference points are measured at the minimum y position and maximum x position. The measurement of these points in the reference system were done with a plumb line, ruler and a spirit level by two people by hand. Several factors contribute were the error of the translation from the construction system to the reference system, giving a realistic error of 20 mm. In the future this error can be reduced to about 1 mm by measuring the position of the Hall probe with the laser tracker.

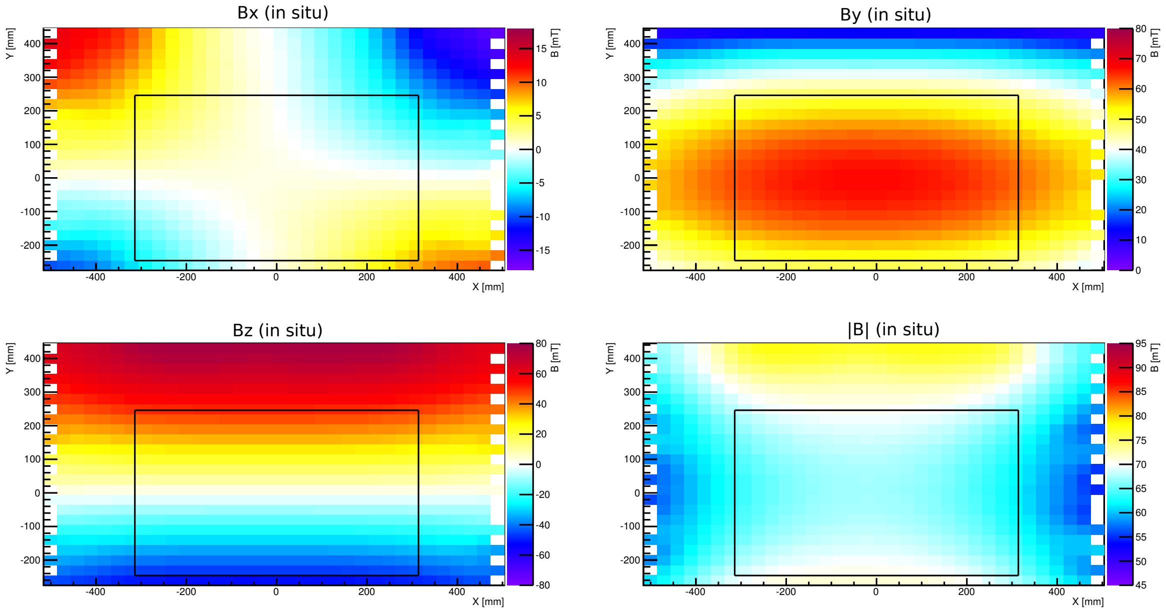

Figure 5.3: Four magnetic field maps of the xy-plane at z = -1065 mm (close to SciFi2) for the x-, y- and z-components and |B| measured in situ. Top left corner: B_x; top right corner: B_y; bottom left corner B_z; bottom right corner: |B|; The colour code shows the field intensity in mT. The black box marks the acceptance area for charged particles. The measurements are done with a magnetic field of 430 mT.

Figure 5.3 shows the in situ measured magnetic field maps of the xy-plane at z = -1065 mm (close

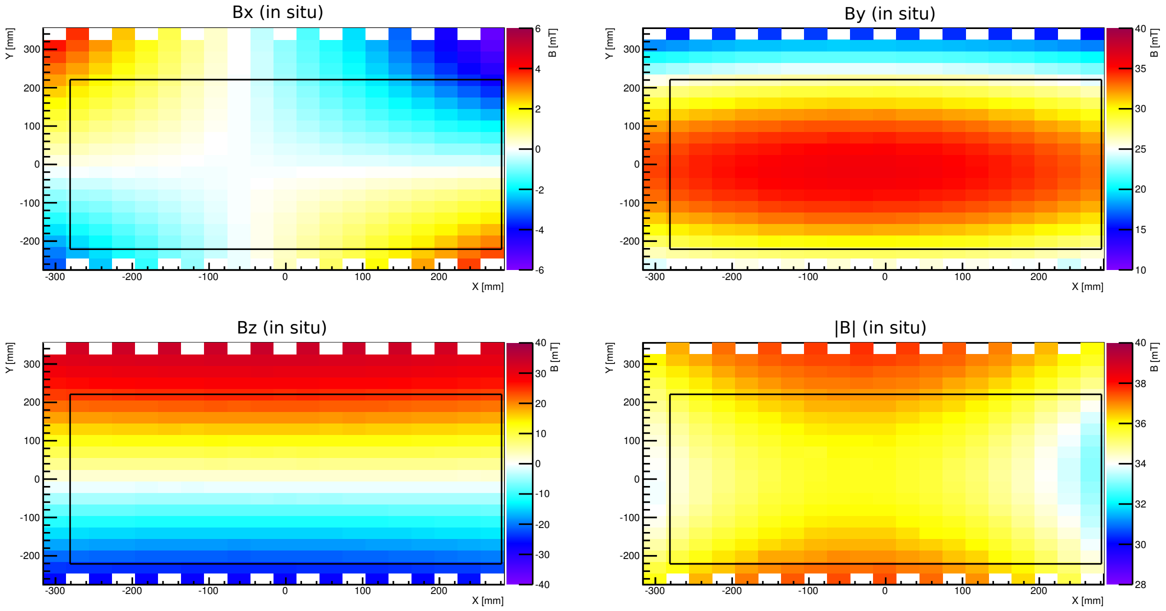

Figure 5.4: Magnetic field maps of the xy-plane at z = -1266 mm for the x-, y- and z-components and |B| measured in situ. Arranged in the same order as figure 5.3. The colour code shows the field intensity in mT. The black box marks the acceptance area for charged particles. The measurements are done with a magnetic field of 430 mT.

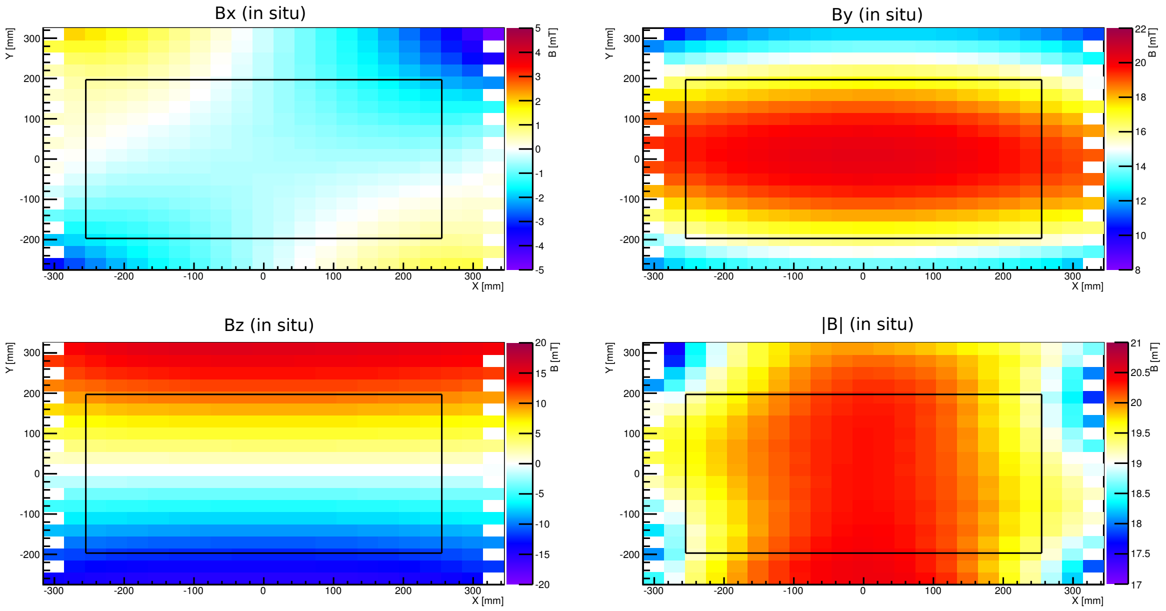

Figure 5.5: Magnetic field maps of the xy-plane at z = -1452 mm for the x-, y- and z-components and |B| measured in situ. Arranged in the same order as figure 5.3. The colour code shows the field intensity in mT. The black box marks the acceptance area for charged particles. The measurements are done with a magnetic field of 430 mT.

to SciFi2). Figure 5.4 shows the in situ measured field maps for the xy-plane at z = -1266 mm (in the middle of the measured region) and the magnetic field maps of xy-plane at z = -1452 mm (close to MOMO) are shown in figure 5.5. The other in situ measured field maps of the 12 additional xy-planes are shown in appendix A. The range of the field intensity (colour code) is different for each field map and at each different xy-plane.
The field maps show the same structure for each component in each different plane. The magnetic field is oriented in the y direction. In the centre of the magnetic field the y component has the highest value and decreases to zero in the direction y and -y at the borders of the field. The z component is the opposite, with maximum values at the border of the field in y and -y direction. The z component must be zero at the magnet centre and changing in sign at that point. The x component also switches in y and x direction from positive to negative values. The x-component is the smallest.
The y-component of the magnetic field shows clearly that the magnetic field decreases with increasing distance to the magnet, at z = -1065 mm (closes to SciFi2) $B_{ymax} \approx 70$ mT and at z = -1452 mm B_{ymax} decreases to ≈ 20 mT. |B| changes in the same way.

For the following comparison of the results of the in situ measured magnetic field maps with the measured field maps at the GSI and the simulated field of the Open Dipole, the 6 mm gap between the three Hall probes in the holder was accounted for. The z-position values corresponded to the z-position of the Hall probe in the middle of the holder (the one which measured the x component of the magnetic field). The z-position of the Hall probe which measured the z-component of the magnetic field is -6 mm of the given z-position and +6 mm is the position of the Hall probe which measured the y-component of the magnetic field when the Hall probe is orientated to MOMO. For orientation to SciFi2 it is the opposite.

5.1 Comparison with data measured at the GSI

A comparison of measurements at GSI and the in situ measurements is required to find out the effects of the shielding of the photomultiplier tubes of MOMO and SciFi2 on the magnetic field and the magnetic parts of the detectors which were not present at the GSI measurements. Figure 5.6 shows the field maps of the xy-plane at z = -1065 mm (close to SciFi2) measured at the GSI. The corresponding in situ measurements are shown in figure 5.3. The structure of the field maps between the in situ measurements and at GSI look similar for each different map.

Figure 5.7 shows the difference between the in situ and the GSI magnetic field maps of the xy-plane at z = -1065 mm (close to SciFi2) for the x-, y- and z-components of the magnetic field and |B|. The corresponding ratios of the two measurements are shown in figure 5.8. Values which are smaller than the precision of the Hall probe (0.1 mT) were set to zero.

The x component shows a white cross in the ratio (figure 5.8) in the region where the values of B_x are zero. There is also an asymmetric shift to -x direction and a smaller shift to -y direction visible. The ratio of the z-component of the magnetic field (shown in the bottom right corner) shows that the plane where field switches from positive to the negative values is shifted between the in situ and GSI measurements. The total differences are very small, for the x and z component the values cover only -3 mT to 3 mT. The differences values of the y component are around -6 mT and increases to -8 mT in the (x, y) corner of the field map. In the (-x, -y) direction of the field map, the difference decreases to

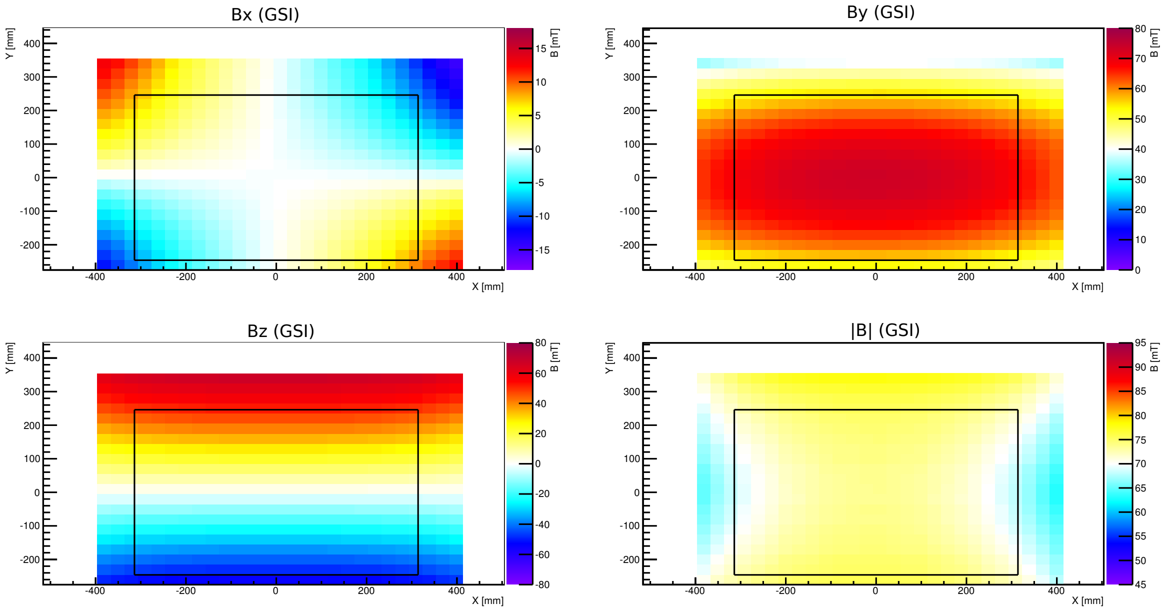

Figure 5.6: Magnetic field maps of the xy-plane at z = -1065 mm for B$_x$, B$_y$, B$_z$ and |B|-field measured at the GSI. Arranged in the same order as figure 5.3. The colour code shows the field intensity in mT. The black box marks the acceptance area for charged particles. The measurements are done with a magnetic field of 430 mT.

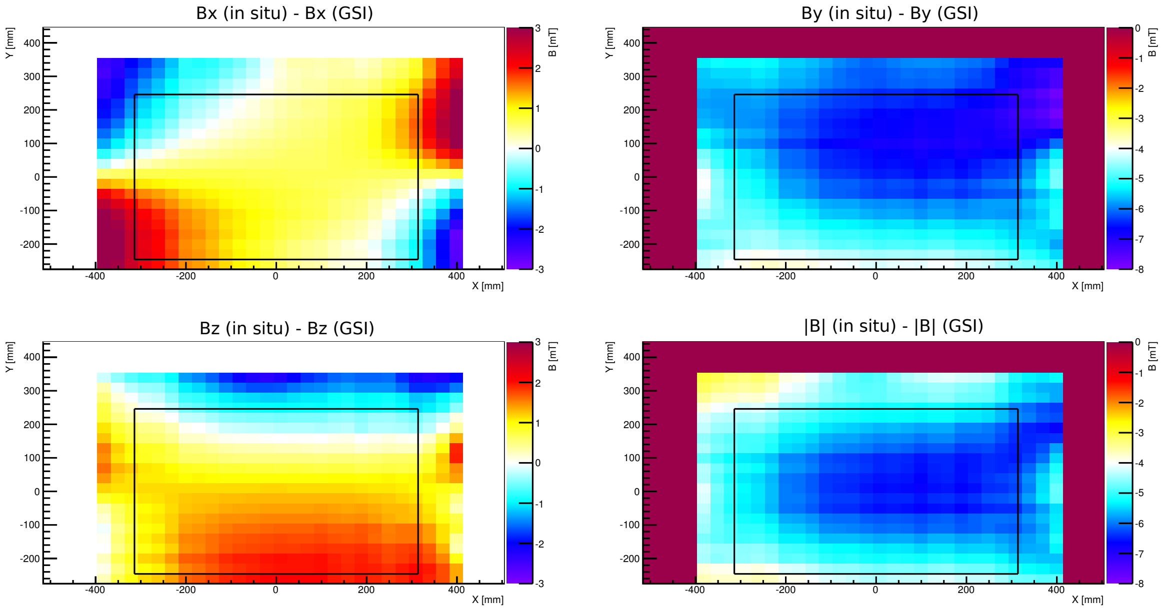

Figure 5.7: Difference between the in situ measured and at the GSI measured magnetic field maps of the xy-plane at z = -1065 mm for the x-, y- and z-components and |B|. Arranged in the same order as figure 5.3. The colour code shows the total different of the measured values in mT. The black box marks the acceptance area for charged particles. The measurements are done with a magnetic field of 430 mT.

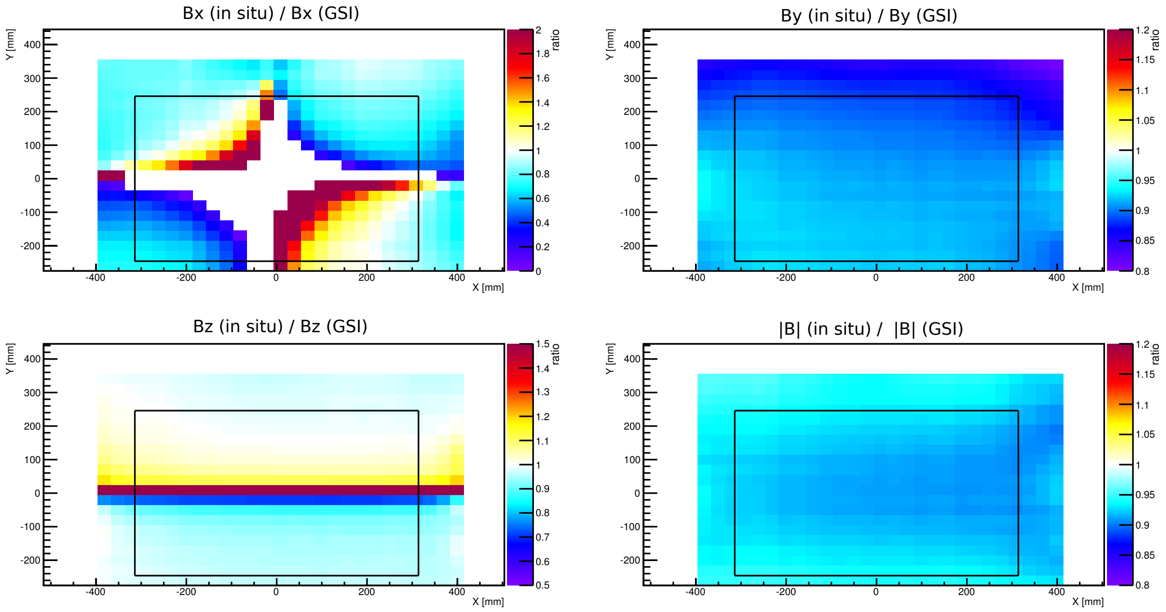

Figure 5.8: Ratio of the in situ measured and at GSI measured magnetic field maps of the xy-plane at z = -1065 mm for the x-, y- and z-components and |B|. Arranged in the same order as figure 5.3. The colour code shows the ratio. The black box marks the acceptance area for charged particles. The measurements are done with a magnetic field of 430 mT.

-4 mT. Also the ratio difference varies from around 10 % in -y area up to 20% for higher y values. The ratio in the middle of the acceptance area of |B| is about 90% and goes up to about 95%. The difference of the absolute values also confirm that there is an effect which decreases from -7 mT to -3 mT. The differences of the B_y and |B| are too high to be insignificant, because $\int$ B dl $\approx$ 0.71 Tm for the field and an absolute difference of around 6 mT corresponds to a maximal momentum accuracy $\approx$ 1% which is too high for a required momentum resolution of 2%.

The field maps measured at the GSI end at z $\approx$ -1300 mm, so the xy-plane at z = -1266 mm (in the middle) is the closest one to MOMO for which also GSI results are available. Figure 5.4 shows the in situ measurement and figure 5.9 the measurement at the GSI of this plane for the x-, y- and z-components of the magnetic field and |B|. These field maps are smaller than the field maps at z = -1065 mm because the shielding of MOMO reduces the possible moving area of the Hall probe.
The total difference between the in situ and the GSI magnetic field maps is shown in figure 5.10. The difference of the x component shows structure in the plane z = -1266 mm. However, the difference extends from -1 mT to 1 mT so it can be disregarded as it is small to affect the momentum resolution. The same applies for the z component which shows differences between 0 and 2 mT. The y component and |B| differences around -4 mT are too high to be disregarded. The y-component has the highest difference in the (x, y) corner and lower differences in the (-x, -y) corner. |B| also has the largest differences close to the edges of the spectrometer acceptance. In y direction the difference decreases to -1 mT. In this area |B| is dominated by the z component which has a smaller difference than the y component.
The ratios between the two field maps are shown in figure 5.11. The x-component shows also the shift

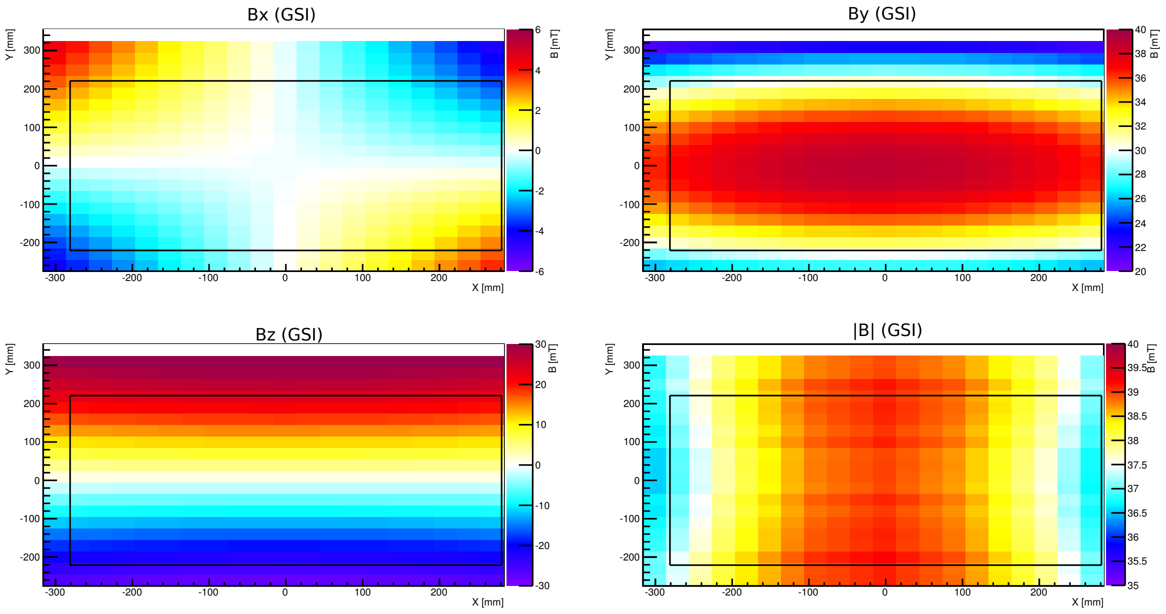

Figure 5.9: Magnetic field maps of the xy-plane at z = -1266 mm for the x-, y- and z-components and |B| measured at the GSI . Arranged in the same order as figure 5.3. The colour code shows the field intensity in mT. The black box marks the acceptance area for charged particles. The measurements are done with a magnetic field of 430 mT.

in the positioning between the in situ and GSI measured field in the -x and -y direction. The shift in the -y direction is also shown in magnetic field map of the z-component. The field map of the y-component shows a ratio of 90% which decreases to 80% in the y direction with a focus in the (y, x) corner. The ratio and the differences in |B| are largest in the centre of the acceptance decreasing towards the edges.

One reason for the shift can be the error in the position for the in situ measurement. Figure 5.12 shows the ratio of the in situ and GSI measured field maps at z = -1266 mm with a 2 cm shift in the x direction. The x component shows that the shift reduces the difference, however there must be more systematic effects contributing to this difference.

MOMO and its shielding with its asymmetric orientation has a definite effect which is partly responsible for the differences between the in situ measurement and the GSI. Also the BGO-ball and the iron holder structure is partly responsible for the shift in -y direction, shown in B_z the ratio. A rack for the electronics of SciFi2 may also have an effect on the field and may be partly responsible for the higher difference in the y direction of |B|. In the (x, y) corner of the acceptance area the MOMO shielding is closer than in the (-x, y) corner, which may be a reason for the higher differences in the (x, y) corner.

5.2 Comparison with the simulated data

The simulated magnetic field maps have the shielding of MOMO and SciFi2 and all magnetic parts of the detector setup included. The simulation used a current I = 1340 A that is the corresponding current for the 430 mT of the magnetic field at the reference Hall probe at the GSI. The current for the in situ measurement was $\approx$ 35 A lower (the exact current was not possible to read from the power supply of the Open Dipole).

Figure 5.13 shows the four simulated field maps of the xy-plane at z = -1065 mm (close to SciFi2)

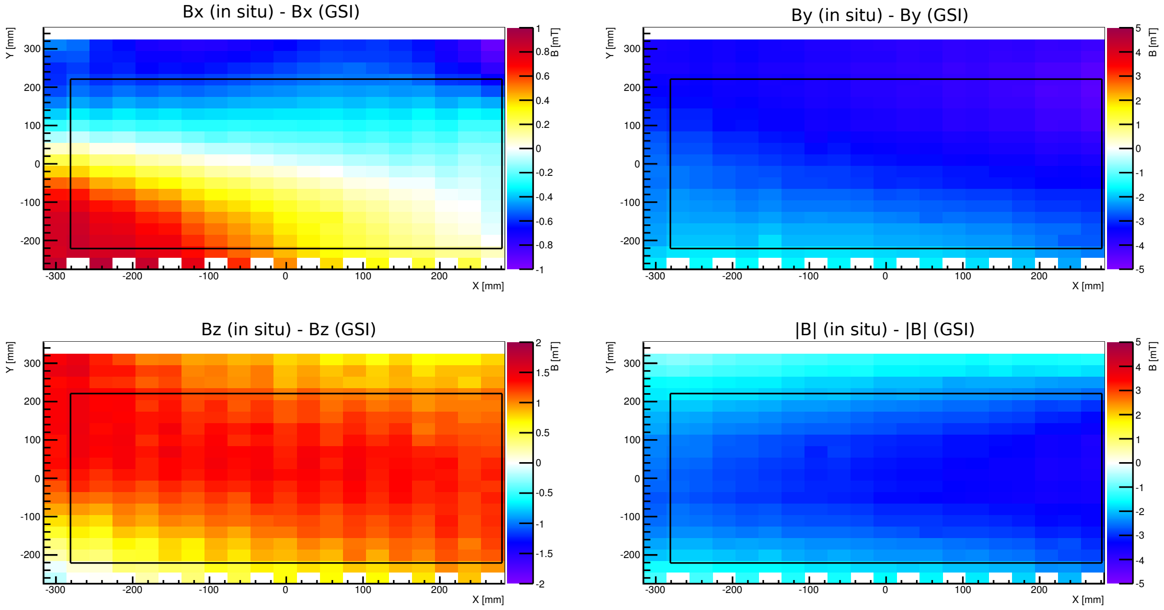

Figure 5.10: Difference between the in situ measured and at the GSI measured magnetic field maps of the xy-plane at z = -1266 mm for the x-, y- and z-components and |B|. Arranged in the same order as figure 5.3. The colour code shows the total difference of the measured values in mT. The black box marks the acceptance area for charged particles. The measurements are done with a magnetic field of 430 mT.

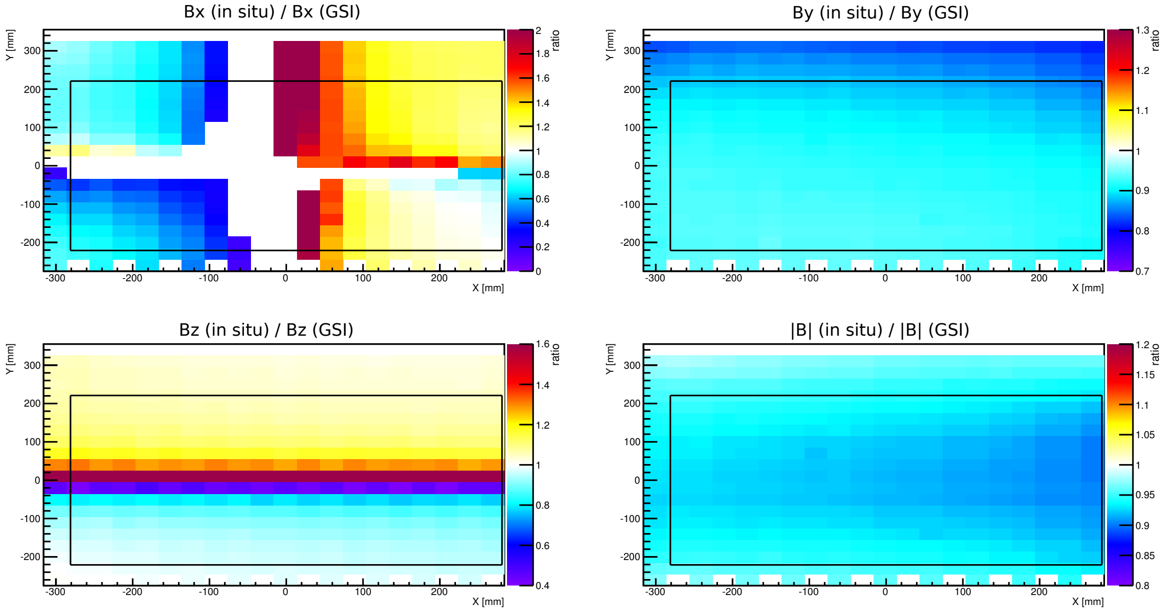

Figure 5.11: Ratio of the in situ measured and at GSI measured magnetic field maps of the xy-plane at z = -1266 mm for the x-, y- and z-components and |B|. Arranged in the same order as figure 5.3. The colour code shows the ratio. The black box marks the acceptance area for charged particles. The measurements are done with a magnetic field of 430 mT.

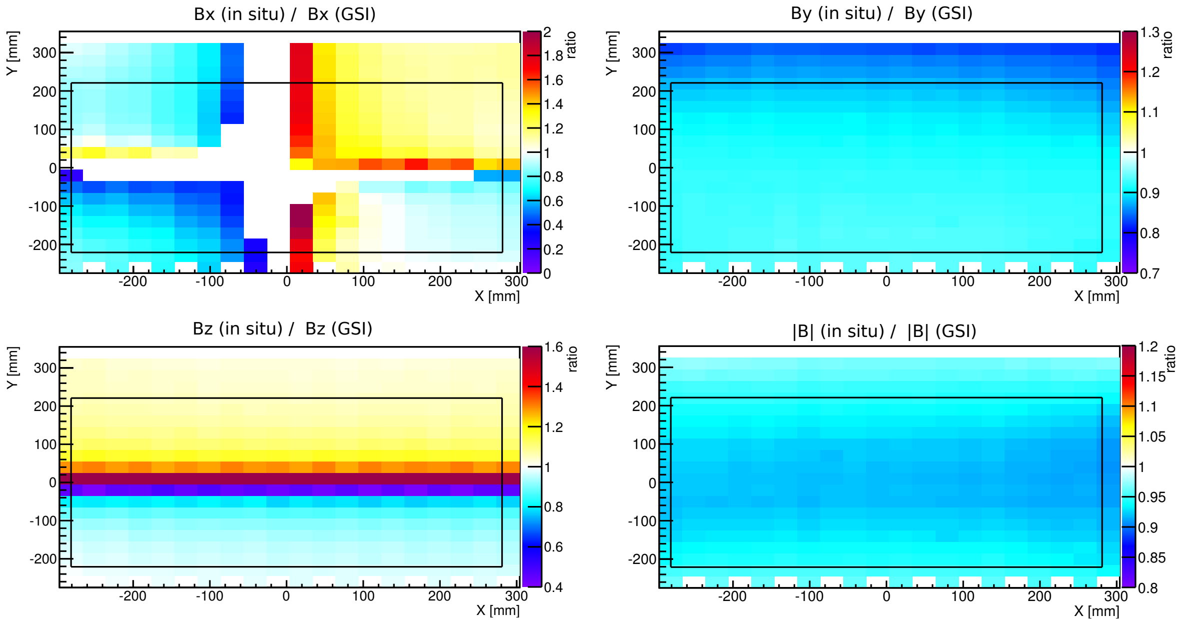

Figure 5.12: Ratio of the in situ measured and at GSI measured magnetic field maps of the xy-plane at z = -1266 mm for the x-, y- and z-components and |B| with a 2 cm shift in the x direction. Arranged in the same order as figure 5.3. The colour code shows the ratio. The black box marks the acceptance area for charged particles. The measurements are done with a magnetic field of 430 mT.

for the x-, y- and z-components and |B| of the field. The corresponding in situ measured field maps are shown in figure 5.3.

The related values for the absolute difference between measured and simulated field are shown in figure 5.14. Figure 5.15 shows ratios between the in situ measurements and simulated x-, y- and z-components and |B| of the magnetic field.

The differences of the x-component show a shift to the (-x, +y) direction. The difference field map of B_z in the bottom left shows a small shift in the y coordinate. In the (+x, +y) corner the difference decreases to values over -15 mT could be a fragment of the simulation. For the active area the simulated field is around 5 mT higher than the measured field. The differences of the y component of the magnetic fields fluctuate in active area between 1 mT and 4 mT at field strengths between 45 mT and 65 mT.
The ratio of the z component shows that the line where the measured data switches from positive to negative values is not exactly aligned with the simulated data. That is different to the GSI field in which the line lays over the measured data. Otherwise shows the map that the simulated field are up to 20% higher then the measured data. The field map of the x component of the magnetic field shows a shift in the -x direction together with a smaller shift to +y direction between the measured and the simulated field.
The ratio of the y component shows that the measured field values are $\approx$ 10% lower than the values of the simulated field. This changes only at the border of the measured field where the shielding of SciFi2 is located. The ratio of |B| verifies that the measured field is in total 10% less than the simulated field. Only the border at the shielding has a total offset in the (x, y) corner higher than in the (-x, y) corner. One reason for the lower measured field strength could be, that the simulation used a current of 1340 A and for the measurements the current was a little bit lower, causing the total field strength to be higher

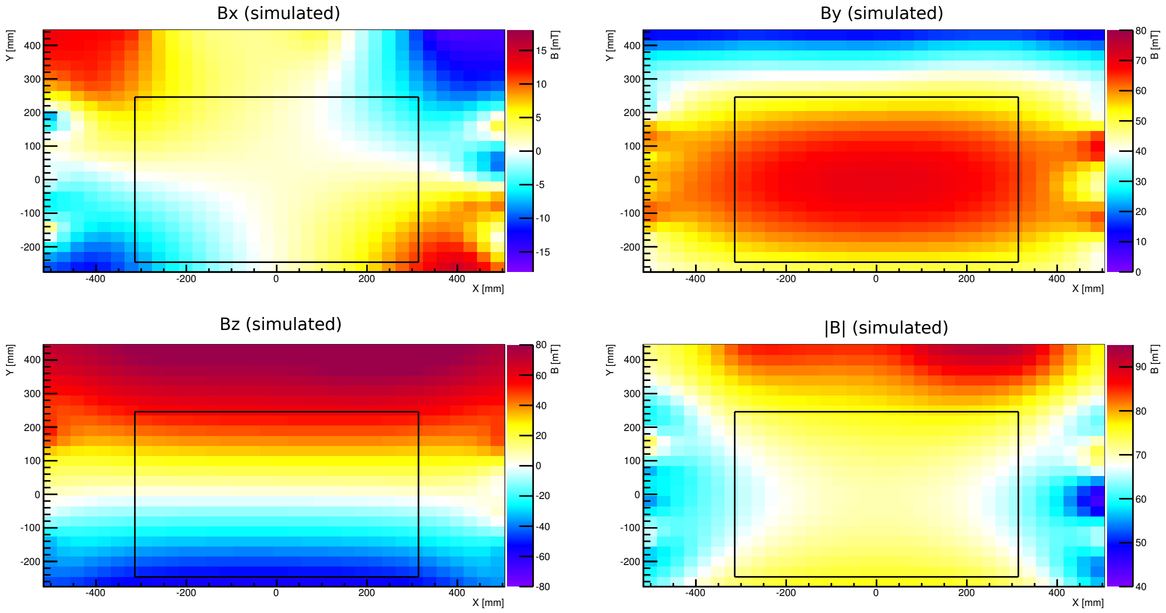

Figure 5.13: Simulated magnetic field maps of the xy-plane at z = -1065 mm for the x-, y- and z-components of the magnetic field and |B|. Arranged in the same order as figure 5.3. The colour code shows the field intensity in mT. The black box marks the acceptance area for charged particles. The simulation are done for I = 1340 A.

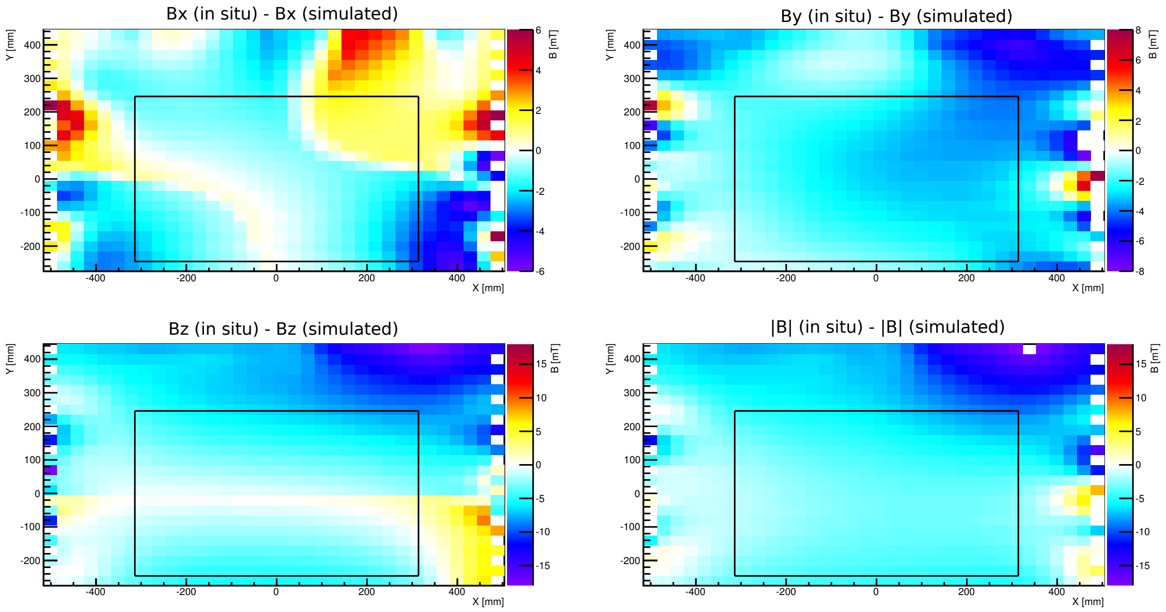

Figure 5.14: Difference between the in situ measured and the simulated magnetic field maps of the xy-plane at z = -1065 mm for the x-, y- and z-components and |B|. Arranged in the same order as figure 5.3. The colour code shows the of the measured values in mT. The black box marks the acceptance area for charged particles. The measurements are done with a magnetic field of 430 mT and simulation are done for a current of 1340 A.

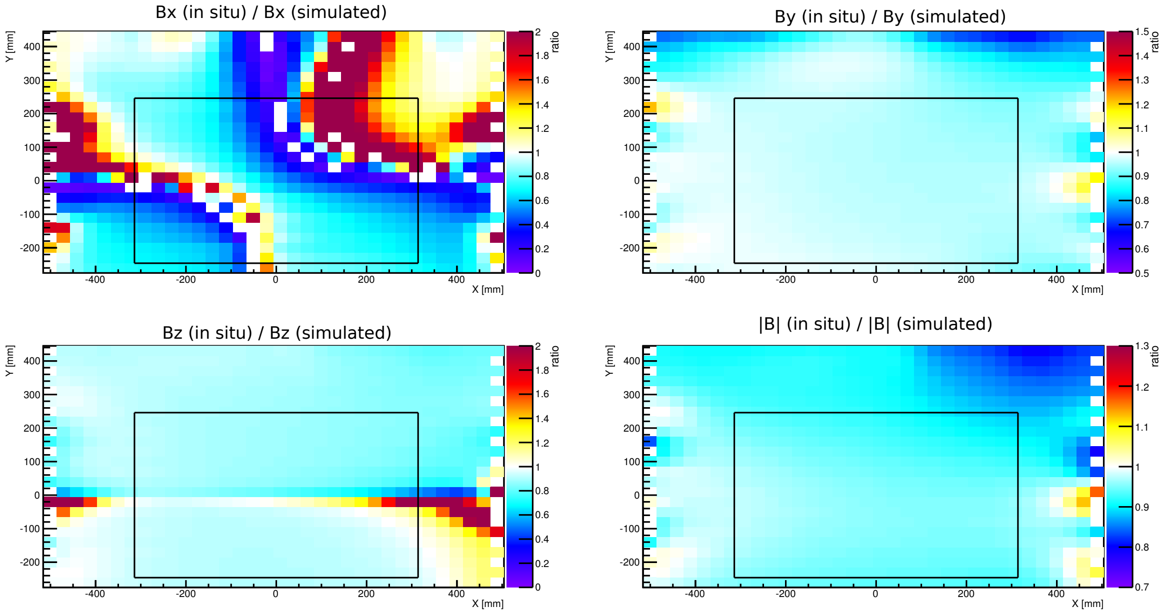

Figure 5.15: Ratio of the in situ measured and simulated magnetic field maps of the xy-plane at z = -1065 mm for the x-, y- and z-component and |B|. Arranged in the same order as figure 5.3. The colour code shows the ratio. The black box marks the acceptance area for charged particles. The measurements are done with a magnetic field of 430 mT and simulation are done for a current of 1340 A.

at the simulated field.

The other z position of the comparison between the GSI and the in situ measured magnetic field is at z = -1266 mm, figure 5.16 shows the four field maps at that position, B_x, B_y, B_z and |B| of simulated data. B_x (top right in the figure 5.16) has more positive field values than the measured field (figure 5.4) and the values of B_y of the simulated field are smaller than the in situ measured field.

The ratio (figure 5.17) and the total difference of the x-component (figure 5.18) shows a shift to the (-x, y) direction and the simulated x-component has values up to 3 mT greater than the in situ measurement.

The ratio of the z component shows again the shift in y direction. In the region over the shift the ratio has a value of 80% and under the shift a value of 90%. The total difference shows also the shift in y direction and from there a more or less symmetric negative rise of the total difference to the top and the bottom. The reason why the difference in the positive region is higher depends on the shift and the factor that in this direction the field was measured up to a higher position.

The ratio and total difference for the y component confirm that the measured values are higher than the simulated values. The ratio gives a value from less than 10% difference for the mean part of the measured field only in (-x, -y) corner and in the area of x = 100 to -200 and y over 240 the ratio increase to around 20%. In this area the total difference increase to 4 mT - 5 mT. In the rest of the map the difference is less then 4 mT at field strengths between 15 mT and 35 mT. Depending of the effect that in the middle of the acceptance the y-component is the main component of |B| and at the borders of the magnetic field the y component gets smaller and the z components increase, the ratio of |B| goes from 1.1 to 0.9 and smaller at the top border of the ratio map with a the shift in (y, -x) direction. The total

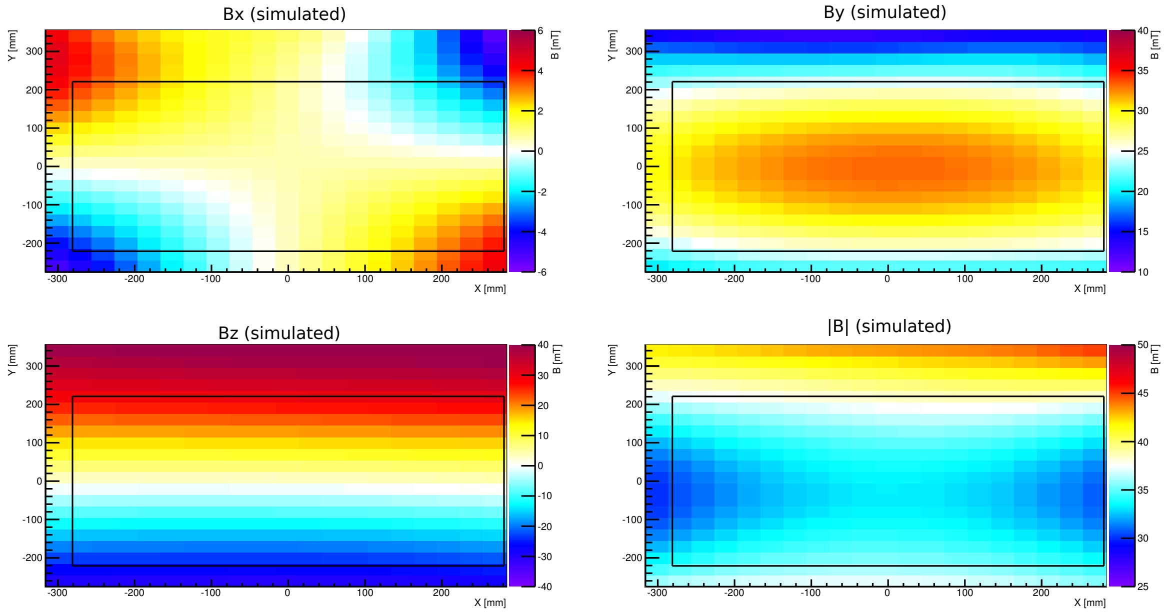

Figure 5.16: Simulated magnetic field maps of the xy-plane at z = -1266 mm for the x-, y- and z-component and |B|. Arranged in the same order as figure 5.3. The colour code shows the field intensity in mT. The black box marks the acceptance area for charged particles. The simulation are done for a current of 1340 A.

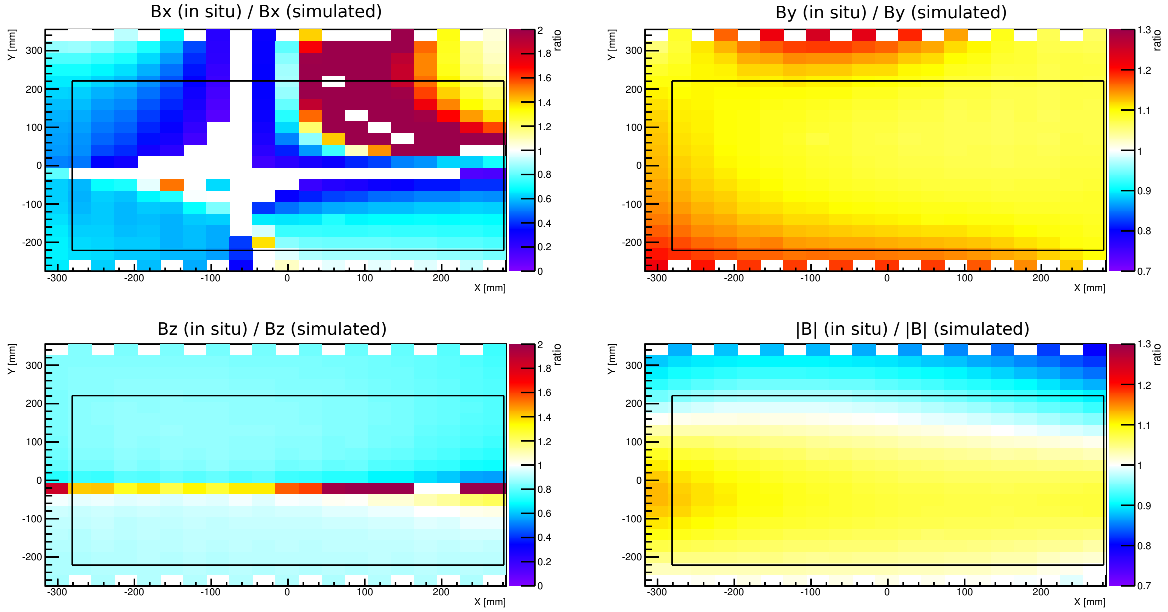

Figure 5.17: Ratio of the in situ measured and simulated magnetic field maps of the xy-plane at z = -1266 mm for the x-, y- and z-components and |B|. Arranged in the same order as figure 5.3. The colour code shows the ratio. The black box marks the acceptance area for charged particles. The measurements are done with a magnetic field of 430 mT and simulation are done for a current of 1340 A.

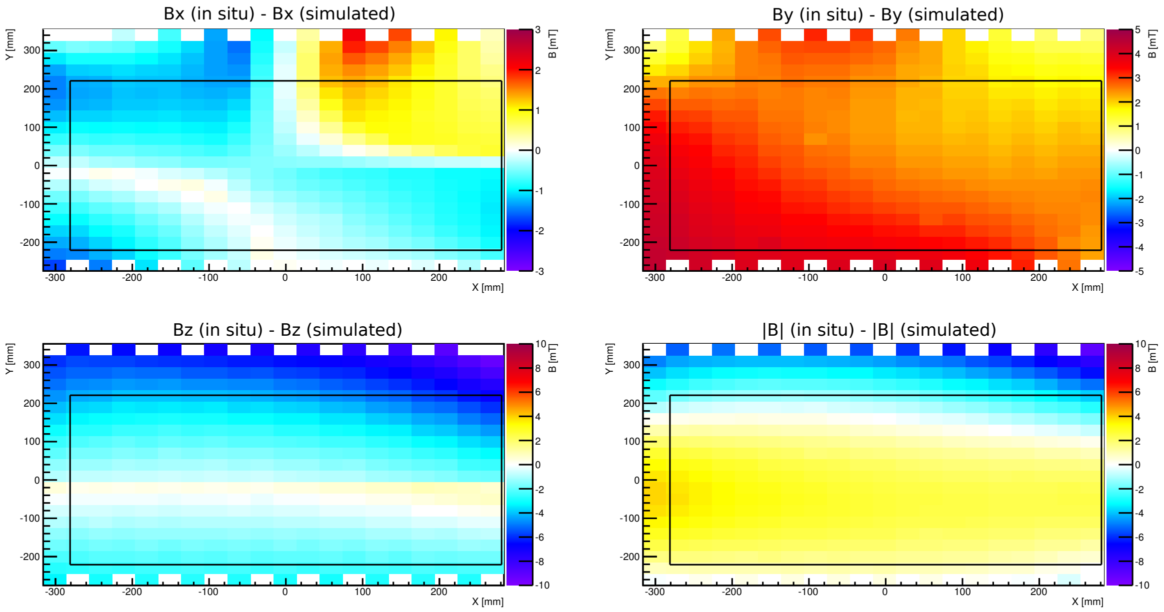

Figure 5.18: Difference between the in situ measured and the simulated magnetic field maps of the xy-plane at z = -1266 mm for the x-, y- and z-components and |B|. Arranged in the same order as figure 5.3. The colour code shows the of the measured values in mT. The black box marks the acceptance area for charged particles. The measurements are done with a magnetic field of 430 mT and simulation are done for a current of 1340 A.

difference changes from 3 mT to -4 mT and in the right top corner decrease to 9 mT at field strengths from 30 mT to 45 mT.

In figure 5.5 is shown a xy-plane at z = -1452 mm (close to MOMO) where there is no GSI field map. Figure 5.19 shows the simulated field maps for this z position. The total difference between the in situ measurements and simulated field are shown in figure 5.20 and the corresponding ratio between them is shown in figure 5.21.

The field maps also show the shift in (y, -x) direction which comes partly from the error of the positioning of the in situ measured field. The y-component of the magnetic field and |B| shows a strong difference at the (x, y) corner and in the middle over the acceptance area. At these positions are the shielding of the MOMO photomultiplier tubes and the Hall probe measured as close as possible to them there. Considering the error of the positioning in the y and z direction, the simulated field could be closer to the iron of the shielding.

The measured field of the y component is 5 mT to 7 mT higher when the simulated field, that is 40% and more by a simulated field values of maximal 15 mT of the y-component. The simulation of the Open Dipole simulates the field not for an endless volume, but for a box around the Open Dipole. It is probably that the given field strength at the border in the -z direction is smaller than the real one. That would explain why the in situ measured B_y has higher values than the simulated one with a larger distance to the magnet. The non expected small asymmetric shift in the ratio and difference can be explained by fragments in the simulation.

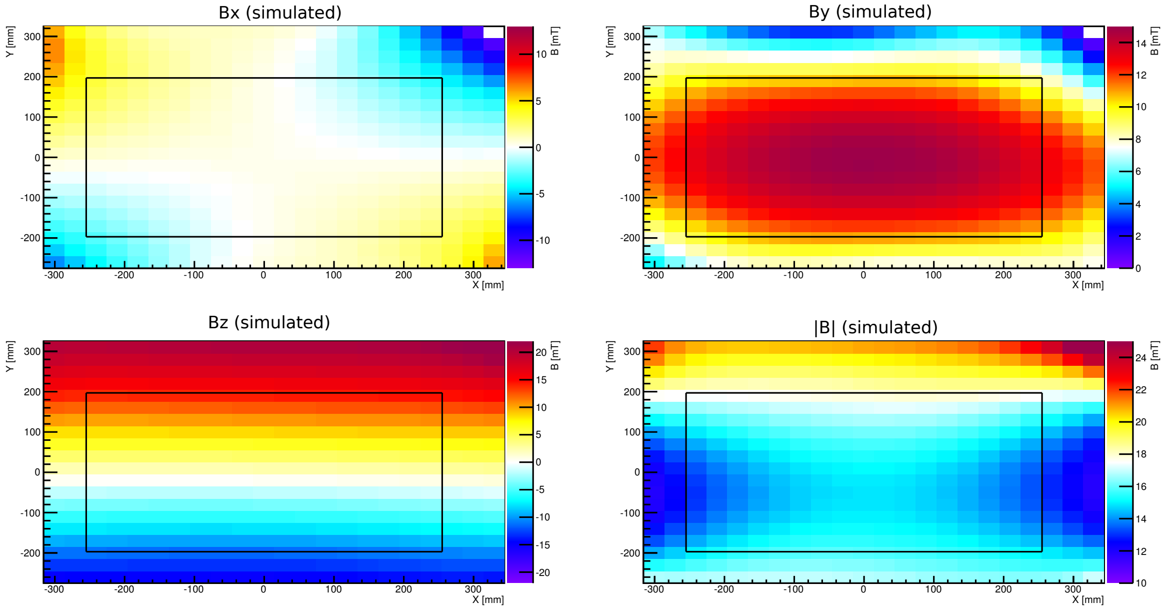

Figure 5.19: Simulate magnetic field maps of the xy-plane at z = -1452 mm (close to MOMO) for the x-, y- and z-component and |B|. Arranged in the same order as figure 5.3. The colour code shows the field intensity in mT. The black box marks the acceptance area for charged particles.The measurements are done with a magnetic field of 430 mT and simulation are done for a current of 1340 A.

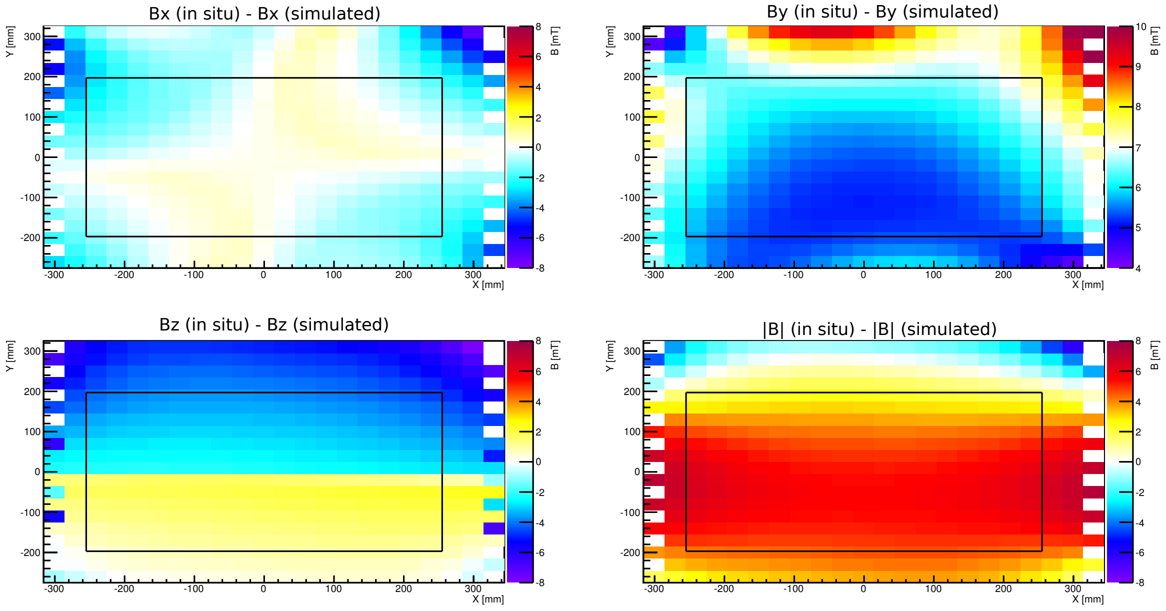

Figure 5.20: Difference between the in situ measured and the simulated magnetic field maps of the xy-plane at z = -1452 mm (close to MOMO) for the x-, y- and z-components and |B|. Arranged in the same order as figure 5.3. The colour code shows the of the measured values in mT. The black box marks the acceptance area for charged particles. The measurements are done with a magnetic field of 430 mT and simulation are done for a current of 1340 A.

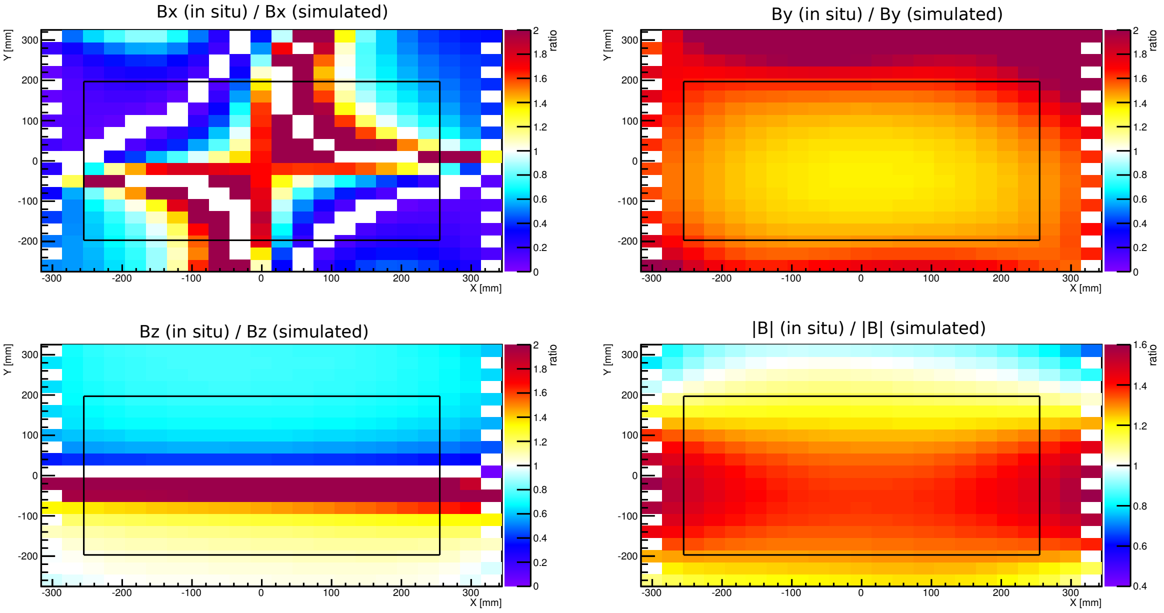

Figure 5.21: Ratio of the in situ measured and simulated magnetic field maps of the xy-plane at z = -1452 mm for the x-, y- and z-components and |B|. Arranged in the same order as figure 5.3. The colour code shows the ratio. The black box marks the acceptance area for charged particles. The measurements are done with a magnetic field of 430 mT and simulation are done for a current of 1340 A.

5.3 Analysis of momentum reconstruction using simulated data

For precise momentum reconstruction the in situ measured values are included in the simulation. To determine what effect the in situ field maps have upon the momentum reconstruction, the in situ measured field maps are included in the simulation. Simulated protons were generated at the target with an energy of E_{kin} = 1 GeV at a set angle of $\Phi = 90°$ and $\Theta = 5°$. The protons traversed the Open Dipole field and were detected 672 cm behind the target with a $200 \times 200 \times 1.5\,\mathrm{cm}^3$ plastic wall. Figure 5.22 shows the different positions where the protons hit the plastic wall for the simulated field and the simulated field with the in situ measurement included.

Gaussian functions were fitted to both data sets showing that there is only a small different in the hit position. The mean of the simulated field with measured data included are -53.09 ± 0.11 cm with a σ = 2.154 ± 0.097 cm and for the simulated field only -53.34 ± 0.13 cm with a σ = 2.415 ± 0.010 cm. The two values are in the 1-σ region of each other.

The next step was to replace the simulated field by the measured field at the GSI. Then two different magnetic field settings were created. The first used the the measured field at GSI and the simulated field in front of the magnet between the target and the end of the measurement at the GSI. The second one used the in situ measured field and the measured field at GSI and the simulated field in front of the magnet between the target and the end of the in situ measurement in the target direction. Figure 5.23 shows a drawing of the region (in front of the magnet) where the two magnetic field settings are different.

It was found that the measured field strength at the magnet centre was a factor of 0.97 different to the simulated field, consequently the simulated field was scaled by 0.97. For both magnetic field settings 300000 protons starting at the target are simulated with an energy from E_{kin} = 100 MeV to

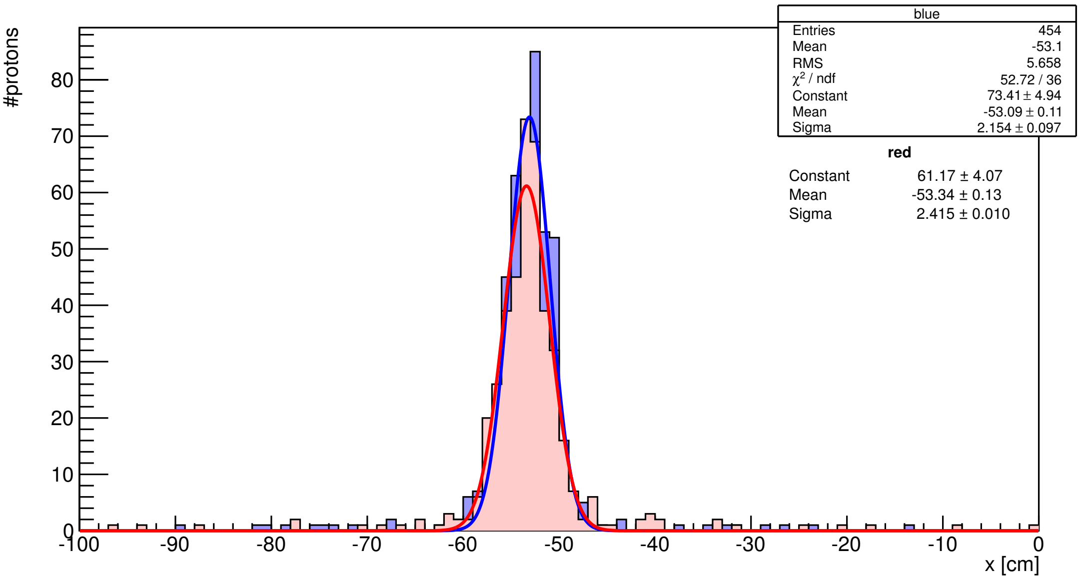

Figure 5.22: Simulated protons created at the target with an energy of $E_{kin} = 1\,\mathrm{GeV}$ and the angle $\Phi = 90°$ and $\Theta = 5°$ which traversed the Open Dipole magnetic field and were detected 672 cm behind the target at $(200 \times 200 \times 1.5)\,\mathrm{cm}^3$ plastic wall. Blue shows the x position the protons penetrated the wall for the protons with the in situ measured field included in the simulated field and red with only the simulated field. Inset are Gaussion fit parameters.

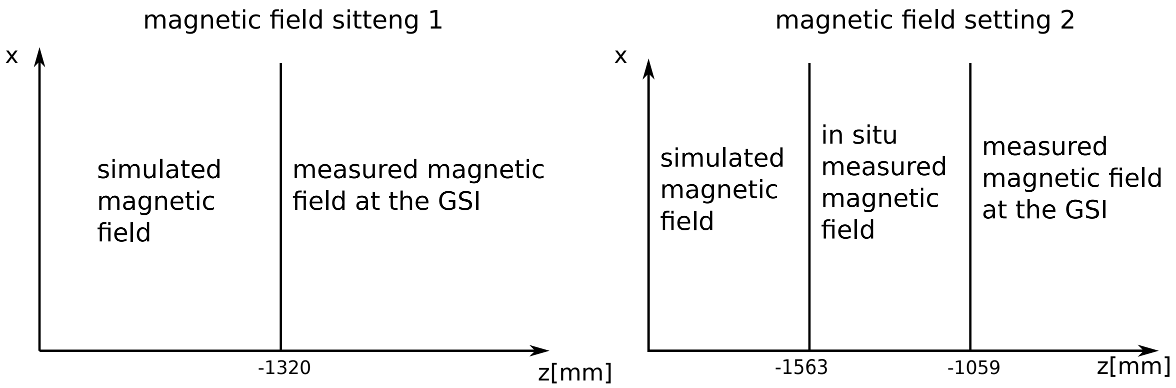

Figure 5.23: Drawing of the two different magnetic field settings.

E_{kin} = 2200 MeV and angles Φ_{min} = 0° to Φ_{max} = 360° and from Θ_{min} = 0° to Θ_{max} = 12°. This covers the full magnetic region expected for the detection of protons in the forward spectrometer.

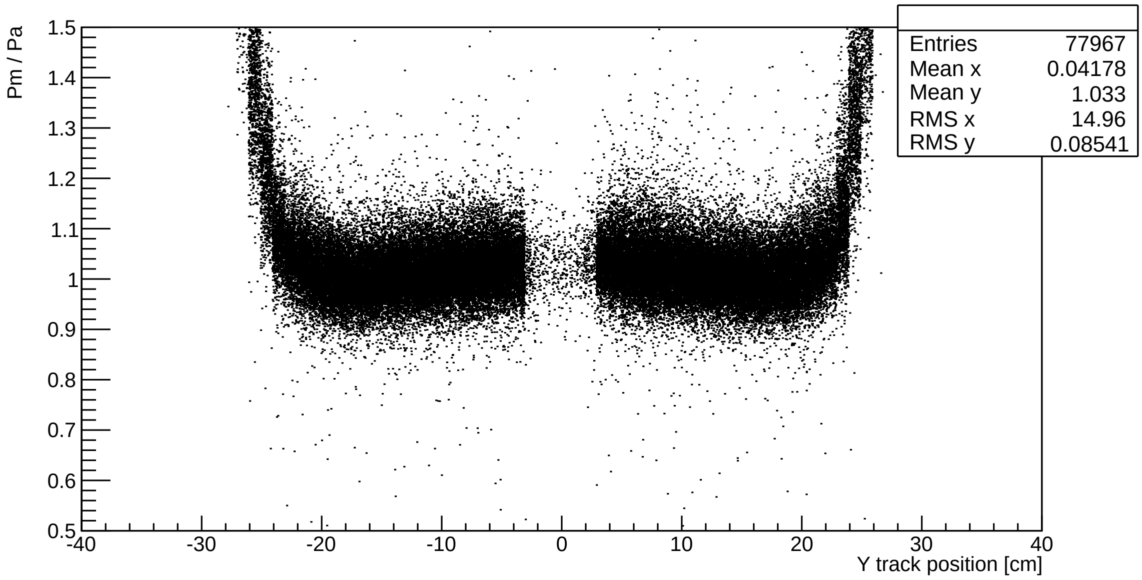

Figure 5.24: Ratio of the measured (Pm) to the actual momentum (Pa) of the y position of simulated protons starting at the target with an energy from E_{kin} = 100 MeV to E_{kin} = 2200 MeV, angles from Φ_{min} = 0° to Φ_{max} = 360° and from Θ_{min} = 0° to Θ_{max} = 12°.

Figure 5.24 shows the ratio of the measured (Pm) to the actual momentum (Pa) plotted against the y position of the track with the first magnetic field setting. It shows that at the limits of acceptance in y, Pm / Pa increases to beyond 1.5. It is speculated that this may be due to the mapped magnetic field not covering the volume inside the magnet and close to the magnet's yokes. For the following comparison to make sure that the all protons hit the whole field, tracks >|22| cm of the y position are rejected. A correction was applied to align Pm / Pa to 1 for all remaining values of x and y. Figure 5.25 shows Pm / Pa plotted against the y position of the track with the cut and correction included. This correction with the same values was also performed for the second setting with the in situ measured field included.

Figure 5.26 shows momentum of simulated protons and ratio of the measured to the actual momentum, Pm / Pa when using the simulated field and the GSI measured field. The corresponding plot for the same simulated protons with the GSI and in situ measured magnetic field are shown in figure 5.27.

For more detailed information of the different of the measured momentum difference using the two magnetic field maps settings, a projection of Pm / Pa was performed for momentum of 1 GeV and 2.5 GeV.

For 1 GeV momentum a Gaussian fit of Pm / Pa for the setting with the GSI measured magnetic field gives a value for Pm / Pa = 0.986 ± 0.001 with σ = 0.02746 ± 0.00042 shown in figure 5.28. Figure 5.29 shows the corresponding plot for the setting with the GSI and in situ measured magnetic field and

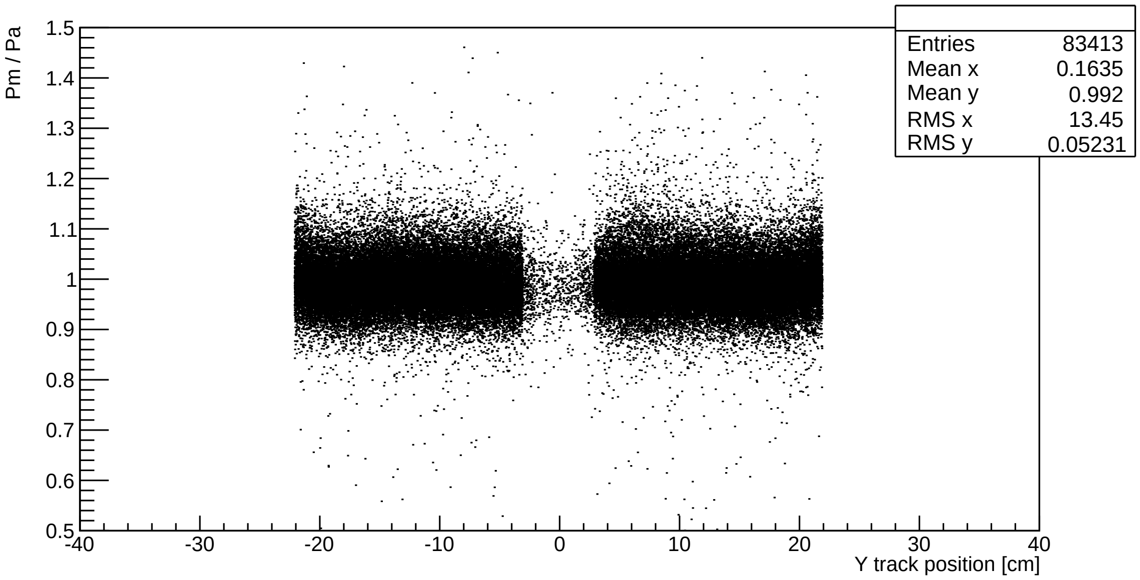

Figure 5.25: Ratio of the measured (Pm) to the actual momentum (Pa) of the y position of simulated protons starting at the target with an energy from E_{kin} = 100 MeV to E_{kin} = 2200 MeV from Φ_{min} = 0° to Φ_{max} = 360° and from Θ_{min} = 0° to Θ_{max} = 12°. Track >|22| cm are cut out and a small correction of the positioning of ΔP are done.

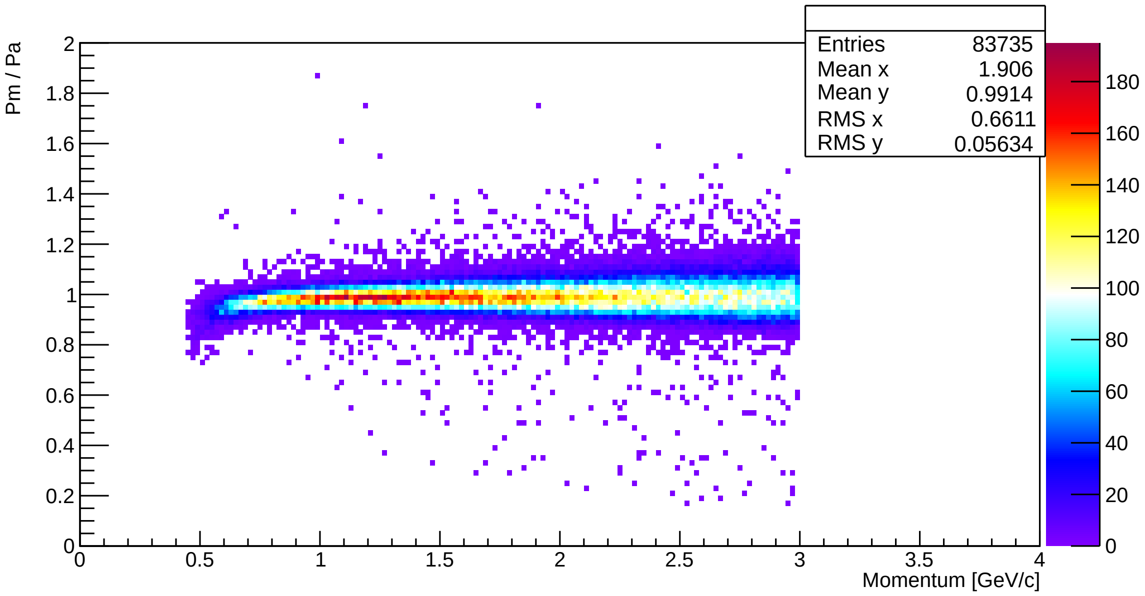

Figure 5.26: Ratio of the measured (Pm) to the actual momentum (Pa) of simulated protons traversing the magnetic field measured at the GSI. The colour shows the number of protons.

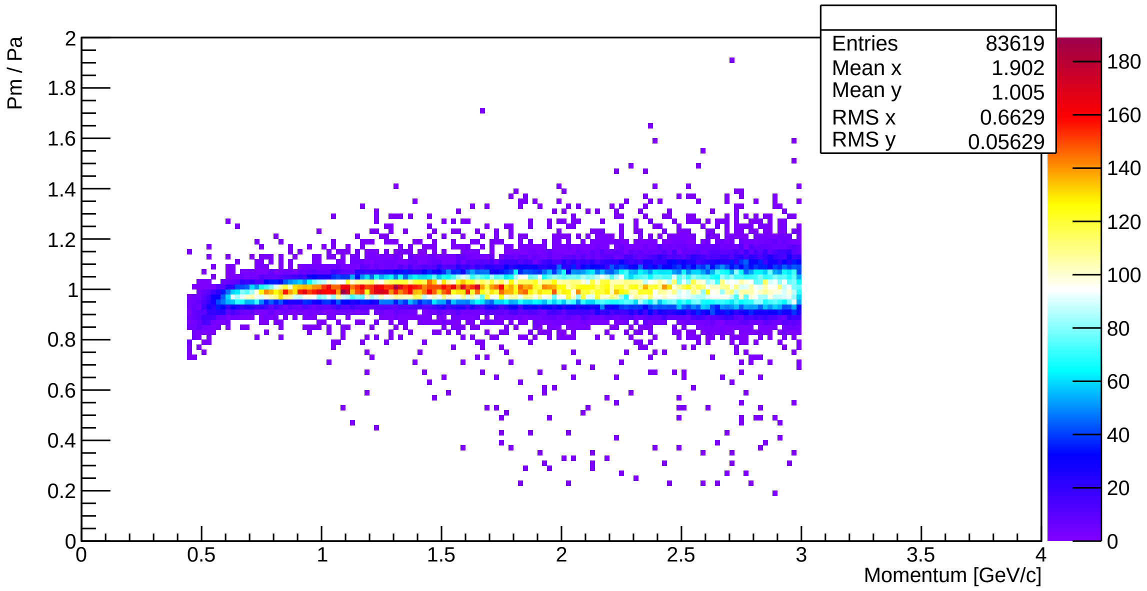

Figure 5.27: Ratio of the measured (Pm) to the actual momentum (Pa) of simulated protons traversing the magnetic field measured at the GSI and the in situ. The colour shows the number of protons.

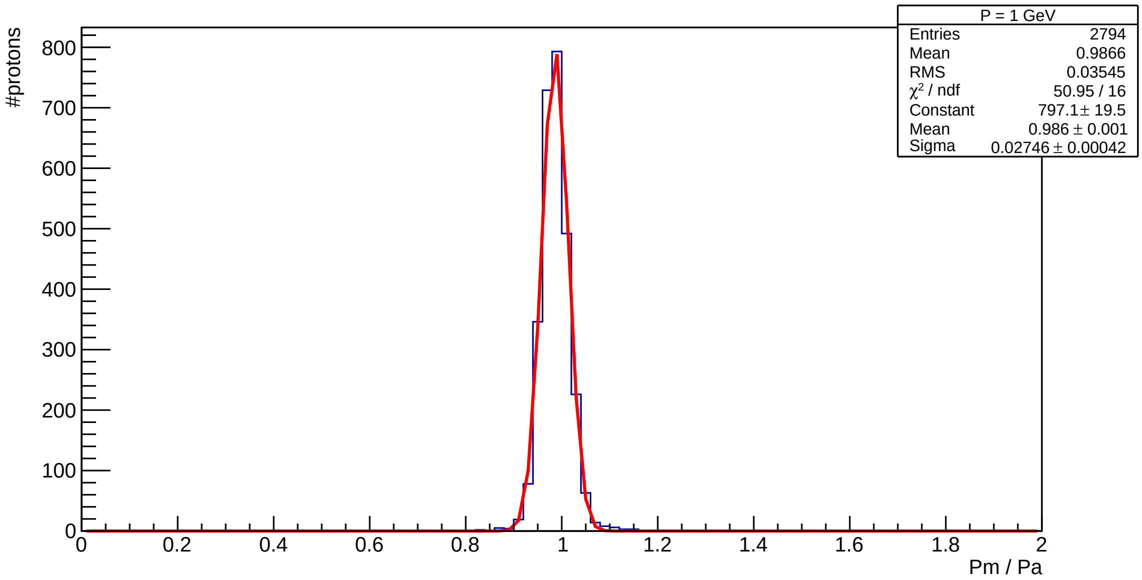

Figure 5.28: Ratio of the measured (Pm) to the actual momentum (Pa) for 1 GeV of momentum with the magnetic field measured at the GSI.

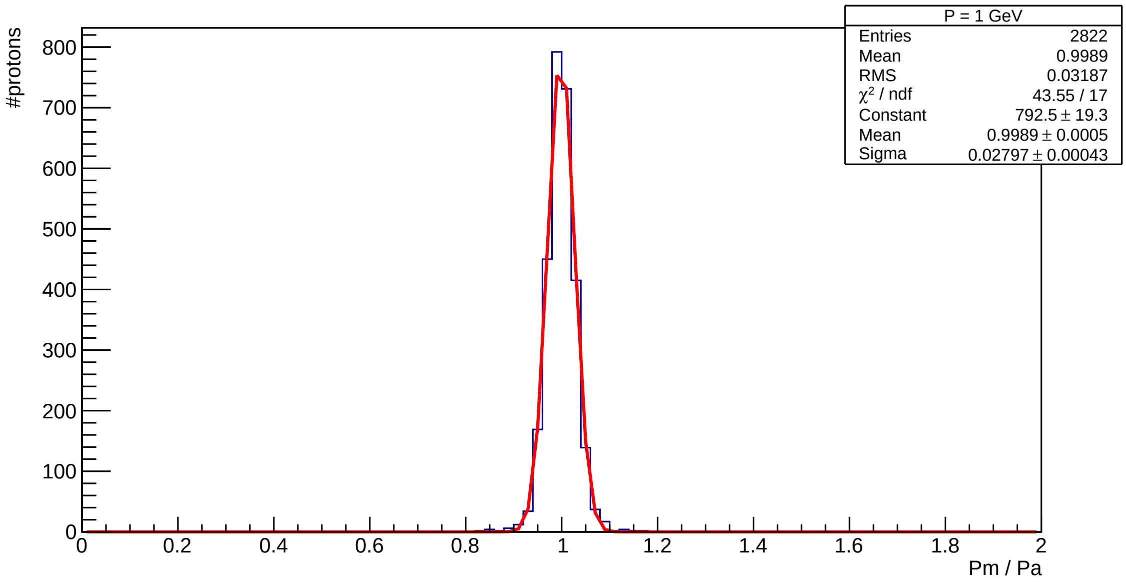

Figure 5.29: Ratio of the measured (Pm) to the actual momentum (Pa) for 1 GeV of momentum with the magnetic field measured at the GSI and in situ.

gives a value of Pm / Pa = 0.9989 ± 0.00043 with $\sigma = 0.02797 \pm 0.00043$.

Figure 5.30 shows ratio of the measured to the actual momentum for a momentum of 2.5 GeV with the GSI measured magnetic field. A fitted Gaussian function gives the value for Pm / Pa = 0.9968 ± 0.0010 with $\sigma = 0.05634 \pm 0.00068$. The corresponding plot for the GSI and in situ measured magnetic field is shown in figure 5.31 and gives values of Pm / Pa = 1.01 with $\sigma = 0.05549 \pm 0.00068$ for the Gaussian function fitted. Within fitting error and expected accuracy, the measured momentum using both field maps agree and also reproduced the actual, true particle momentum.

To get extract the momentum accuracy between the two magnetic field settings the momentum of protons traversing the magnetic field are plotted against the ratio between the measured momentum using the GSI measured magnetic field (setting 1) and the GSI measured field with the in situ measured magnetic field included (setting 2) shown in figure 5.32. It shows a mean of 0.9913 over the whole energy region. In appendix B are shown projections of Pm / Pa for different momenta (1.2 GeV, 1.5 GeV, 2 GeV, 2.5 GeV and 3 GeV). The mean of fitted Gaussian functions vary between 0.9842 with $\sigma = 0.047$ (P = 2 GeV) and 0.9987 with $\sigma = 0.06647$ (P = 3 GeV).
The mean of 0.9914 is achieved for the whole polar angle of acceptance Θ, shown in figure 5.33. In the appendix B are shown projection of Pm / Pa for for different Θ (4°, 5°, 6°, 7°, 8° and 10°). The mean of the fitted Gaussian functions vary between 0.9891 with $\sigma = 0.04068$ ($\Theta = 4°$) and 0.9942 with $\sigma = 0.004302$ ($\Theta = 6°$). All Gaussian fits shows show that there is a momentum accuracy $\approx 1\%$.
Figure 5.34 shows the total difference between the Θ angle of the measured proton momenta in the GSI measured magnetic field and the magnetic field measured at the GSI and in situ. Θ is given by the hits of a particle in MOMO and Scifi2 assuming there is no deflection from a magnetic field. The fact that $\Delta\Theta \approx 0°$ demonstrates that the fringe field does not effect the particle trajectories between SciFi and

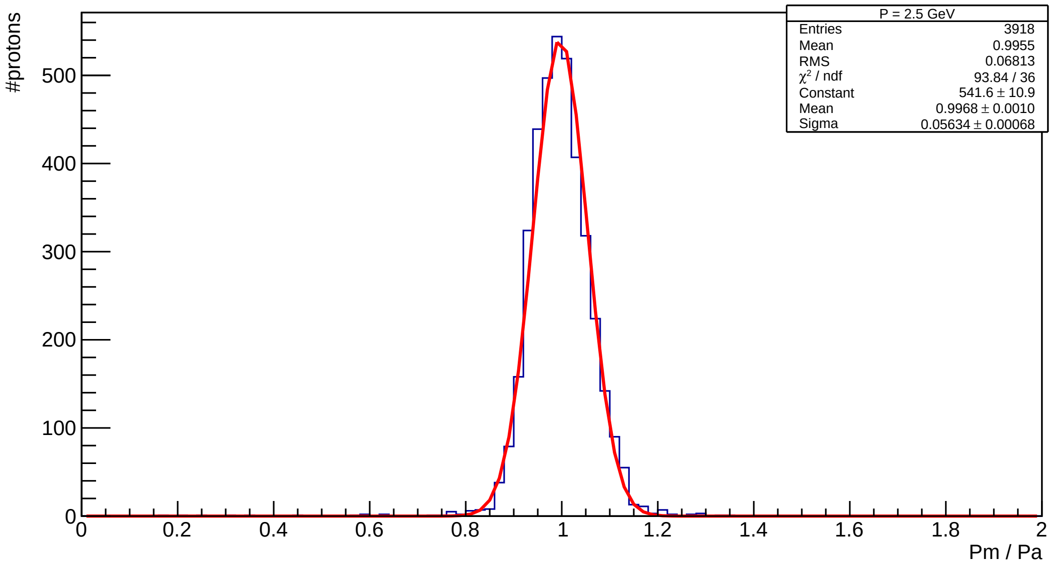

Figure 5.30: Ratio of the measured (Pm) to the actual momentum (Pa) for 2.5 GeV of momentum with the magnetic field measured at the GSI.

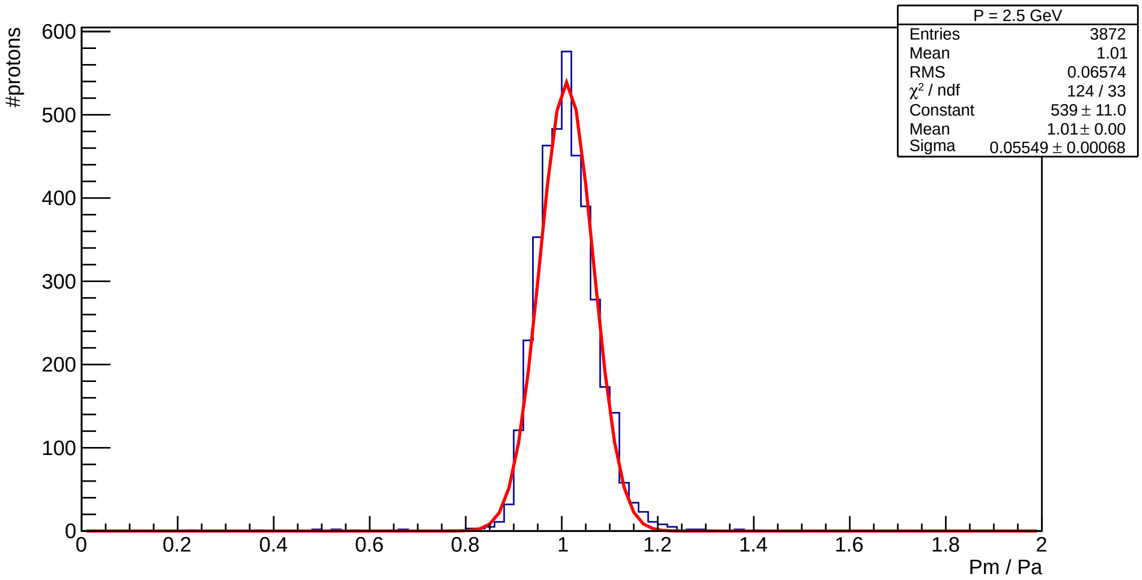

Figure 5.31: Ratio of the measured (Pm) to the actual momentum (Pa) for 2.5 GeV of momentum with the magnetic field measured at the GSI and in situ.

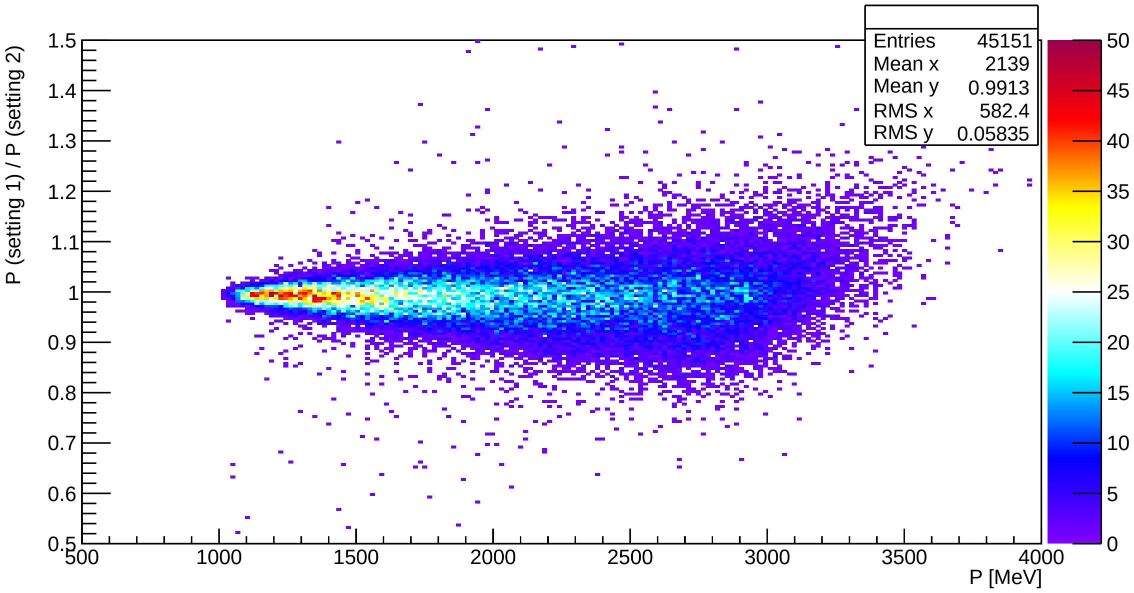

Figure 5.32: Momentum of simulated protons traversing the magnet field measured at GSI plotted again the momentum accuracy between the momentum of a protons that traversing the magnetic field measured at GSI (setting 1) and the the magnetic field measured at GSI with in situ measured field included (setting 2). The colour code shows the number of protons.

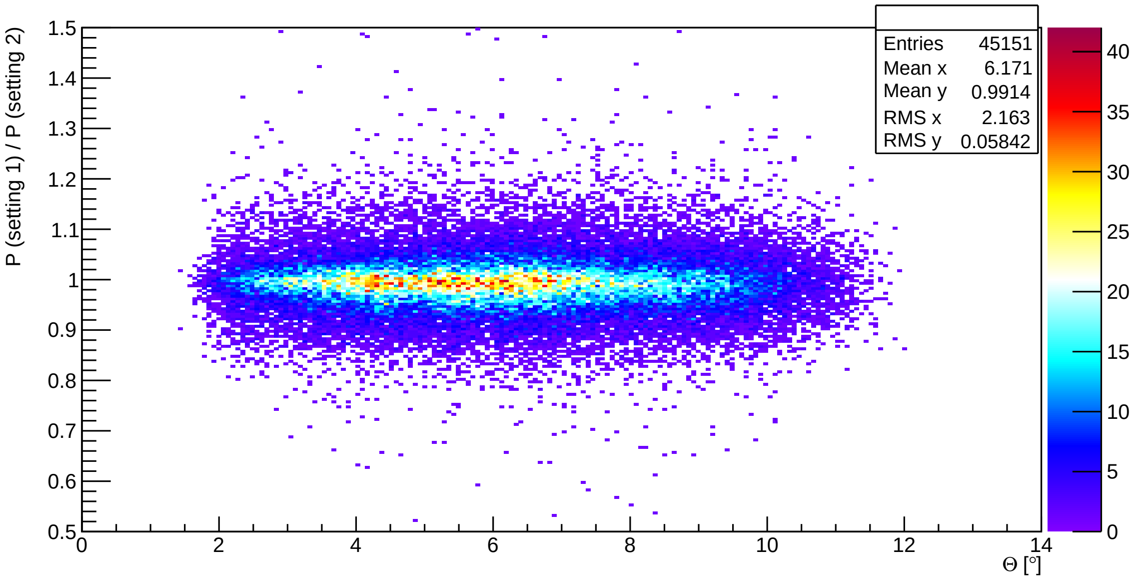

Figure 5.33: Θ angle of the simulated protons traversing the magnet field measured at GSI plotted again the momentum accuracy between the momentum of a protons that traversing the magnetic field measured at GSI (setting 1) and the the magnetic field measured at GSI with in situ measured field included (setting 2). The colour code shows the number of protons.

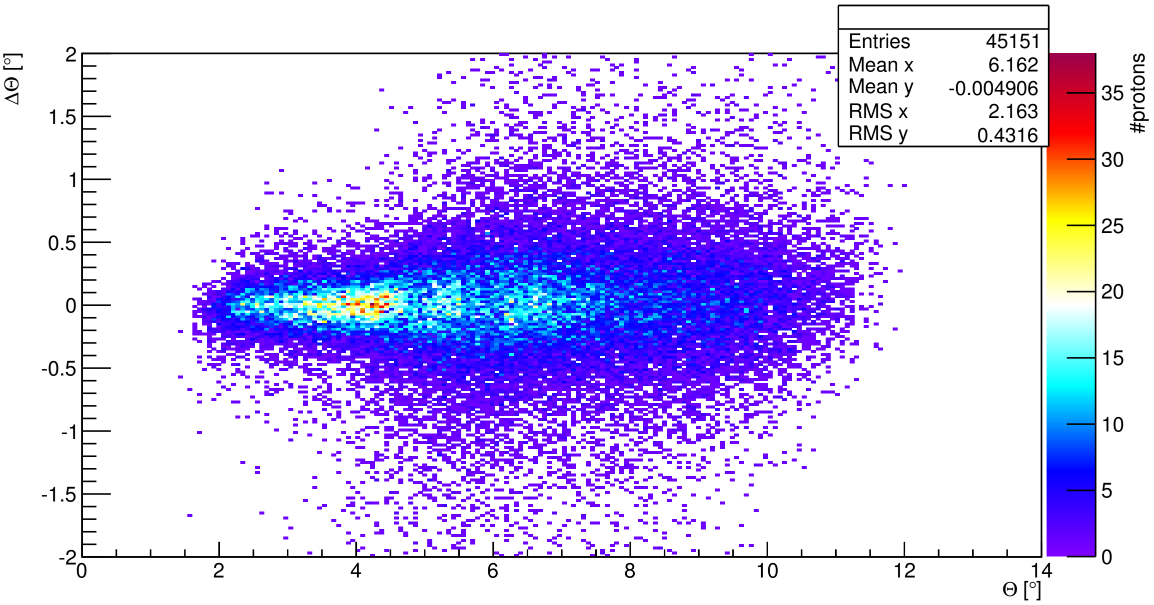

Figure 5.34: Θ angle of the simulated protons traversing the magnet field measured at GSI plotted again the total difference of the Θ angle between protons traversing the magnetic field measured at GSI and the the magnetic field measured at GSi with in situ measurements included. The colour code shows the number of protons.

MOMO.

The analysis of momentum reconstruction using simulated data shows that it gives a momentum accuracy of up to $\approx 1\%$, it vary depending on the momentum and the angles.

Chapter 6

Summary and Outlook

The aim of my of diploma work was to develop and construct an in situ field mapping system for the fringe field in front of the Open Dipole magnet of the BGO-OD experiment. A first measurement with this construction was also completed. Both are described in this thesis.

The in situ field mapping system was based on a two axis linear system which moved a Hall probe in the vertical and the horizontal directions by two independent step motors. It could be moved by hand in the beam direction (z direction) on the MOMO holding structure rails. The Hall probe can measure all three components of the magnetic field at the same time. For each step motor an independent electronic control board was developed and built. A program with a user interface was been written for the movement of the Hall probe by the step motors, allowing an automatic measurement of an xy-plane of the magnetic field.

The magnetic field in the area between MOMO and Scifi2 was measured and compared with the measurements at the GSI and the simulated field.
The comparison with the GSI measurement shows that the new shielding of the photomultiplier tubes and the metallic structures of the detectors close to the open dipole magnet have a non-negligible effect. It is estimated that this effect changes the measured particle momenta by $\approx 1\%$, which is 50% of the required momentum resolution of 2%.
A comparison with the simulated field shows that there is no significant differences between the in situ measured data and the simulated data. Close to the edges of the measured field region however, the y-component of the magnetic field is smaller in the simulated field than the measured field.
Also shifts in the x and y direction are shown between the in situ simulated data and the GSI data, which is due to the positioning error of the in situ measurement due to the small uncertainly in the reference position measurement.
To reduce this error a laser tracker system will soon be used, providing an accuracy of 1-2 mm.

The analysis of the momentum reconstruction using simulated data verified the estimated momentum accuracy of $\approx 1\%$ for protons traversing the magnetic field measured. This was found to be the case for when only using the GSI measured field and when also including the new in situ measurement.

Appendix A

In situ measurement

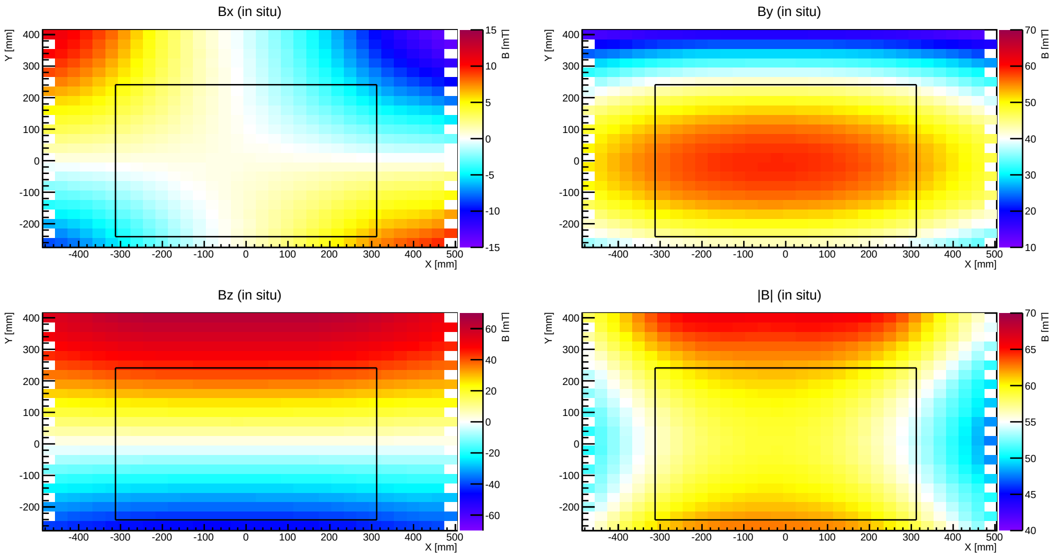

Figure A.1: Magnetic field maps of the xy-plane at z = -1108 mm for the x-, y- and z-components and |B| measured in situ. Arranged in the same order as figure 5.3. The colour code shows the field intensity in mT. The black box marks the acceptance area for charged particles. The measurements are done with a magnetic field of 430 mT.

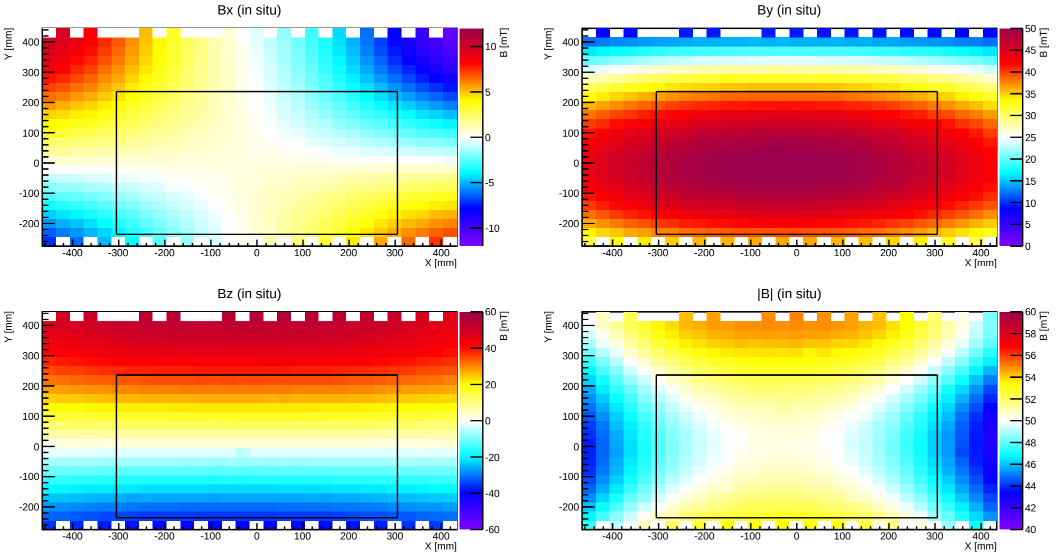

Figure A.2: Magnetic field maps of the xy-plane at z = -1149 mm for the x-, y- and z-components and |B| measured in situ. Arranged in the same order as figure 5.3. The colour code shows the field intensity in mT. The black box marks the acceptance area for charged particles. The measurements are done with a magnetic field of 430 mT.

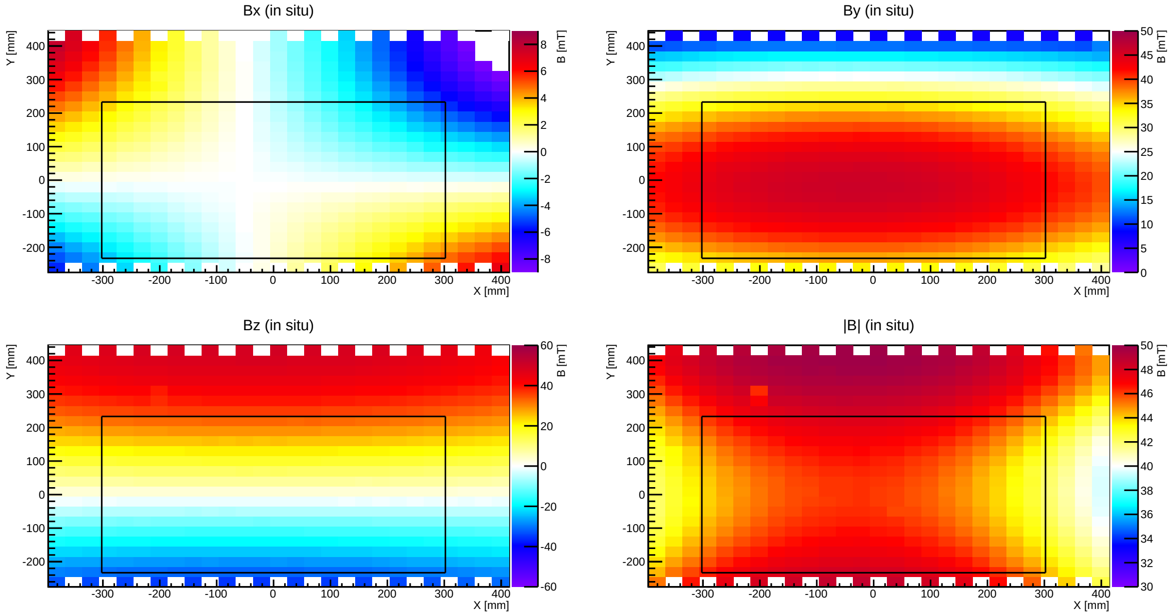

Figure A.3: Magnetic field maps of the xy-plane at z = -1178 mm for the x-, y- and z-components and |B| measured in situ. Arranged in the same order as figure 5.3. The colour code shows the field intensity in mT. The black box marks the acceptance area for charged particles. The measurements are done with a magnetic field of 430 mT.

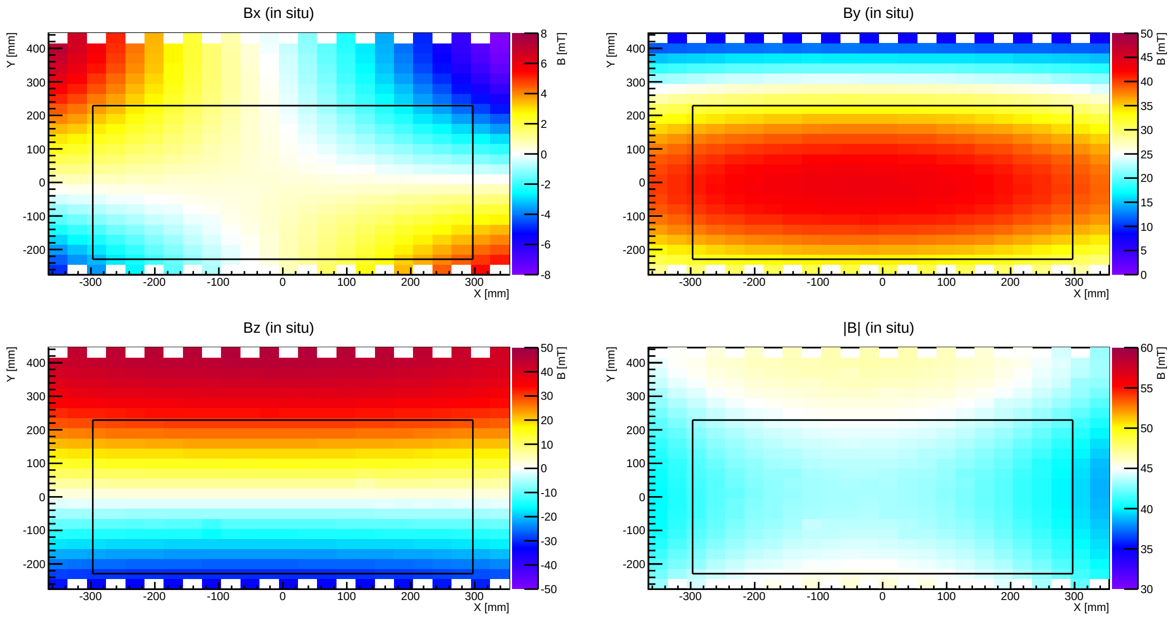

Figure A.4: Magnetic field maps of the xy-plane at z = -1201 mm for the x-, y- and z-components and |B| measured in situ. Arranged in the same order as figure 5.3. The colour code shows the field intensity in mT. The black box marks the acceptance area for charged particles. The measurements are done with a magnetic field of 430 mT.

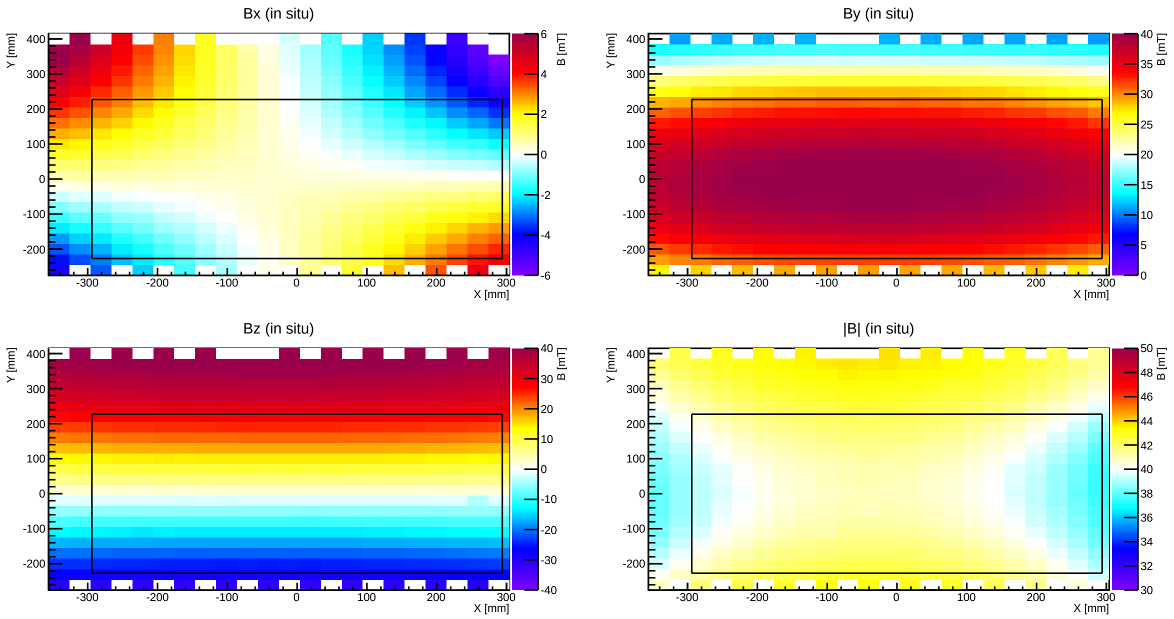

Figure A.5: Magnetic field maps of the xy-plane at z = -1219 mm for the x-, y- and z-components and |B| measured in situ. Arranged in the same order as figure 5.3. The colour code shows the field intensity in mT. The black box marks the acceptance area for charged particles. The measurements are done with a magnetic field of 430 mT.

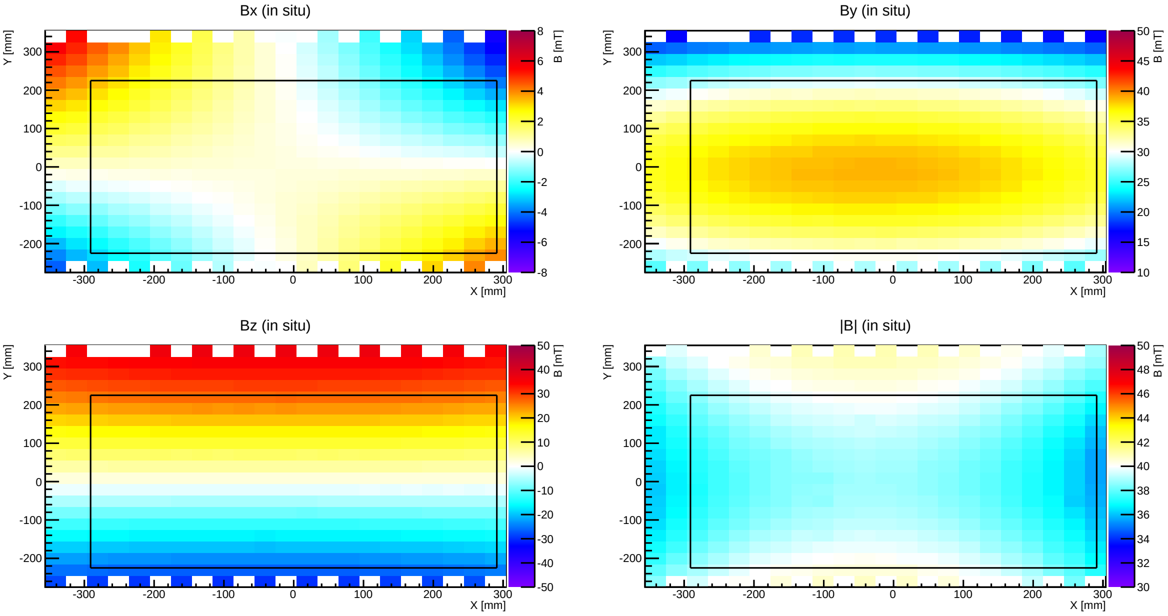

Figure A.6: Magnetic field maps of the xy-plane at z = -1232 mm for the x-, y- and z-components and |B| measured in situ. Arranged in the same order as figure 5.3. The colour code shows the field intensity in mT. The black box marks the acceptance area for charged particles. The measurements are done with a magnetic field of 430 mT.

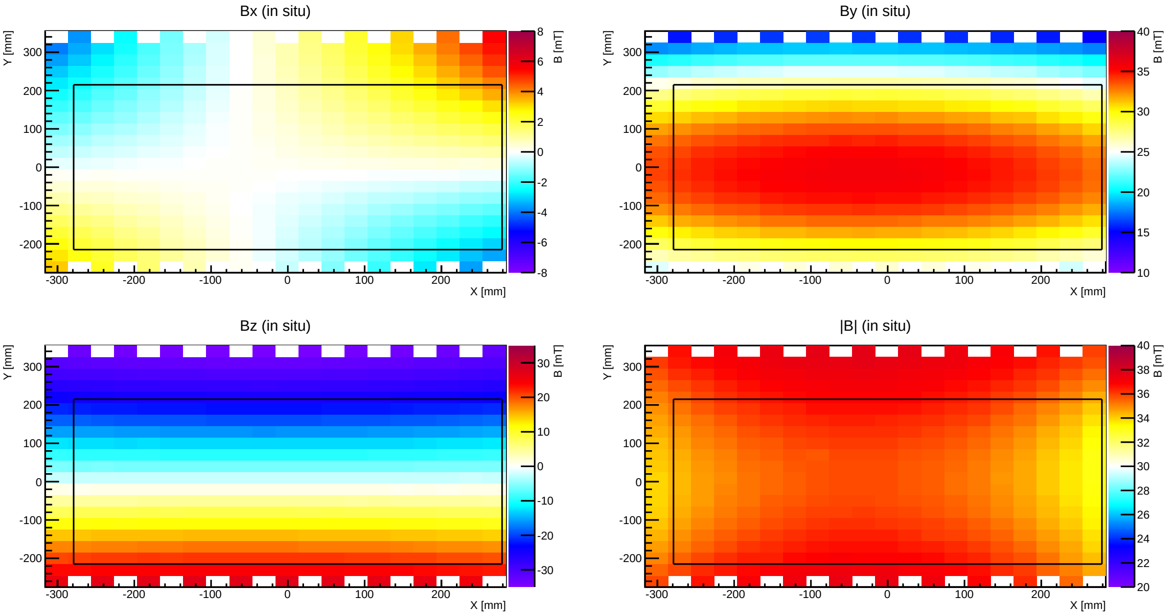

Figure A.7: Magnetic field maps of the xy-plane at z = -1308 mm for the x-, y- and z-components and |B| measured in situ. Arranged in the same order as figure 5.3. The colour code shows the field intensity in mT. The black box marks the acceptance area for charged particles. The measurements are done with a magnetic field of 430 mT.

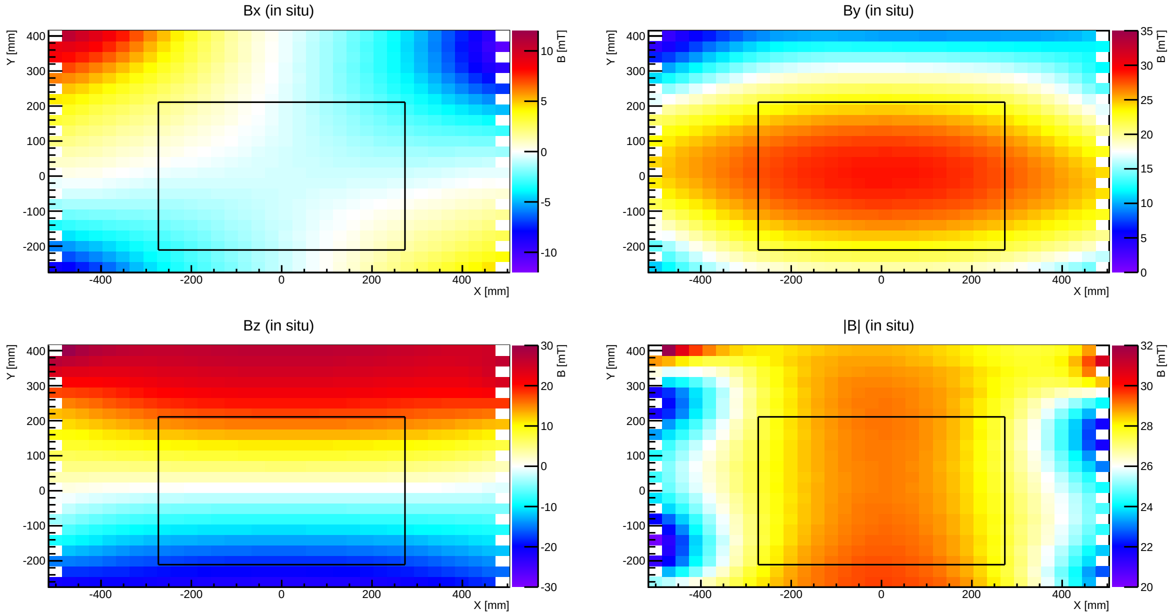

Figure A.8: Magnetic field maps of the xy-plane at z = -1343 mm for the x-, y- and z-components and |B| measured in situ. Arranged in the same order as figure 5.3. The colour code shows the field intensity in mT. The black box marks the acceptance area for charged particles. The measurements are done with a magnetic field of 430 mT.

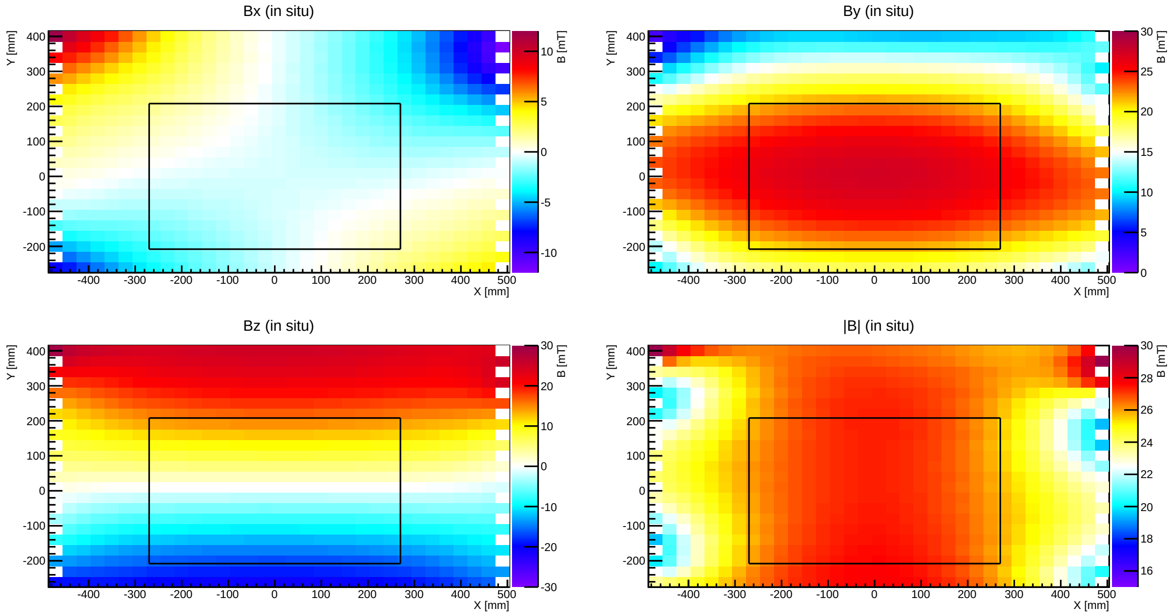

Figure A.9: Magnetic field maps of the xy-plane at z = -1362 mm for the x-, y- and z-components and |B| measured in situ. Arranged in the same order as figure 5.3. The colour code shows the field intensity in mT. The black box marks the acceptance area for charged particles. The measurements are done with a magnetic field of 430 mT.

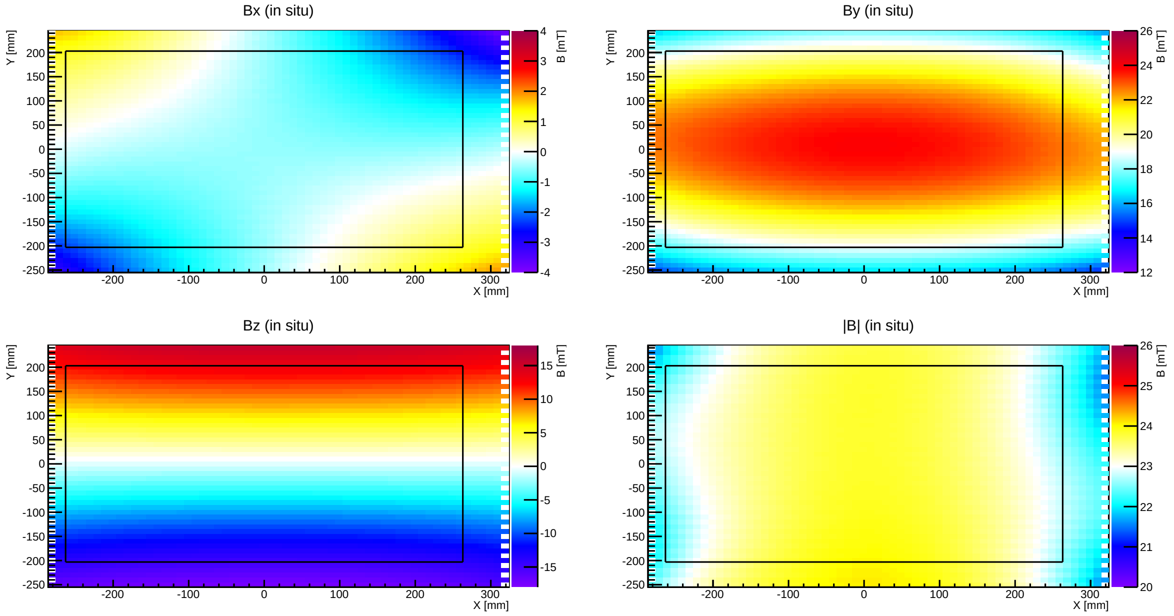

Figure A.10: Magnetic field maps of the xy-plane at z = -1402 mm for the x-, y- and z-components and |B| measured in situ. Arranged in the same order as figure 5.3. The colour code shows the field intensity in mT. The black box marks the acceptance area for charged particles. The measurements are done with a magnetic field of 430 mT.

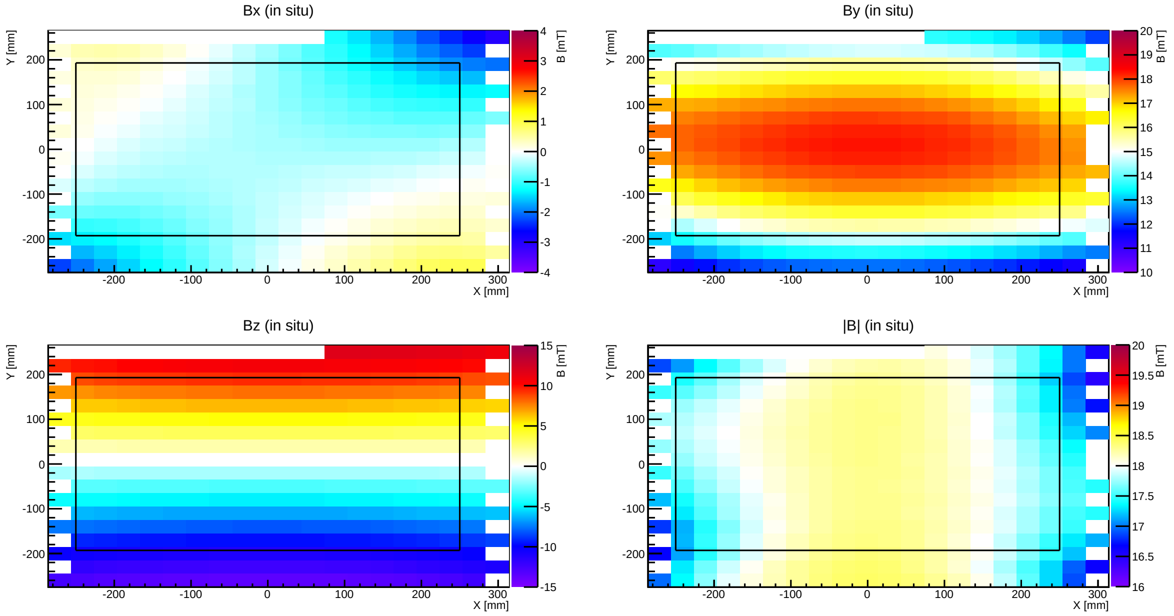

Figure A.11: Magnetic field maps of the xy-plane at z = -1484 mm for the x-, y- and z-components and |B| measured in situ. Arranged in the same order as figure 5.3. The colour code shows the field intensity in mT. The black box marks the acceptance area for charged particles. The measurements are done with a magnetic field of 430 mT.

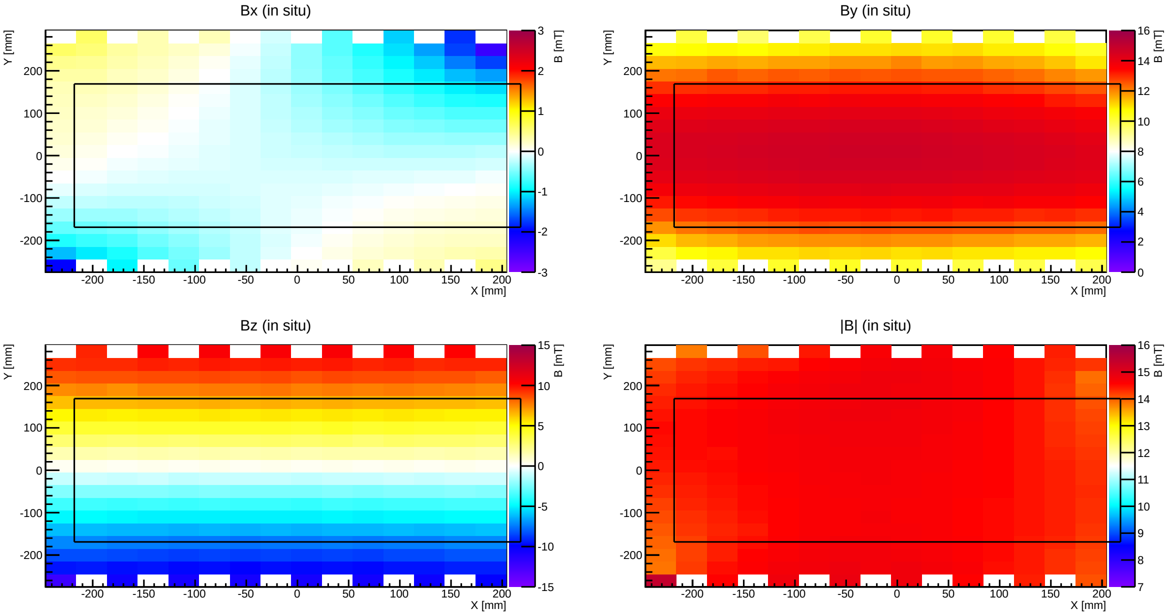

Figure A.12: Magnetic field maps of the xy-plane at z = -1554 mm for the x-, y- and z-components and |B| measured in situ. Arranged in the same order as figure 5.3. The colour code shows the field intensity in mT. The black box marks the acceptance area for charged particles. The measurements are done with a magnetic field of 430 mT.

Appendix B

Simulation

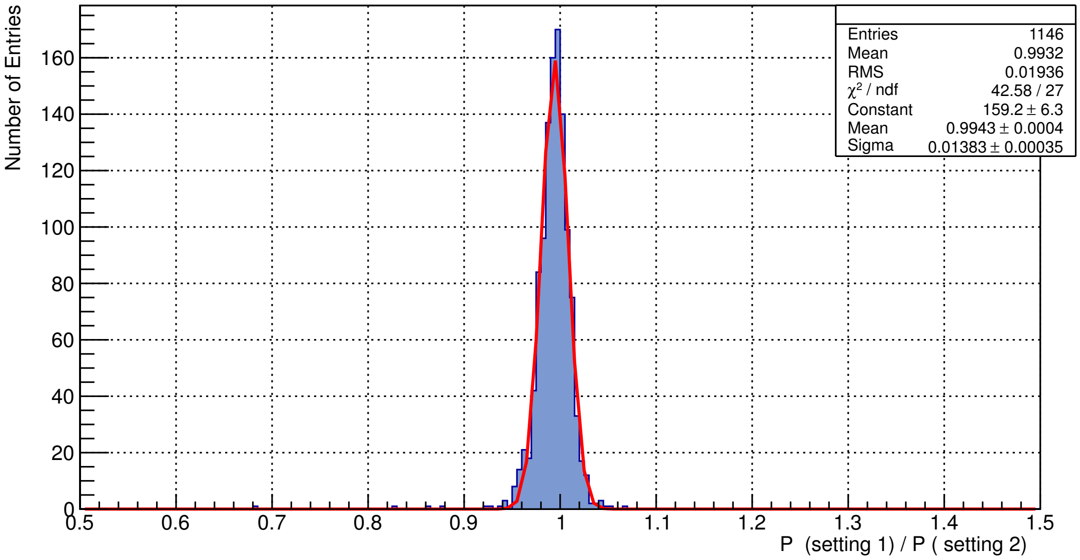

Figure B.1: P (setting 1) / P (setting 2) for protons with 1.2 GeV of momentum traversing the corresponding magnetic field settings. Inset are Gaussian fit parameters.

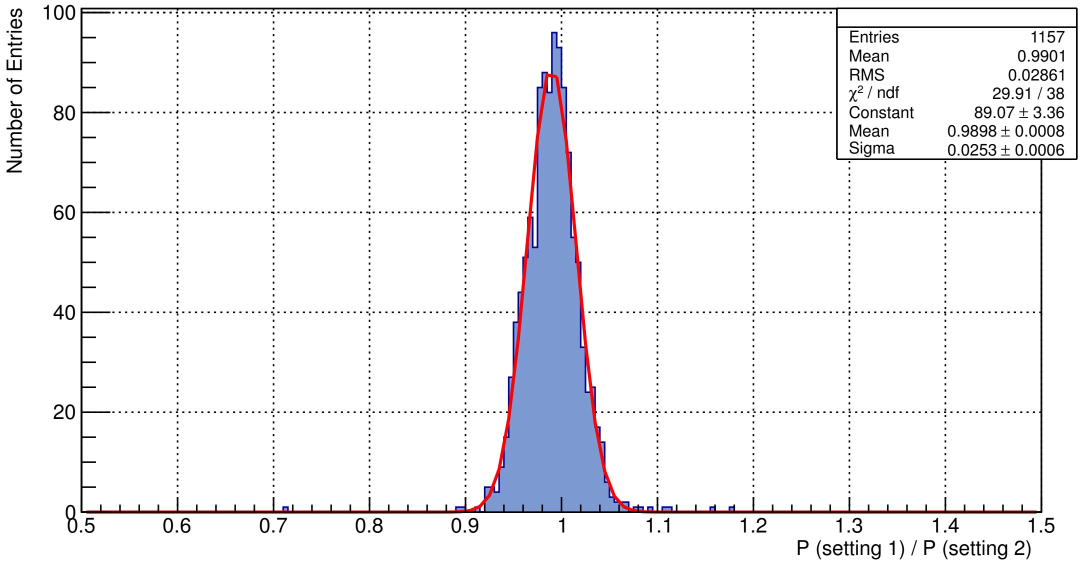

Figure B.2: P (setting 1) / P (setting 2) for protons with 1.5 GeV of momentum traversing the corresponding magnetic field settings. Inset are Gaussian fit parameters.

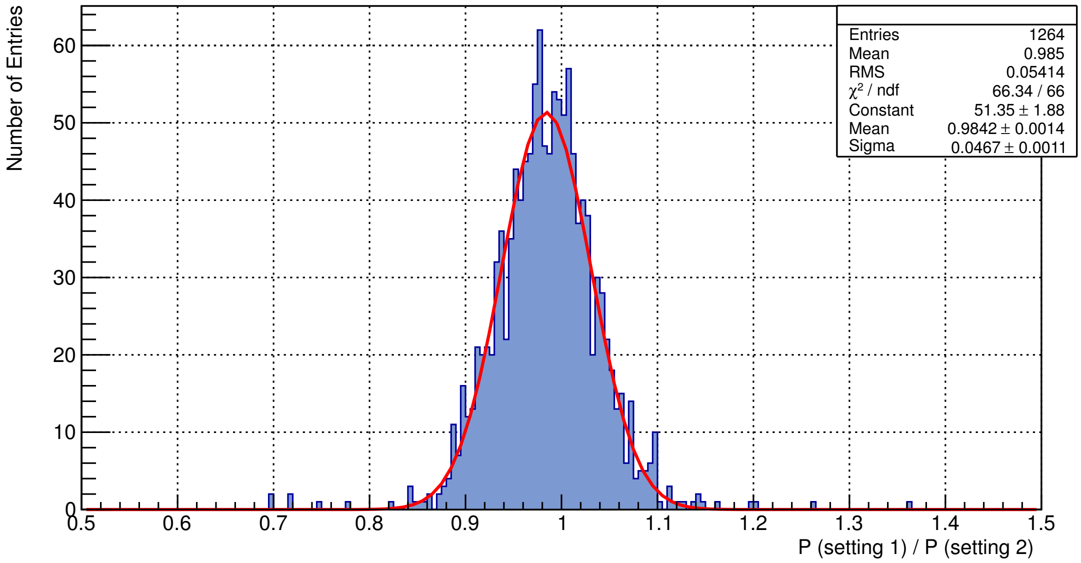

Figure B.3: P (setting 1) / P (setting 2) for protons with 2 GeV of momentum traversing the corresponding magnetic field settings. Inset are Gaussian fit parameters.

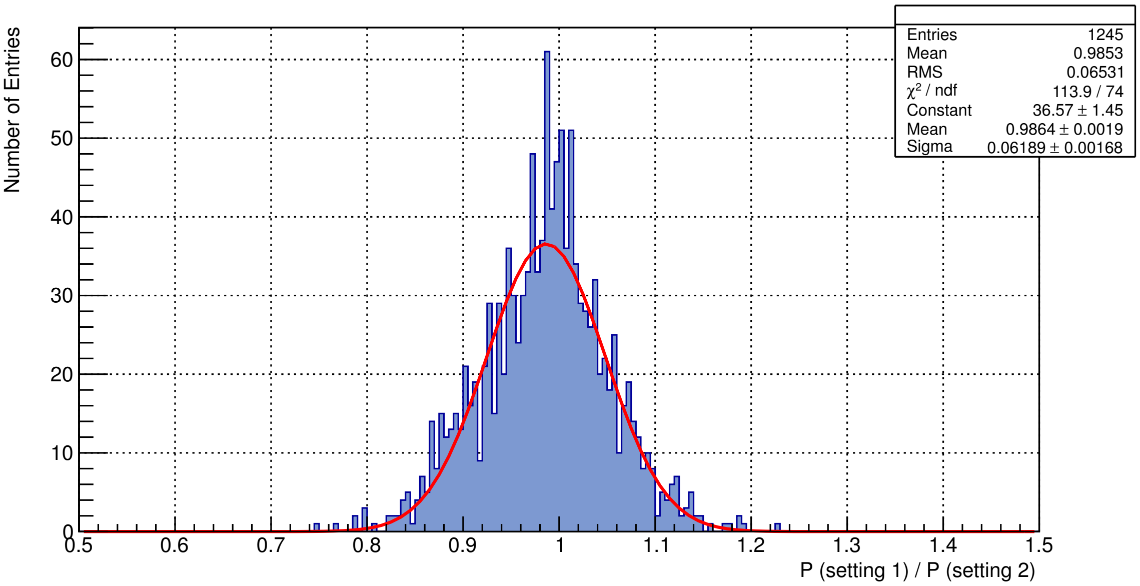

Figure B.4: P (setting 1) / P (setting 2) for protons with 2.5 GeV of momentum traversing the corresponding magnetic field settings. Inset are Gaussian fit parameters.

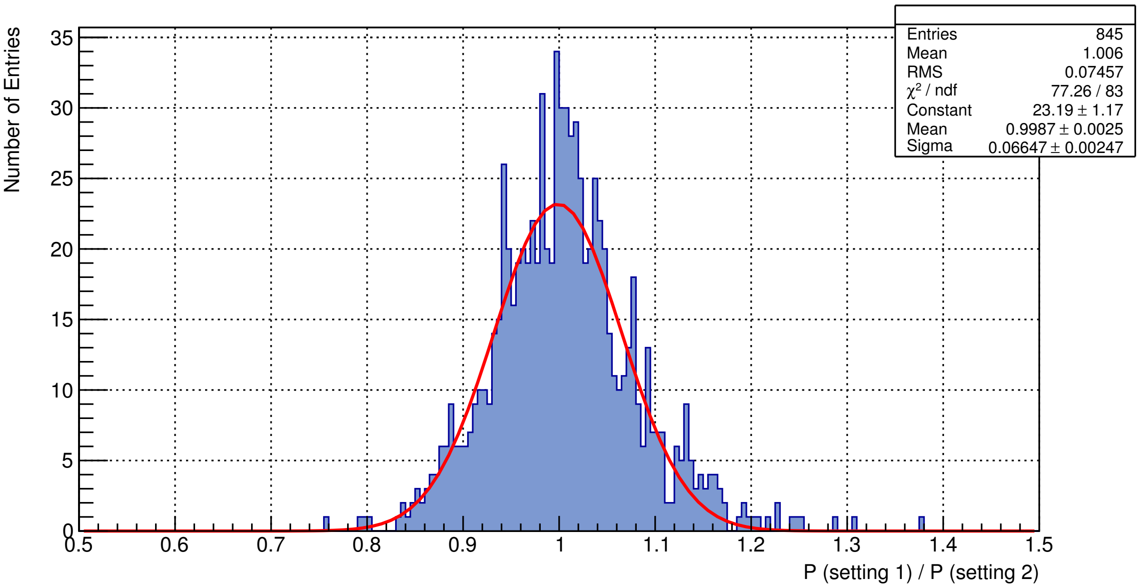

Figure B.5: P (setting 1) / P (setting 2) for protons with 3 GeV of momentum traversing the corresponding magnetic field settings. Inset are Gaussian fit parameters.

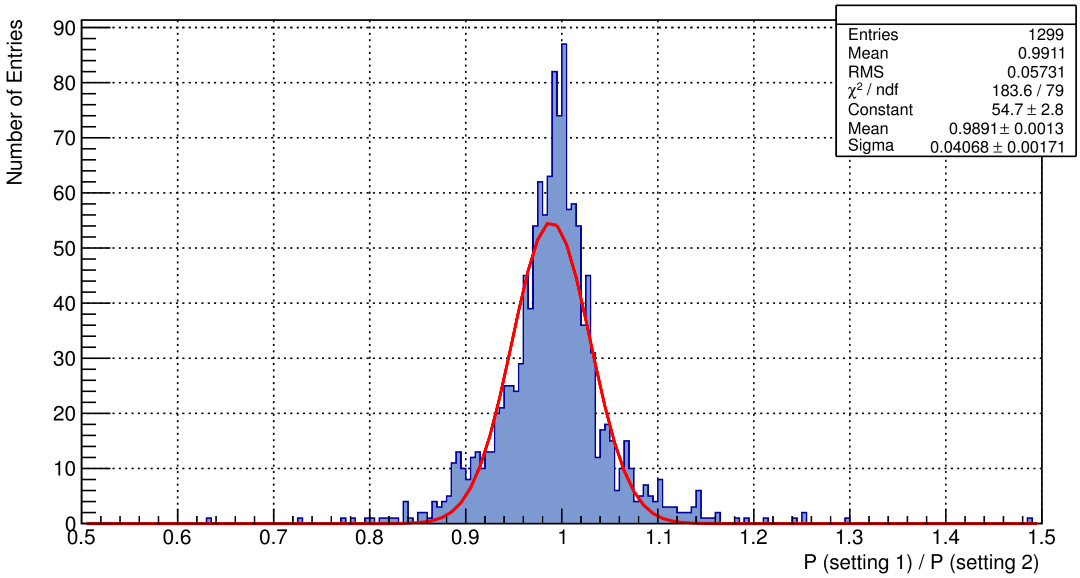

Figure B.6: P (setting 1) / P (setting 2) for protons with a polar angle Θ = 4° which traversing the corresponding magnetic field settings. Inset are Gaussian fit parameters.

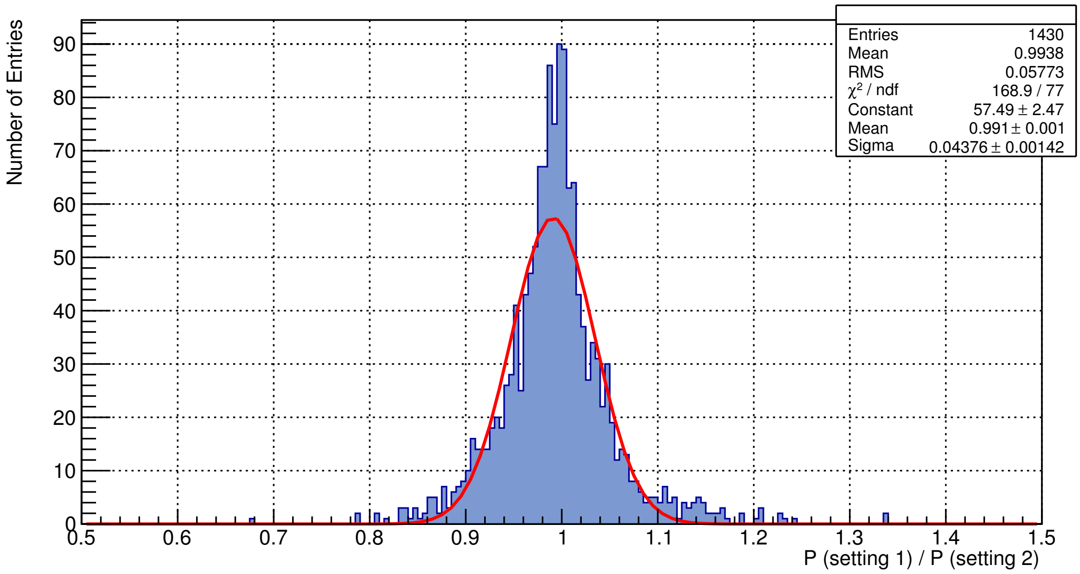

Figure B.7: P (setting 1) / P (setting 2) for protons with a polar angle Θ = 5° which traversing the corresponding magnetic field settings. Inset are Gaussian fit parameters.

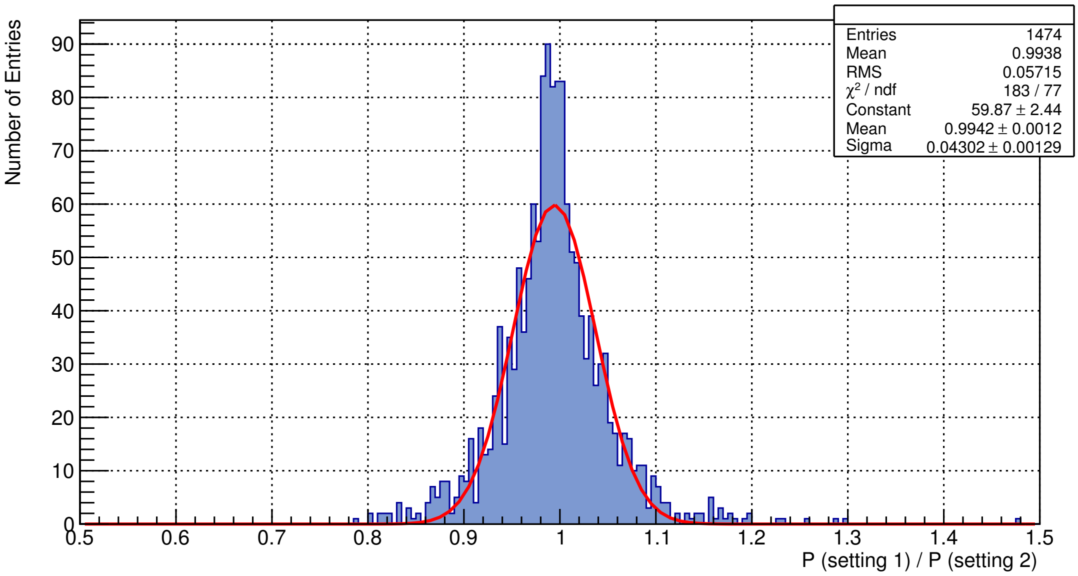

Figure B.8: P (setting 1) / P (setting 2) for protons with a polar angle Θ = 6° which traversing the corresponding magnetic field settings. Inset are Gaussian fit parameters.

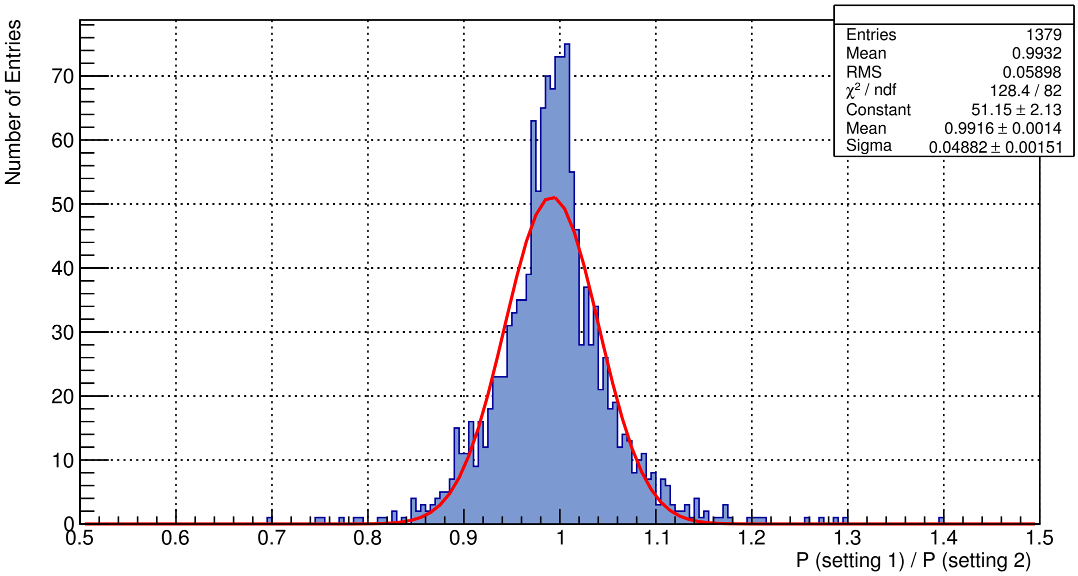

Figure B.9: P (setting 1) / P (setting 2) for protons with a polar angle Θ = 7° which traversing the corresponding magnetic field settings. Inset are Gaussian fit parameters.

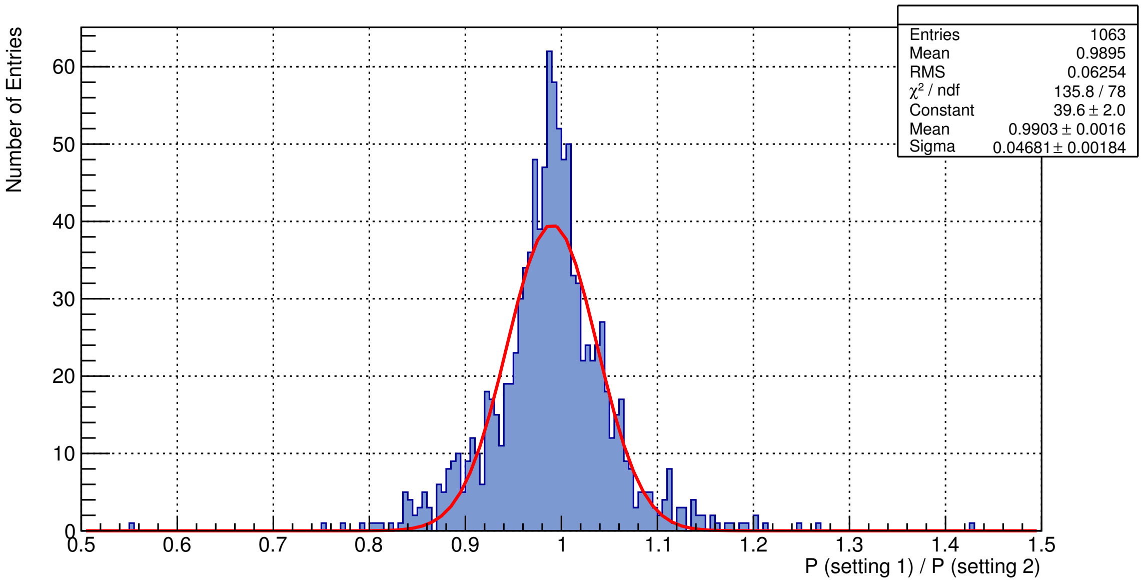

Figure B.10: P (setting 1) / P (setting 2) for protons with a polar angle Θ = 8° which traversing the corresponding magnetic field settings. Inset are Gaussian fit parameters.

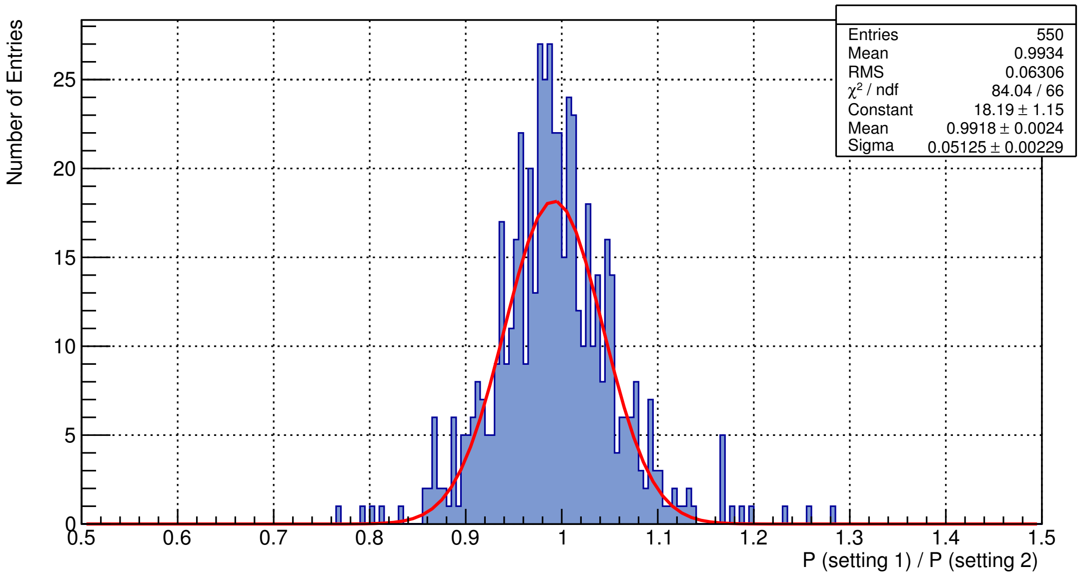

Figure B.11: P (setting 1) / P (setting 2) for protons with a polar angle Θ = 10° which traversing the corresponding magnetic field settings. Inset are Gaussian fit parameters.

Danksagung

Ich bedanke mich recht herzlich bei allen die mich beim Gelingen meines Studium und dieser Diplomarbeit unterstützt haben.
Mein besonderer Dank gilt Herrn Prof. Hartmut Schmieden für die Vergabe dieses interessanten Themas und seiner Unterstützung während meiner Arbeit. Bei Herrn PD Dr. Wolfgang Hillert bedanke ich mich für die Übername des Koreferates. Ich möchte mich bei der ganzen Arbeitsgruppe bedanken für das nette Arbeitsklima und die vielen hilfreichen Diskussionen. Besonders bei Dr. Daniel Elsner und Thomas Zimmermann die mir immer mit Rat und Tat zur Seite standen und bei Dr. Tom C. Jude für seine Hilfe bei der Aufbereitung meiner Messdaten mit Hilfe der Simulation. Ich bedanke mich bei Dr. Valentina Vegna, Dr. Tom C. Jude und Thomas Zimmermann für das Korrekturlesen meiner Diplomarbeit. Zu guter Letzt bedanke ich mich noch bei meiner Familie die mich während meines ganzen Studiums unterstützt hat.

Bibliography

[BÏ2] Böse, Sabine: *PhD Thesis in preparation.* PhD thesis, Rheinische Friedrich-Wilhelms-Universität Bonn, Helmholtz-Institut für Strahlen- und Kernphysik, 2012.

[BGO] *BGO-OD Experiment setup, Dipole magnet.* `http://b1.physik.uni-bonn.de/ExperimentalSetup/Magnet`.

[Cas98] Castoldi, M.: *The temperature monitoring system of a BGO calorimeter.* NIMA 403, page 22, 1998.

[Dri] *BGO-OD Experiment setup, DriftChamber.* `http://b1.physik.uni-bonn.de/ExperimentalSetup/DriftChamber`.

[ELS09] *ELSA facility*, February 2009. `http://www-elsa.physik.uni-bonn.de/Beschleuniger/elsaplan_en.html`.

[Ghi98] Ghio, F.: *The GRAAL high resolution BGO calorimeter and its energy calibration and monitoring system.* NIMA 404, page 71, 1998.

[Gro97] Group3 Technology Ltd: *Group3 Probe Holders*, 1997. `http://www.group3technology.com/dlarea/docs/Group3%20Probe%20Holders%20-%20A4.pdf`.

[Gro05] Group3 Technology Ltd: *MPT-141, mimiature Standard sensitivity Hall probe*, Mai 2005. `http://www.group3technology.com/dlarea/docs/MPT-141%20spec.pdf`.

[Gro07] Group3 Technology Ltd: *DTM-151 DIGITAL TESLAMETER with serial communications, USER'S MANUAL*, Jul 2007. `http://www.group3technology.com/dlarea/docs/DTM-151-S%20Manual%20-S5%2020-Jul-07.pdf`.

[Ham] Hammann, Daniel: *private communication.*

[Han] Hannappel, Dr. Jürgen: *private communication.*

[HS88] Husmann, D. and W. J. Schwille: *ELSA - die neue Bonner Elektronen-Stretcher-Anlage.* Phys. Bl, 44:40–44, 1988.

[Jah] Jahn, Oliver: *private communication.*

[Jud] Jude, Dr. Tom C.: *private communication.*

[Lei08] Leica Geosystems Metrology Products: *Leica Absolute Tracker*, December 2008. `http://www.leica-geosystems.com/downloads123/m1/metrology/AT901/brochures-datasheet/Leica%20Absolute%20Tracker_ASME%20Specifications_en.pdf`.

[MOM] *BGO-OD Experiment setup, MOMO.* `http://b1.physik.uni-bonn.de/ExperimentalSetup/Momo`.

[Nan] Nanotec GmbH & Co.KG: *Optische Impulsgeber*. `en.nanotec.com/downloads/pdf/2012/Encoder-HEDS_HEDL.pdf`.

[O.B05] O.Baztalini: *Measurement of π° photoproduction on the proton from 550 to 1500 MeV at GRAAL*. EPJA 26, page 399, 2005.

[Pho] *BGO-OD Experiment setup, Photon Flux Monitor*. `http://b1.physik.uni-bonn.de/ExperimentalSetup/PhotonFluxMonitor`.

[Phy] Phytron-Elektronik GmbH: *ZSS 19 bis 56, 2-Phasen-Hybrid-Schrittmotor*. `ftp://ftp.phytron.de/datasheets/stepper_motors/zss-d.pdf`.

[San96] Sandri, P. Levi: *Performance of a BGO calorimeter in a tagged photon beam from 260 to 1150 MeV*. NIMA 370, page 396, 1996.

List of Figures

List of Tables